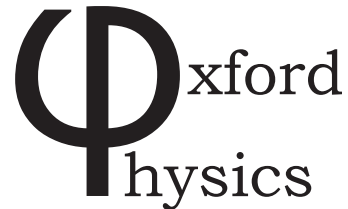


Optical Spectroscopy of Wide Bandgap Semiconductor Nanoscale Structures

Mark J. Holmes

Supervised by Prof. Robert A. Taylor



Thesis submitted for the degree
of Doctor of Philosophy

Department of Physics
University of Oxford

September 2011

Optical Spectroscopy of Wide Bandgap Semiconductor Nanoscale Structures

Mark J. Holmes

Abstract

The optical properties of GaN nanocolumn structures containing InGaN quantum disks are investigated by optical microphotoluminescence spectroscopy using pulsed lasers, and cathodoluminescence. The results are analyzed in the context of current theories regarding an inhomogeneous strain distribution in the disk which has been theorized to generate lateral charge separation in the disks by strain induced band bending, an inhomogeneous polarization field distribution, and Fermi surface pinning. Simulations of the strain distribution for the relevant materials and structures are also performed, and the results analysed. It is concluded from experimental measurements that no extreme lateral separation of carriers occurs in the quantum disks under investigation. Internal field screening by an increased carrier density in the QDisks at higher excitation densities is observed via a blue-shift of the emission and a dynamically changing decay time. Other possible explanations for these effects are discussed and discounted.

Microphotoluminescence studies are also carried out on a single GaN nanocolumn structure that has been removed from its growth substrate and dispersed onto a patterned grid. An analysis of the dynamics of the carriers in the nanocolumn is presented. Suppression of the GaN luminescence from the area of the column in the vicinity of the InGaN QDisk in addition to a delayed emission from the QDisk relative to the GaN is observed. Time resolved spatial maps of the luminescence intensity from the column are also presented, illustrating the evolution of the carrier density in the system.

Additional, albeit early-stage, work on novel structures based on the production of GaN nanocolumns, namely nanotubes and nanopyramids, is also presented.

List of Publications

~Peer Reviewed Journal Publications~

1. **Optical studies on a single GaN nanocolumn containing a single $\text{In}_x\text{Ga}_{1-x}\text{N}$ quantum disk**

Mark J. Holmes, Young S. Park, Xu Wang, Christopher C. S. Chan, Benjamin P. L. Reid, HeeDae Kim, Robert A. Taylor, Jamie H. Warner, Jun Luo. *Appl. Phys. Lett.*, **98**, 251908 (2011). [Chapter 6]

[Selected for the July 2011 issue of the Virtual Journal of Ultrafast Science]

2. **Carrier dynamics of $\text{In}_x\text{Ga}_{1-x}\text{N}$ quantum disks embedded in GaN nanocolumns**

Mark J. Holmes, Young S. Park, Xu Wang, Christopher C. S. Chan, Anas F. Jarjour, Robert A. Taylor, Jamie H. Warner, Jun Luo, H. A. R. El-Ella, and R. A. Oliver. *J. Appl. Phys.*, **109**, 063515 (2011). [Chapter 5]

[Selected for the April 2011 issue of the Virtual Journal of Ultrafast Science]

3. **Optical Studies of GaN Nanocolumns Containing InGaN Quantum Disks and the Effect of Strain Relaxation on the Carrier Distribution**

Mark J. Holmes, YoungSin Park, Xu Wang, Christopher C. S. Chan, Jun Luo, Jamie H. Warner and Robert A. Taylor. *accepted for publication in Phys. Stat. Sol. (c)* (2011)

4. **GaN Nanorods Grown on Si (111) Substrates and Exciton Localization**

Young S. Park, Mark J. Holmes, Y Shon, Im Taek Yoon, Hyunsik Im and Robert A Taylor. *Nanoscale. Res. Lett.*, (**6**) 81 (2011).

5. **Quantum confined Stark effect and corresponding lifetime reduction in a single $\text{In}_x\text{Ga}_{1-x}\text{N}$ quantum disk**

Mark J. Holmes, Young S. Park, Jamie H. Warner and Robert A. Taylor. *Appl. Phys. Lett.*, (**95**) 181910 (2009). [Chapter 5]

[Selected for the December 2009 issue of the Virtual Journal of Ultrafast Science]

6. Mapping cavity modes of ZnO nanobelts

Xiulai Xu, Frederic S. F. Brossard, David A. Williams, Daniel P. Collins, Mark J. Holmes, Robert A. Taylor and Xitian Zhang. *Appl. Phys. Lett.*, **(94)** 231103 (2009).

7. Cavity modes of tapered ZnO nanowires

Xiulai Xu, Frederic S F Brossard, David A Williams, Daniel P Collins, Mark J. Holmes, Robert A Taylor and Xitian Zhang. *New Journal of Physics*, **(12)** 083052 (2010).

8. Cavity enhancement of single quantum dot emission in the blue

Robert A. Taylor, Anas F. Jarjour, Daniel P. Collins, Mark J. Holmes, Rachel A. Oliver, Menno J. Kappers and Colin J. Humphreys. *Nanoscale. Res. Lett.*, **(5)** 608 (2010)

9. Optical properties of bulk-like GaN nanorods grown on Si (111) substrates by rf-plasma assisted molecular beam epitaxy

Young S. Park, T. W. Kang, Hyunsik Im, Mark J. Holmes, and Robert A. Taylor. *Phys. Stat. Sol. (c)*, **(7)** 2211 (2010).

10. Q-factor measurements on planar nitride cavities

Daniel P. Collins, Mark J. Holmes, Robert A. Taylor, Rachel A. Oliver, Menno J. Kappers and Colin J. Humphreys. *Phys. Stat. Sol. (c)*, **(7)** 1866 (2010).

11. Quantum confined Stark effect of InGaN/GaN multi quantum disks grown on top of GaN nanorods

Young S. Park, Mark J. Holmes, Tae W. Kang, and Robert A. Taylor. *nanotechnology*, **21** 115401 (2010). [Chapter 5]

~Conference Presentations~

1. Optical Studies of GaN Nanocolumns Containing InGaN Quantum Disks and the Effect of Strain Relaxation on the Carrier Distribution [poster presentation]

Mark J Holmes, YoungSin Park, Xu Wang, Christopher C. S. Chan, Jun Luo, Jamie H.

Warner and Robert A. Taylor. *ICNS9 10th-15th July 2011, Glasgow, Scotland*. [The presentation resulted in the author receiving the *Young Researcher Award* at ICNS9].

2. Evolution of quantum dot photoluminescence in GaN/InGaN nanorod LEDs

Robert A. Taylor, Christopher C. S. Chan, Philip Shields, Mark J. Holmes, Y. Zhuang, D. Allsopp. *ICNS9 10th-15th July 2011, Glasgow, Scotland*.

3. Optical Studies on In_xGa_{1-x}N Quantum Disks

Mark J. Holmes, Young S. Park, Xu Wang, Christopher C. S. Chan, Anas F. Jarjour, Jamie H. Warner, Jun Luo, Haitham A. R. El-Ella, Rachel A. Oliver and Robert A. Taylor. *SPIE Photonics West 22nd-27th January 2011, The Moscone Center, San Francisco, California, USA*.

4. Quantum Dot-like Emission Lines in Wet-etched Nano-rod Array GaN Based MQW LEDs [poster presentation]

Christopher C. Chan, Mark J. Holmes, Philip A. Shields, Duncan W. E. Allsopp and Robert A. Taylor. *UKNC Annual Conference 2011, 6th-7th January 2011, Manchester University, Manchester, UK*.

5. Carrier Dynamics in In_xGa_{1-x}N Quantum Disks Embedded in GaN Nanocolumns

Mark J. Holmes, Young S. Park, Xu Wang, Christopher C. S. Chan, Anas F. Jarjour, Robert A. Taylor, Jamie H. Warner, Jun Luo, H. A. R. El-Ella and Rachel A. Oliver. *UKNC Annual Conference 2011, 6th-7th January 2011, Manchester University, Manchester, UK*.

6. Internal Field Shielding and the Quantum confined stark effect in a single In_xGa_{1-x}N quantum disk [poster presentation]

Mark J. Holmes, Young S. Park, Jamie H. Warner, Jun Luo, Xu Wang, Anas F. Jarjour and Robert A. Taylor. *ICPS-30, 25th-30th July 2010, COEX exhibition centre, Seoul, Republic of Korea*.

7. Quantum confined stark effect in a single In_xGa_{1-x}N quantum disk

Mark J. Holmes, Young S. Park, Jamie H. Warner and Robert A. Taylor. *UKNC Annual Conference 2010, 12th-13th January 2010, Tyndall Institute, Cork, Rep. of Ireland.*

8. Optical properties of bulk-like GaN nanorods grown on Si (111) substrates by rf-plasma assisted molecular beam epitaxy [poster presentation]

Young S. Park, Tae W. Kang, Hyunsik Im, C. M. Park, Myung-Soo Han, Mark J. Holmes, and Robert A. Taylor. *INCS8 October 18th - 23rd 2009, Jeju-do, Republic of Korea.*

9. Micro-reflectivity studies of planar nitride cavities [poster presentation]

Daniel. P. Collins, Anas. F. Jarjour, Mark. J. Holmes, Robert. A. Taylor, Rachel. A. Oliver, Menno. J. Kappers, Colin. J. Humphreys. *INCS8 October 18th - 23rd 2009, Jeju-do, Republic of Korea.*

10. Micro-reflectance studies of AlGaN/GaN DBRs

Mark. J. Holmes, Daniel. P. Collins, Anas. F. Jarjour, Rachel. A. Oliver, Robert. A. Taylor, Menno J. Kappers and Colin. J. Humphreys. *UKNC Annual Conference 2009, 7th-8th January 2009, University of Oxford, UK.*

1	Introduction and Thesis Overview	11
2	The Properties of III-Nitride Semiconductors	14
2.1	Crystal Structure and the Emergent Spontaneous Polarization	14
2.2	Band Structure	16
2.3	Excitons	16
2.4	$\text{In}_x\text{Ga}_{1-x}\text{N}$	17
2.5	Piezoelectric Polarization	20
2.5.1	Stress and Strain	20
2.5.2	Piezoelectricity	21
2.6	The Quantum Confined Stark Effect	23
2.7	Defects and Dislocations	26
2.8	GaN Nanocolumns and their Growth Process	27
3	Modelling the Strain Distribution in an InGaN Quantum Disk/GaN Nanocol- umn System, and Considerations on the Resulting Carrier Distribution	30
3.1	Strain Simulation Process	30
3.2	The Strain Distribution in an InGaN Quantum Disk	31
3.3	On the Resulting Carrier Distribution	35
3.3.1	Piezoelectric Effect (QCSE)	35
3.3.2	Deformation Potentials	37
3.3.3	Fermi-surface Pinning	39
3.4	Combination of effects	41
3.5	Additional work on multiple QDisk stacks	44
4	Experimental Techniques	47
4.1	Introduction	47
4.2	Excitation Sources	47
4.2.1	Ti:Al ₂ O ₃ Laser	47
4.2.2	2 nd and 3 rd Harmonic Generation: Ultrafast Pulses at 400 and 266 nm	48
4.3	Time Integrated μ -Photoluminescence Studies	49

4.4	Time Resolved μ -Photoluminescence Studies	51
4.5	Electron Beam Lithography	53
4.5.1	JEOL JBX-5500ZC electron beam lithography system	55
4.6	Cathodoluminescence	57
5	The Carrier Dynamics of $\text{In}_x\text{Ga}_{1-x}\text{N}$ Quantum Disks Embedded in GaN Nanocolumns	58
5.1	Initial investigation into GaN nanocolumns	58
5.2	Determination of the nanocolumn/QDisk luminescence spectrum	59
5.3	μ -PL experiments on as-grown columns	62
5.3.1	Temperature dependent time-resolved μ -PL studies and the subsequent implications for the carrier distribution in the QDisk	62
5.3.2	Low temperature μ -photoluminescence studies: The quantum confined Stark effect	64
5.3.3	Further evidence for the QCSE in $\text{In}_x\text{Ga}_{1-x}\text{N}$ QDisks	70
5.4	Defect emission	70
5.5	Chapter Summary	72
6	Optical Studies on a Single GaN Nanocolumn Containing a Single $\text{In}_x\text{Ga}_{1-x}\text{N}$ Quantum Disk	75
6.1	Isolating and locating a single nanocolumn	75
6.2	(The lack of) plasmon effects	77
6.3	Initial Optical studies on the single column	77
6.4	Chapter Summary	82
7	Self Assembled III-Nitride Nanotubes and Nanopyramids	84
7.1	The Optical Properties of Self-Assembled Crystalline GaN Nanotubes	84
7.1.1	Experimental studies on GaN nanotubes	86
7.1.2	The red-shifted emission	88

7.2	Self-assembled GaN nano-pyramids grown on InGaN/GaN nanocolumns	90
7.2.1	Summary	94
8	Summary, Outlook, and Concluding Remarks	95
A	Non Linear Optical Effects	98
A.1	The Kerr Effect and Kerr Lens Modelocking	98
B	Estimating the $\text{In}_x\text{Ga}_{1-x}\text{N}$ QDisk Indium Content	100
C	Cleanroom Processing	105
C.1	E-beam lithography	105
C.2	Process: Single nanocolumn sample	106
C.3	Process: Mask for single QD excitation	107
D	nextnano³ input file	108
E	Superconducting Nanowire Single Photon Detector	113
E.1	Current State of the Art	113
E.2	Theory of Superconducting Nanowire Single Photon Detectors	114
E.3	Niobium Nitride Nanowire	115
E.4	Construction and Operation of the SNSPD System	117
E.5	Characterisation	120
E.6	Experimental use	124
E.7	Summary and outlook	124
	References	125

1

Introduction and Thesis Overview

Since bursting onto the scene of the optoelectronics industry in the late 1990's, III-Nitride semiconductors have found their way into many household appliances. Blue LED's, white LEDs, Blu-ray laser applications are just some examples. This rapid ascension to market acceptance is due to the unique properties of the material system. Gallium nitride has a direct, wide, bandgap of 3.39 eV at 300 K [1] allowing efficient, low wavelength light emission. By utilising GaN together with it's related compounds (typically AlN and InN with respective band gaps of 6.2 eV and 0.8 eV) it is theoretically possible to create systems which luminesce from the UV to the near infra-red. III-Nitrides are also seen as a eco-friendly option, due to their non-toxicity (conventional semiconductor systems often contain arsenic and phosphorous). In addition to these properties, GaN displays inertness to many corrosive chemicals, and is resilient at high temperatures and pressures [2]: It is quite plausible, then, that III-Nitride based devices will find employment in demanding environments. The wide bandgap and high breakdown voltages exhibited by GaN also make the material an excellent choice for high power and high frequency electronics applications [3, 4].

These properties ensure that III-Nitrides are of great interest to the semiconductor optoelectronics industry. It is perhaps surprising then, that III-Nitrides didn't come into fruition in the semiconductor industry until the 1990's [5], due to extensive research by Nichia corporation. Therefore, as a relatively new semiconductor system, the III-Nitrides have yet to reach the maturity enjoyed by systems such as the III-Arsenides; the workhorse of the IR telecommunications and optoelectronics industry. This is due to both a lack of full understanding of the system's

electronic and opto-electronic properties, and a relatively poor crystal quality of produced samples. Great achievements have, however, been made within the last 20 years. In particular the realisation of optoelectronic devices such as LEDs [6, 7, 8] and laser diodes [5]. Single photon sources have been created from InGaN quantum dots [9], and further recent studies have centred on cavities operating in the strong light-matter coupling regime [10], and polariton lasing [11, 12].

In this thesis the optical properties of GaN/InGaN nanocolumnar heterostructures are reported. These structures may become important in the future when used in light emission devices to increase efficiency. GaN nanocolumns themselves, are seen as an attractive system for a wide range of semiconductor devices. Indeed, LED's [13, 14], photonic crystals [15], biosensors [16] and UV sensors [17] are just some of the device/device components that have been realised thus far. Nanocolumnar structures have also been used as seeds for quantum dot (full 3-dimensional confinement) growth [18], and lasing has also been observed in regularly arranged GaN columns [15]. Recently, Sekiguchi *et al.* have produced a series of light emitting GaN/InGaN columns that emit across the whole of the visible spectrum [19]. Further, more recent, studies have involved interfacing various species of nanocolumn (including GaN) with neurons [20, 21]. The definition of a nanocolumn is fairly broad in the sense that the range of diameter can range from a few 10's to a few 100's of nanometers, but in each case the properties of the structure are affected by the large surface to volume ratio.

In Chapter 2 a brief overview of the physical properties of III-Nitrides and a discussion their defining properties is presented (namely the wide direct bandgap and the internal electric fields). This is followed in Chapter 3 by an explanation and discussion of some strain simulations that have been carried out on the nanocolumnar structures that will provide the main focus for this work. We will see that the strain distribution in their heterostructures may have profound effects on the carrier and recombination dynamics.

In Chapter 4 a detailed explanation of the experimental techniques that are required to investigate the effects of the strain on the carrier recombination is provided. This will include

both time integrated and time resolved microphotoluminescence techniques, and non linear optical systems to generate frequency tripled light from a pulsed Ti:Al₂O₃ laser. Electron beam lithography and various cleanroom based device fabrication techniques have also been employed in the fabrication of grids utilised for the location of single structures, these will also be described.

The main experimental data based section of the thesis are Chapters 5 and 6. The experimental studies on the GaN nanocolumns and InGaN QDisks are presented along with a discussion in Chapter 5. This will lead to some interesting insights on the carrier distribution in the structures. A related study on a single nanostructure will be described in detail in Chapter 6.

In Chapter 7 an introduction to further experiments that have been performed on novel nitride nanostructures (namely *nanopyramids* and *nanotubes*) is given. In both cases the structures materialize by a self formation process, which is novel as the only current known method of fabrication is by a several step etching process, or using selective growth patterned substrates.

A general conclusion, and outlook for future experiments will be given in Chapter 8, which will then be followed by the appendices. These include several discussions on related material that doesn't quite fit in the flow of the main text. The estimation of the nanostructure indium content, for example, or the description of an input file for the strain simulations. In one appendix we describe the manufacture, setup, characterisation and experimental use of a superconducting nanowire single photon detector for use in the near infra-red.

At the very end of the thesis, two poster presentations that were given by the author at international conferences (ICPS 2010 in Seoul, Korea, and ICNS 2011 in Glasgow, Scotland) are presented in figures E.10 and E.11, respectively.

2

The Properties of III-Nitride Semiconductors

III-Nitride semiconductor-based structures are enjoying success in optoelectronic device applications, due largely to the wide direct band gap exhibited by GaN, enabling efficient high energy emission [5, 22]. The ability to incorporate either indium or aluminium, during growth, to form ternary/quaternary compounds enables the construction of crystals with a wide range of band gap energies and hence emission wavelengths [23]. When in the wurtzite crystal structure (space group $P6_3mc$) these structures will be at the mercy of an inbuilt electric field that has components due to both a spontaneous polarisation and a strain induced piezoelectric field ($P6_3mc$ is a non-centrosymmetric group). In nanostructures the effect of these fields (which have a combined magnitude of order MVcm^{-1} [24, 25, 26, 27]) is to redshift the energy spectrum, and increase the emission lifetime by the quantum confined Stark effect (QCSE). These effects, along with the basic structural parameters of III-Nitrides, are presented and discussed in this chapter.

2.1 Crystal Structure and the Emergent Spontaneous Polarization

The III-Nitride semiconductor is found naturally in one of two crystal structures; The zinc-blende structure with cubic symmetry (space group $F\bar{4}3m$) or the wurtzite structure with hexagonal symmetry (space group $P6_3mc$). The wurtzite structure is the most stable of the two (The energy difference between the two states has been calculated as 10 meV per atom [28]), and most III-Nitride systems are found to be crystallized in this structure. All samples investigated in this thesis have the wurtzite crystal structure, of which a representation of the primitive cell can be

found in figure 2.1. The image was created using the freely available software *balls and sticks* [29]. In this figure the crystal axes were set to $a = b = 3.174 \text{ \AA}$ and $c = 5.169 \text{ \AA}$ [30]. The radii of the atoms are set to the covalent radii of the respective species (Ga= 1.26 \AA , N= 0.75 \AA [31]).

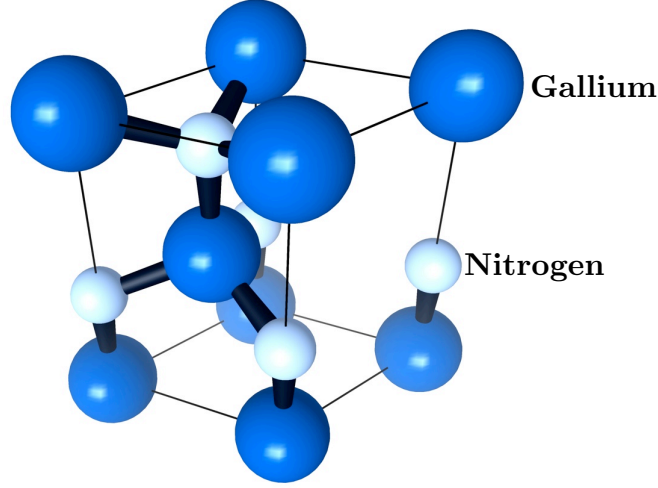


Figure 2.1: *The unit cell of the wurtzite structure GaN crystal. The image was created using the freely available software balls and sticks [29].*

The lattice parameters of the materials relevant to this study, namely wurtzite structure GaN and InN can be found in table 2.1. The lattice parameters of InGaN will be discussed separately in section 2.4.

lattice parameter:	a	c
GaN	3.174 \AA	5.169 \AA
InN	3.538 \AA	5.707 \AA

Table 2.1: *Calculated lattice parameters for wurtzite GaN and InN (Taken from reference [30]).*

A consequence of the wurtzite crystal symmetry is that the $[0001]$ and $[000\bar{1}]$ directions are not equivalent, and one may thus define the polarity of a given grown crystal. Furthermore, nitrogen has a larger affinity for electrons (electronegativity) such that the electron clouds in the metal-nitrogen bonds are shifted towards the nitrogen atoms. This affect, along with the atomic positioning in the primitive unit cell leads to a spontaneous, and microscopic polarization in the

the primitive unit cell, which results in a macroscopic polarization in the whole crystal. This effect is compounded by the fact that the real III-Nitride crystal structure is not ideal ($\frac{c}{a} \neq \sqrt{\frac{8}{3}}$) and thus the bond length is compressed in the [0001] direction, giving rise to further separation of the electron cloud and ion core charge barycentres.

As space group $P6_3mc$ is non-centrosymmetric, III-Nitride systems exhibit a piezoelectric nature (the emergence of an electric field in response to strain) which will be outlined in section 2.5.* This nature will have profound effects on the recombination dynamics of charge carriers confined in nano-scale heterostructures, as we shall see in chapter 5.

2.2 Band Structure

The optical properties of GaN are characterised by the wide direct band gap (~ 3.39 eV) at the Γ point of the Brillouin zone ($k = 0$). The physical origin of a semiconductor band gap is due to the overlapping of the atomic orbitals of the constituent atoms as they hybridize to form molecular orbitals. The lower energy bonding molecular orbitals which are formed primarily by p atomic orbitals form the, filled, valence band. Likewise, the conduction band is formed by the antibonding molecular orbitals, and takes s -like character. Due to an interaction with the crystal field, the degeneracy between the in plane (p_x and p_y) and out of plane (p_z) states is lifted. The p_x and p_y degeneracy is further lifted by spin orbit coupling, leaving 3 valence bands. In the case of GaN, these bands are labelled A, B and C [33]. A simplified diagram of the GaN bandstructure at the Γ point is shown in figure 2.2. Furthermore, the valence bands near the Γ point are highly anharmonic [34], meaning that the effective mass approximation (which relies on a quadratic band dispersion) needs to be used with care.

2.3 Excitons

The excitation of an electron across the band gap by the absorption of a photon leaves a hole which can become bound via the Coulomb interaction with the electron to form a state called

*A simple argument as to why only those crystals with no inversion symmetry exhibit piezoelectric effects is given in reference [32].

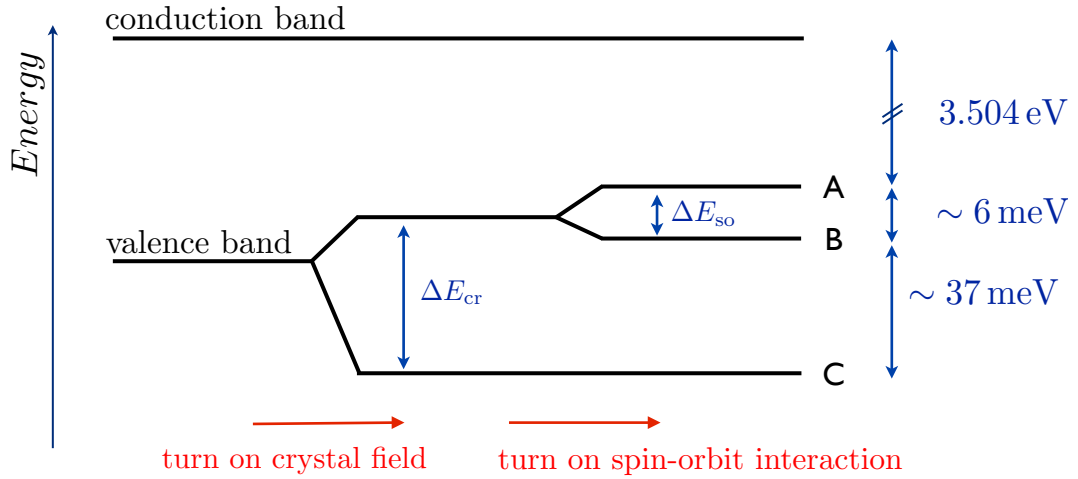


Figure 2.2: A simplified bandstructure diagram for GaN. The values of the gaps are taken from reference [34].

an exciton. This bound state can be modelled as a hydrogen atom, with binding energy given by a modified Rydberg constant ($R = \mu^* e^4 / 2h^2 \epsilon^2$) [35], where μ is the reduced effective mass of the electron and hole ($1/\mu^* = 1/m_e^* + 1/m_h^*$). The binding energy of the A-exciton in GaN has been measured by many groups using different techniques [36] and is typically found to be between 20 and 30 meV [37, 38, 39]. This value, however, is found to change with strain, so the measured values will depend strongly on the sample substrate and layer thicknesses [36]. The recombination energy then, is the band gap less the exciton binding energy. The excitons can be free to move around in the material, though may also become bound in potential fluctuations caused by impurities in the crystal. In epitaxially grown GaN, the most common impurities are donors (typically Si),[†] so many excitons can typically be found bound to donor sites [36].

2.4 $\text{In}_x\text{Ga}_{1-x}\text{N}$

The ternary compound $\text{In}_x\text{Ga}_{1-x}\text{N}$ is often used to create heterostructures with GaN. The low, direct, bandgap of InN in theory facilitates the fabrication of $\text{In}_x\text{Ga}_{1-x}\text{N}$ structures that can emit light at wavelengths across the whole of the visible spectrum [40, 19]. depending on their indium mole fraction, x . In this section the basic parameters of InGaN are discussed, and an

[†]Indeed, most intrinsically grown nitride materials are to some extent n -type.

introduction to the concept of strain in epitaxially grown materials is given.

Bandgap

The band gap of $\text{In}_x\text{Ga}_{1-x}\text{N}$ lies between the bandgaps of GaN and InN, however there is not a linear relationship between the indium mole fraction, x , and the band gap; a bowing parameter b_{bow} is necessary to describe the relation via

$$E_g^{\text{In}_x\text{Ga}_{1-x}\text{N}} = (1-x)E_g^{\text{GaN}} + xE_g^{\text{InN}} - b_{\text{bow}}x(1-x). \quad (2.1)$$

The bandgap of InN itself, was originally measured to be ~ 1.89 eV for thin films prepared by RF-sputtering [41], though it is generally believed that this value is too high (due to poor quality material growth) and has more recently been re-evaluated to be in the range of 0.7 to 0.8 eV [42, 43, 44]. It should be noted that this lower value is still not completely accepted by the international research community; Shubina *et al* have provided some evidence that the 0.7 eV band gap may actually be due to surface states which are pinned at about 0.7 eV above the conduction band edge, and that the real band gap may be as high as 1.4 eV [45]. It has also been commented [46] that a band gap of 0.7 eV is lower than should be expected for InN, and that further study is required.

Values of the bowing parameter in the literature vary largely; parameters of 1.43 eV [43], 2.8 eV [47], 3.65 eV [48], and 4.1 eV [49] have each been reported, and can be compared to a theoretical value of 1.7 eV [50]. It should also be noted that some calculations suggest that the bowing parameter is itself composition dependent [51]. This wide range of reported parameters leads to an uncertainty, making reliable theoretical calculations for low indium content $\text{In}_x\text{Ga}_{1-x}\text{N}$ difficult to perform.

Lattice parameters

The lattice parameters for InN are given in table 2.1. As indium is a physically larger atom than gallium (1s2 2s2 2p6 3s2 3p6 4s2 3d10 4p6 5s2 4d10 5p1 as opposed to 1s2 2s2 2p6 3s2 3p6 4s2

3d10 4p1), the lattice parameters of InN are larger than those of GaN. The lattice parameters of the ternary compound $\text{In}_x\text{Ga}_{1-x}\text{N}$ are found by Vegard's Law [52] i.e. linear interpolation between those of GaN and InN;

$$a_{\text{In}_x\text{Ga}_{1-x}\text{N}} = (1 - x)a_{\text{GaN}} + xa_{\text{InN}}. \quad (2.2)$$

When under homogeneous strain, for example in the condition of pseudomorphic growth[‡] on GaN, the $\text{In}_x\text{Ga}_{1-x}\text{N}$ layer will take on the in-plane lattice parameter of the underlying material, and exhibit a changed band gap due to the effect of the strain and the deformation potentials (see section 3.3.2).

Band tailing and localisation

It has been postulated and experimentally verified that epitaxially grown $\text{In}_x\text{Ga}_{1-x}\text{N}$ layers may contain regions of varying indium content, and may indeed segregate into small indium rich inclusions within a matrix of lower indium content material [54]. These regions of higher indium content can act as potential traps, and create localised states for charge carriers. These localised states create a tailing in the density of states, which can be observed by an S-shape in the emission wavelength as the sample temperature is increased towards room temperature [55, 48, 56]. The S-curve is caused by a shift in the carrier distribution to higher energy states (generated by the inhomogeneous distribution in indium content) before the onset of the shift to lower energy caused by the well known reduction of the band gap energy due to thermal expansion of the crystal with increasing temperature [57, 58, 59].

It has been theoretically shown that the degree of localisation becomes greater for larger x , and that low indium content ($x < 0.2$) quantum wells should have very limited broadening (< 5 meV) due to indium content fluctuations [60]. Indeed there is experimental evidence to support this [61].

[‡]defined as the condition that up until a critical growth thickness, a grown material takes on the lattice parameters of the material onto which it is grown: for $\text{In}_x\text{Ga}_{1-x}\text{N}$ this critical thickness has been measured (for $0.05 \leq x \leq 0.2$) to be ~ 400 nm [53], well above that of the structures under investigation in this study.

2.5 Piezoelectric Polarization

The piezoelectric effect can be found in many materials, and is described as a generation of polarization in response to an external stress. This is particularly important for III-Nitride materials which are often under strain due to a lack of suitable growth substrate. The effect is best described using tensor notation, as will be outlined here. For a more in depth description, the reader is directed to Nye (1985) [32]. The strain introduced into an pseudomorphically grown layer of $\text{In}_x\text{Ga}_{1-x}\text{N}$ on GaN is one such cause of the piezoelectric effect in III-Nitrides. The effect is described below.

2.5.1 Stress and Strain

Before contemplating the piezoelectric effect, a method to describe stress and strain within a solid is necessary. Stress, or a force per unit area applied to a crystal is usually represented by a rank 2 tensor of elements σ_{jk} , with $\sigma_{jk} = \sigma_{kj}$ in the absence of body torques [32]. The stress tensor itself relates the force across an area element within the volume of the solid body to the vector perpendicular to that element, and is related to the strain (effectively the deformation of the material) which is also a rank 2 tensor of elements ϵ_{jk} , by Hooke's law:

$$\sigma_{ij} = \zeta_{ijkl}\epsilon_{kl}, \quad (2.3)$$

where ζ_{ijkl} are the elements of the rank 4 compliance tensor (elastic modulus). Although both σ and ϵ contain $3^2 = 9$ elements, only 6 of these are independent in the absence of torque, so that it is possible to re-index the tensors:

$$\begin{pmatrix} \sigma_{11} & \sigma_{12} & \sigma_{13} \\ \sigma_{21} & \sigma_{22} & \sigma_{23} \\ \sigma_{31} & \sigma_{32} & \sigma_{33} \end{pmatrix} \longrightarrow \begin{pmatrix} \sigma_1 & \sigma_6 & \sigma_5 \\ \sigma_6 & \sigma_2 & \sigma_4 \\ \sigma_5 & \sigma_4 & \sigma_3 \end{pmatrix}, \quad (2.4)$$

and also the compliance tensor such that

$$\sigma_i = \zeta_{ij}\epsilon_j \quad (2.5)$$

where the stress and strain tensors have be written in their re-indexed form as pseudo-vectors. This Voigt notation is useful for the following analysis of the piezoelectric effect which involves the rank 3 piezoelectric tensor.

The strain is effectively the degree of extension or compression of the material and can be also written as, in the special case of biaxial strain,

$$\epsilon_1 = \epsilon_2 = \frac{a_{\text{strained}} - a_0}{a_0} \quad (2.6)$$

$$\epsilon_3 = \frac{c_{\text{strained}} - c_0}{c_0} \quad (2.7)$$

where a_{strained} and c_{strained} are the lattice parameters for the strained layer, and likewise a_0 and c_0 are the parameters for an unstrained material.

2.5.2 Piezoelectricity

The polarisation P_i induced in a medium by stress/strain is related to the stress tensor σ_{jk} by the relation

$$P_i = d_{ijk}\sigma_{jk}, \quad (2.8)$$

where d_{ijk} are the elements of the (rank 3) piezoelectric tensor [32]. In general the piezoelectric tensor has $3^3 = 27$ components, though, due to the same symmetry argument as above, it can be seen that $d_{ijk} = d_{ikj}$. Therefore, the number of independent elements is reduced to 18, and in similar fashion to the stress and strain tensors, d_{ijk} can be re-indexed as:

$$\begin{pmatrix} d_{i11} & d_{i12} & d_{i13} \\ d_{i21} & d_{i22} & d_{i23} \\ d_{i31} & d_{i32} & d_{i33} \end{pmatrix} \longrightarrow \begin{pmatrix} d_{i1} & \frac{1}{2}d_{i6} & \frac{1}{2}d_{i5} \\ \frac{1}{2}d_{i6} & d_{i2} & \frac{1}{2}d_{i4} \\ \frac{1}{2}d_{i5} & \frac{1}{2}d_{i4} & d_{i3} \end{pmatrix}, \quad (2.9)$$

and equation 2.8 rewritten as [32]:

$$P_i = d_{ij}\sigma_j, (i = 1, 2, 3; j = 1, 2...6). \quad (2.10)$$

In full matrix notation, equation 2.10 is expanded as

$$\begin{pmatrix} P_1 \\ P_2 \\ P_3 \end{pmatrix} = \begin{pmatrix} d_{11} & d_{12} & d_{13} & d_{14} & d_{15} & d_{16} \\ d_{21} & d_{22} & d_{23} & d_{24} & d_{25} & d_{26} \\ d_{31} & d_{32} & d_{33} & d_{34} & d_{35} & d_{36} \end{pmatrix} \begin{pmatrix} \sigma_1 \\ \sigma_2 \\ \sigma_3 \\ \sigma_4 \\ \sigma_5 \\ \sigma_6 \end{pmatrix} \quad (2.11)$$

The complexity of the piezoelectric matrix δ_{ij} can be even further reduced by careful analysis of the crystal symmetry. For the wurtzite class it is found that there are only 3 non-vanishing components of the piezoelectric tensor[§]; δ_{33} , δ_{13} and δ_{15} [62].

$$\begin{pmatrix} P_1 \\ P_2 \\ P_3 \end{pmatrix} = \begin{pmatrix} 0 & 0 & 0 & 0 & d_{15} & 0 \\ 0 & 0 & 0 & d_{15} & 0 & 0 \\ d_{31} & d_{31} & d_{33} & 0 & 0 & 0 \end{pmatrix} \begin{pmatrix} \sigma_1 \\ \sigma_2 \\ \sigma_3 \\ \sigma_4 \\ \sigma_5 \\ \sigma_6 \end{pmatrix} \quad (2.12)$$

Similar analysis of the crystal symmetry leads to simplification of the rank 2 compliance pseudo-tensor:

$$\begin{pmatrix} \sigma_1 \\ \sigma_2 \\ \sigma_3 \\ \sigma_4 \\ \sigma_5 \\ \sigma_6 \end{pmatrix} = \begin{pmatrix} \zeta_{11} & \zeta_{12} & \zeta_{13} & 0 & 0 & 0 \\ \zeta_{12} & \zeta_{11} & \zeta_{13} & 0 & 0 & 0 \\ \zeta_{13} & \zeta_{13} & \zeta_{33} & 0 & 0 & 0 \\ 0 & 0 & 0 & \zeta_{44} & 0 & 0 \\ 0 & 0 & 0 & 0 & \zeta_{44} & 0 \\ 0 & 0 & 0 & 0 & 0 & \zeta_{66} \end{pmatrix} \begin{pmatrix} \epsilon_1 \\ \epsilon_2 \\ \epsilon_3 \\ \epsilon_4 \\ \epsilon_5 \\ \epsilon_6 \end{pmatrix}, \quad \zeta_{66} = \frac{1}{2}(\zeta_{11} - \zeta_{12}), \quad (2.13)$$

such that the strain induced piezoelectric polarization arising due to a given strain distribution $\epsilon(xyz)$ be calculated from equations 2.12 and 2.13 for known piezoelectric constants:

$$\begin{pmatrix} P_1 \\ P_2 \\ P_3 \end{pmatrix} = \begin{pmatrix} 0 & 0 & 0 & 0 & e_{15} & 0 \\ 0 & 0 & 0 & e_{15} & 0 & 0 \\ e_{31} & e_{31} & e_{33} & 0 & 0 & 0 \end{pmatrix} \begin{pmatrix} \epsilon_1 \\ \epsilon_2 \\ \epsilon_3 \\ \epsilon_4 \\ \epsilon_5 \\ \epsilon_6 \end{pmatrix}, \quad (2.14)$$

where e_{ij} is the Voigt notation representation of the matrix relating polarization to strain.

[§]Indeed, wurtzite is the structure with the highest order of symmetry that exhibits a piezoelectric nature [62, 63]

In the growth direction then, the degree of polarization can be written as

$$P_z = e_{31}(\epsilon_{xx} + \epsilon_{yy}) + e_{33}\epsilon_{zz}, \quad (2.15)$$

where now the index of the strain tensor has been rewritten in terms of cartesian co-ordinates.

From this point on in the current work, this convention will be obeyed.

It is found, in both simulation [62] and experiment [64], that the piezoelectric constants for III-nitrides are relatively high. A comparison of piezoelectric constants between several materials (theoretical values) can be found in table 2.2. The values have been taken from Bernardini *et al.* [62].

	e_{33}	e_{31}		e_{33}	e_{31}		e_{33}	e_{31}		e_{33}	e_{31}
AlN	1.46	-0.60	CdTe	0.03	-0.01	AlAs	-0.01	0.01	ZnS	0.10	-0.05
GaN	0.73	-0.49	GaAs	-0.12	0.06	ZnSe	0.04	-0.02	InAs	-0.03	0.01
InN	0.97	-0.57	GaP	-0.07	0.03	GaSb	-0.12	0.06	ZnO	1.21	-0.51

Table 2.2: Piezoelectric constants for a variety of materials (in units of C/m^2) taken from reference [62]. III-Nitride piezoelectric constants are comparatively very high, and almost as high as those for ZnO (Values for III-Nitride compounds and ZnO are for the wurtzite crystal structure. All other compounds are zinc-blende structure).

The enhanced piezoelectric nature of III-Nitrides can have a profound effect on nanostructures realised from III-Nitride heterojunctions, which indeed undergo strain due to lattice mismatch between the constituent compounds, as we shall see in section 2.6.

2.6 The Quantum Confined Stark Effect

The presence of an internal electric field on a quantum confined nanostructure induces a red shift in emission, an increased radiative lifetime, and an emission broadening. These effects are collectively known as the quantum confined Stark effect (QCSE), which is most easily described and understood by imagining the effect of a small electric field on a planar quantum well (QW) of confinement energy such that any energy shift induced by the field may be treated as a small magnitude perturbation. The electric field acts as a perturbation on the ground state energies and wavefunctions of the QW, causing an energy shift and a separation in space of charge carriers.

The reduced wavefunction overlap caused by the spatial separation of the carriers results in a reduced recombination rate, and hence an increased emission lifetime. The effect is illustrated in figure 2.3.

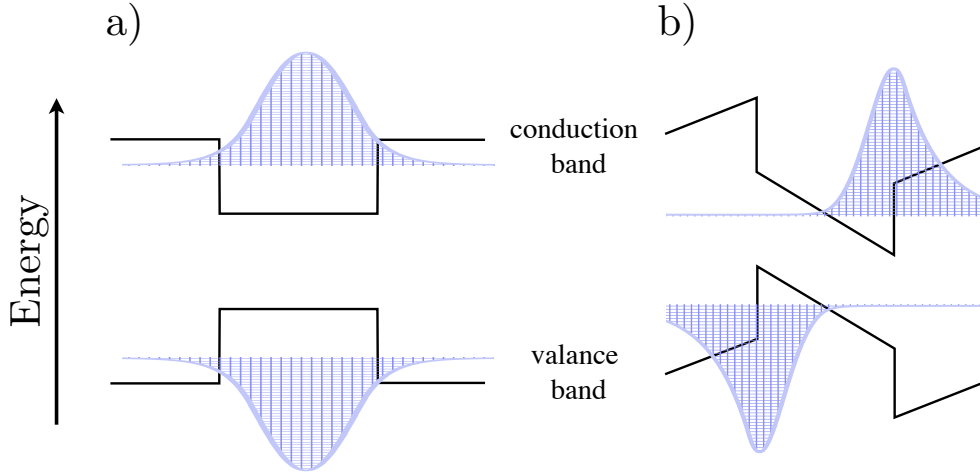


Figure 2.3: Simplified Band structure and ground state emission energy and wavefunctions of a) a finite quantum well, and b) the same well under the effect of an internal piezoelectric field.

In the case of an infinite potential well, to first order the change in energy of the bound states is zero (the overall integrand has -ve symmetry). In second order perturbation theory, the energy shift for the ground state of a quantum well under a field F along the z axis (perpendicular to the well) becomes:

$$\Delta E_1 = \sum_{k \neq 1} \frac{|\langle k | eFz | 1 \rangle|^2}{E_1 - E_k} \approx \frac{|\langle 2 | eFz | 1 \rangle|^2}{E_1 - E_2} = -\alpha F^2. \quad (2.16)$$

I.e. the energy shift is -ve and proportional to the square of the electric field.

Bastard *et al.* [65] used a variational technique to calculate the change of the wavefunction when under the influence of an applied electric field. For the case of a weak field in a finite potential well of width L (such that the change in energy level is small compared to the confinement energy), the wavefunction can be written as

$$\psi(z) = N(\beta)(1 + \beta z/L)\psi_0(z), \quad (2.17)$$

where β is the variational parameter with respect to which the energy will be minimised, and $N(\beta)$ is a constant of normalisation. This variation acts to shift the wavefunction along the axis of the field. Indeed, under these conditions, the shift in the energy is found to be negative, and proportional to the square of the applied electric field [65]. (The wavefunctions drawn in figure 2.3b) are representations of the kind in equation 2.17.)

Experimentally, the effects of an electric field on QW structures has been investigated by Miller *et al.*, who reported the non-linear red shift and broadening of exciton resonances in GaAs/AlGaAs quantum well structures [66]. The red shift in absorption/emission is the shift outlined above, and the broadening is suggested to occur due to possible non-uniformities in the electric field. Though in their simulations they find that the confinement provided by the QW is enough to preserve the exciton and prevent it from being ionised in the electric field, some extra broadening may be caused by the tunnelling of some carriers from the well [67, 66]. The broadening has been further experimentally verified in studies on III-nitride systems by Wang *et al.* [68], and Lai *et al* [69], and in various other material systems [70, 71, 72]. In early studies on InGaN QWs, the broadening due to the QCSE was rarely reported, as noted in reference [73], due presumably to poor material quality which resulted in broadened emissions (FWHM \sim 100 meV) caused by indium content fluctuations, which masked the QCSE induced broadening. These indium content fluctuations would cause the potential variation, resulting in localisation centres which give rise to the band tailing effect outlined in section 2.4.

The QCSE is generally perceived to be a nuisance to the production and realisation of any optoelectronic semiconductor device using III-Nitride materials, as it's main effect is to reduce the recombination efficiency and hence the device efficiency. In order to circumvent or combat the QCSE, many researchers have taken to growing non-polar *m*-plane GaN in which the electric field does not exist, or tried to produce columnar structures, which have less strain due to surface relaxation. Indeed, it is heterostructures in these nano-scale columnar structures that will form the majority of the work presented in this thesis. The growth of the columns will be outlined in section 2.8.

2.7 Defects and Dislocations

A further consequence of strain in a material is the occurrence of crystal dislocations. These usually appear when the strain in a layer becomes large enough that the material cannot sustain it, and it is more energetically favourable to have an abrupt change in the crystal lattice. Epitaxially grown GaN is well known to have many defects, due mainly to the lack of suitable substrate for growth (impurities introduced during growth may also act as crystal defects when they occupy a lattice point that should be occupied by gallium or nitrogen). Al_2O_3 , SiC and Si(111) are typically used substrates for the epitaxial growth of III-nitrides, but these have a lattice mismatch with GaN, such that the epitaxially grown material is under considerable strain, and will contain dislocations. The dislocation densities have been measured to be as high as $\sim 10^7 - 10^{11} \text{ cm}^{-2}$ [74, 75, 76]. These dislocations/defects act as potential traps for charge carriers, and hence as recombination centres, adversely affecting device performance [77]. One method to reduce the dislocation density in III-Nitrides, is to attempt epitaxial lateral overgrowth (ELOG), which results in reduced dislocation densities, and enables the fabrication of laser diodes [78]. Another method to grow GaN with reduced defect density is not to perform planar epilayer growth at all, but to grow columnar structures [79]. The enhanced surface to volume ratio of the nanocolumn allows for strain relaxation in the column and a huge suppression of the number of dislocations. A simulation of the strain state in a single GaN nanocolumn (100 nm diameter and 1 μm length) is shown in figure 2.4 In which it is clear that the column is largely relaxed, and that only the end of the column near the substrate (in this case Al_2O_3) is under any strain. The strain simulation process is described in the following chapter. It is also

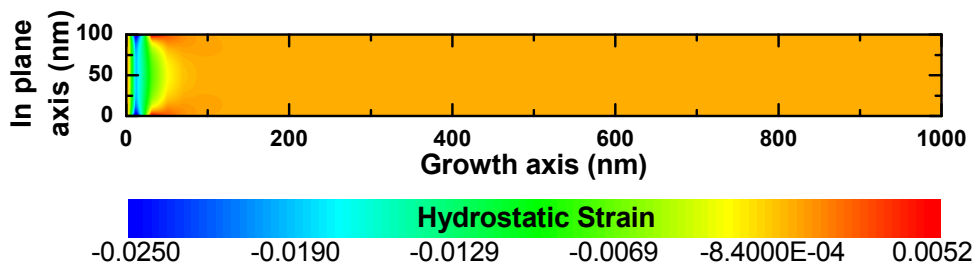


Figure 2.4: The distribution of hydrostatic strain in a 1 μm long GaN nanocolumn grown on an Al_2O_3 substrate. The majority of the column is strain free, resulting in high quality material growth.

possible to perform ELOG of planar GaN onto the columns with improved quality [80]. Indeed, LEDs have been produced in this way using AlGaN nanocolumns [81]. The growth of the GaN nanocolumns used in this investigation are described in the next section. For a review of the general properties of III-V nanocolumns/nanowires, the reader is directed to the review article by Joyce *et. al.* [82].

2.8 GaN Nanocolumns and their Growth Process

There are generally two ways to produce semiconductor nanocolumnar structures:

1. A *top down* approach, in which the columns are fabricated out of some material, usually involving lithographical masking and an etching technique.
2. A *bottom up* approach, in which the semiconductor material is grown under specific atmospheric conditions that favour the production of columnar structures.

The samples investigated in this study were produced by the bottom up method, as is outlined below.

The columns were grown under nitrogen rich conditions by RF-plasma assisted molecular beam epitaxy (PAMBE) on Si (111) substrates by Professor Y. S. Park of the Quantum-functional Semiconductor Research Centre at Dongguk University, Korea [83, 84, 85]. The MBE process involves the epitaxial (layer-by-layer) growth of single crystals on a substrate, in this case Si(111). The substrate is first degreased and etched using HF. It is then given thermal treatment at 1000 °C for 30 m before being kept under high vacuum in a reaction chamber and held at a constant, controllable temperature (900 °C). The elements that will make up the crystal are introduced into the chamber in the gaseous phase, where they condense on the substrate surface and form chemical bonds. In the case of GaN growth, the gallium source is a pure gallium cell that is heated such that a sublimation process occurs and atoms effuse into the chamber. The Nitrogen source is a pure nitrogen gas which is fed into an RF-plasma generator [86]. The plasma produces atomic nitrogen, which is then allowed into the growth chamber.

Gallium is expected to be highly mobile at typical MBE substrate temperatures ($\sim 800^\circ\text{C}$) as the Ga melting temperature is 302.9K. Zywietz *et al.* [87] have shown, however, that under nitrogen rich conditions the Ga mobility is reduced, owing to an increased migration inhibiting pseudo-potential barrier induced by Ga-N bonds. The reduced Ga mobility is theorised to lead to the formation of Ga clusters (Ga balling) which in turn become nitrogenated, forming GaN islands on the substrate surface. These GaN islands act as seeds for further GaN columnar growth. It is possible to control the physical parameters of the nanocolumns by careful control of the ambient conditions during growth. Increasing the temperature, for example, will result in a higher gallium desorption rate, which leads to smaller, and less dense Ga clusters and hence a lower density of GaN columns. The column length can be determined by the growth time. The GaN was grown directly on the prepared Si(111) substrate.

Consonni *et al.* [88, 89, 90] have shown that the transition between the formation of the islands, and the final columnar structures is a strain driven mechanism. The growth of nanowires/columns starts by the formation of coherent hemispherical islands, which change to hexagonal columns to reduce the strain energy at the surface and edges. In addition to this, Foxon *et al.* have shown that the geometry of the MBE chamber (the angle at which the gallium and nitrogen atoms impinge the surface) may also have an effect on the column parameters [91].

SEM images of the sample are shown in figure 2.5a,b,c). In agreement with previous results, [83, 84, 85] there appear to be two growth regimes present: The first being a compact region of GaN near to the substrate, resulting from the coalescence of low aspect ratio nanocolumns, and the second consisting of the higher aspect ratio nanocolumns. These columns are typically 140 nm in diameter and about 2-4 μm in length, with an estimated density of $1 \times 10^9 \text{ cm}^{-2}$. It is clear that the columns have a high aspect ratio, straight sidewalls and a hexagonal profile. In figure 2.5 d) a histogram can be found showing the distribution of column diameters (measured at the widest point).

Once the columns had grown to a length of about 2 – 4 μm , a $\sim 3 \text{ nm}$ thick $\text{In}_x\text{Ga}_{1-x}\text{N}$ quantum well layer was grown on top of the columns such that a single quantum disk was formed

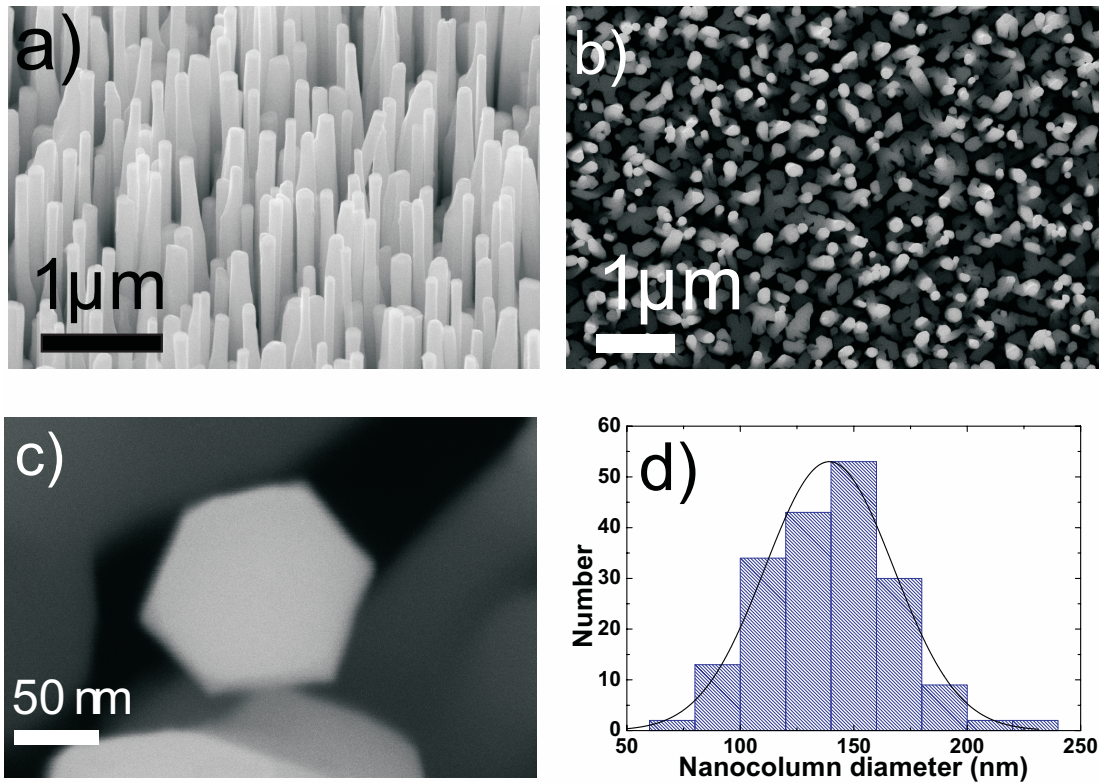


Figure 2.5: a) b) c) Scanning electron micrographs of the sample used in this investigation. d) Histogram of column diameters (measured at the widest point) showing that the average column diameter is ~ 140 nm.

on each column. The quantum disk is basically like a 2-dimensional quantum well, though with finite lateral extent limited to the diameter of the nanocolumn. The QDisk thus provides both a strong carrier confinement in the growth direction and a degree of lateral confinement. These disks were grown at reduced temperature (700°C) to facilitate the incorporation of indium, before being capped with another layer of GaN. The QDisks were nominally grown with an indium mole fraction $x = 0.1$, though some rudimentary calculations (see appendix B[¶]) lead us to believe that the real value is slightly lower than that (~ 0.07). The capping layer was also grown at the low temperature to stop the effusion of indium atoms from the QDisk during a temperature ramping process.

[¶]It is recommended to read chapter 5 before reading appendix B.

3

Modelling the Strain Distribution in an InGaN Quantum Disk/GaN Nanocolumn System, and Considerations on the Resulting Carrier Distribution

In this chapter strain simulations carried out on a GaN nanocolumn containing an InGaN QDisk are presented and discussed. The work presented here has been published in reference [92].

3.1 Strain Simulation Process

As there is no suitable, low-cost growth substrate for III-Nitrides, most research groups have been using Al_2O_3 substrates which are popular due to their relatively low price, stability at high temperature, transparency, and good crystal quality [36]. However, there is a $\sim 15\%$ lattice mismatch with GaN [36], which will induce strain into any GaN layer grown pseudomorphically to the substrate. As shown in chapter 2, strain can induce many effects that may be detrimental to device performance and is therefore an important issue for any technologist who wishes to build devices using III-Nitride semiconductor structures. In this chapter a commercial software package is used to simulate the strain in a single GaN nanocolumn/InGaN QDisk system due to lattice mismatch. A discussion is then given on how the strain distribution may affect the carrier distribution within the QDisk.

There are many software packages available that allow for the calculation of strain tensor elements. Nextnano³, which is freely available, and comes with a database of many material

parameters for a wide range of semiconductor materials [93], has been chosen for this study. In essence, the user has to just define the structure of the system to be evaluated, and `nextnano3` will then calculate the strain tensor elements by a process of minimising the overall strain in the system. A sample input file, along with explanation, for one of the simulations carried out during this study can be found in appendix D.

`nextnano3` utilises a continuum strain model [94], where a material grid is defined by the user and the strain is calculated at the grid points. The process of strain minimisation involves calculating the lattice parameters of the compounds in the constituent sections of the structure, and then allowing strain into the layers by enforcing pseudomorphic growth (the condition in which one layer is forced to have altered lattice parameter in order to match the layer below it). As this configuration will not necessarily be that with the lowest energy, `nextnano3` then allows for the relaxation of strain some areas and the increase of strain in other areas, and finds the value with the least overall strain energy (defined as the work done to distort the elastic medium). The strain minimisation process is outlined in references [93, 94, 95]. The calculation is an iterative process, and at each step the residual (difference between the strain energies of the current step and the previous pass) is calculated. Once the residual falls below a user-set value, the strain is said to have converged on the state of minimum strain energy, and the elements of the strain tensor corresponding to this minimum energy distribution are output as a function of position in the structure. It is these output files that will be analysed in this chapter.

3.2 The Strain Distribution in an InGaN Quantum Disk

To begin, a plot of the hydrostatic strain in a cross section (xz -plane) through the centre of a QDisk-containing nanocolumn is presented in figure 3.1. The QDisk has been modelled as a 3 nm thick hexagonal layer composed of $\text{In}_{0.1}\text{Ga}_{0.9}\text{N}$. For comparison, a bright field micrograph obtained from a transmission electron microscope (TEM) of the tip of a single nanocolumn is presented in the same figure. The hydrostatic strain is defined as $\epsilon_{\text{hyd}} = \epsilon_{xx} + \epsilon_{yy} + \epsilon_{zz}$, and literally corresponds to the local volume change of the system under consideration due to strain.

The QDisk is represented by the area of relatively high compressive ($\epsilon_{\text{hyd}} < 0$) strain near the tip of the column. Due to the minimisation of the strain energy, it is clear that some strain is induced into the nanocolumn by the presence of the QDisk. During the simulation the side walls of the column are kept rigid (a limitation of the simulation software), whereas in the TEM image it is clear that there is some change in column diameter near the tip. This could quite probably be due to the strain imparted into the column by the QDisk, but could also be due to an increased lateral growth rate when the indium is added to the system, or a small amount of lateral overgrowth during the capping process.

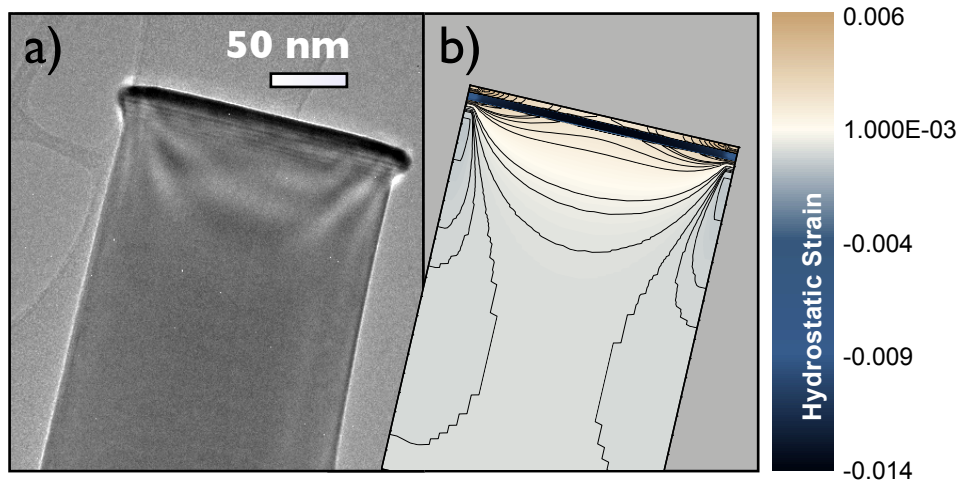


Figure 3.1: a) TEM micrograph of the tip region of a single GaN nanocolumn containing a single InGaN QDisk. b) The simulated hydrostatic strain $\epsilon_{\text{hyd}} = \epsilon_{xx} + \epsilon_{yy} + \epsilon_{zz}$ throughout a cross section (xz -plane) of the tip of a GaN nanocolumn containing a single $\text{In}_{0.1}\text{Ga}_{0.9}\text{N}$ QDisk of width 3 nm.

It is clear that to some extent, the simulated strain in the column mimics that which is observed in the whole column, although direct comparison can only be made with the caveat that the TEM image is an integration of the whole body of the column, whereas the simulation projection is of a single plane crossing through the centre of the column.

A higher resolution image of just the tip of the column, focussing on the region of the QDisk is presented in figure 3.2. In this figure we show the ϵ_{xx} component of the strain tensor (the other simulated components ϵ_{ij} for the same region in space can be found at the end of this chapter, in figure 3.11). As could be expected, the strain tensor takes a negative value (compressive strain) in the centre of the QDisk owing to the larger in-plane lattice constant of

$\text{In}_{0.1}\text{Ga}_{0.9}\text{N}$ in comparison to the underlying, and capping GaN layers.* Interestingly, a direct consequence of the free surface at the side wall is that the strain becomes somewhat reduced in the vicinity of the the side wall: It becomes more energetically favourable for the $\text{In}_{0.1}\text{Ga}_{0.9}\text{N}$ QDisk to become unstrained, and consequently the surrounding GaN layer becomes strained. The distribution of ϵ_{xx} calculated here compares well with those published for similar structures [96, 97, 98, 99, 100, 101], albeit with reduced magnitude owing to the lower indium content of the QDisk in this investigation: ϵ_{xx} varies by nearly 2 orders of magnitude from from -1.1% at the centre of the disk to an almost completely relaxed value of -0.05% at the edge. Loosely speaking, at the edge of the QDisk, the GaN layer is forced to have the $\text{In}_{0.1}\text{Ga}_{0.9}\text{N}$ lattice parameter, and the QDisk becomes further relaxed.

This inhomogeneity in strain distribution is a direct consequence of the columnar nature of the sample, and could theoretically have drastic implications on how photo-excited carriers may be distributed within the column/QDisk system. The distribution of these carriers is considered in terms of a broad change of confining potential, and band edge energies in the following section.

In the high resolution simulation, the bottom of the simulated area was set to have 0 strain. This is deemed reasonable as the column itself is almost fully relaxed (as shown in figure 2.4).

*This in plane compression results in a perpendicular tensile strain in the QDisk, as can be observed in the ϵ_{zz} component in figure 3.11.

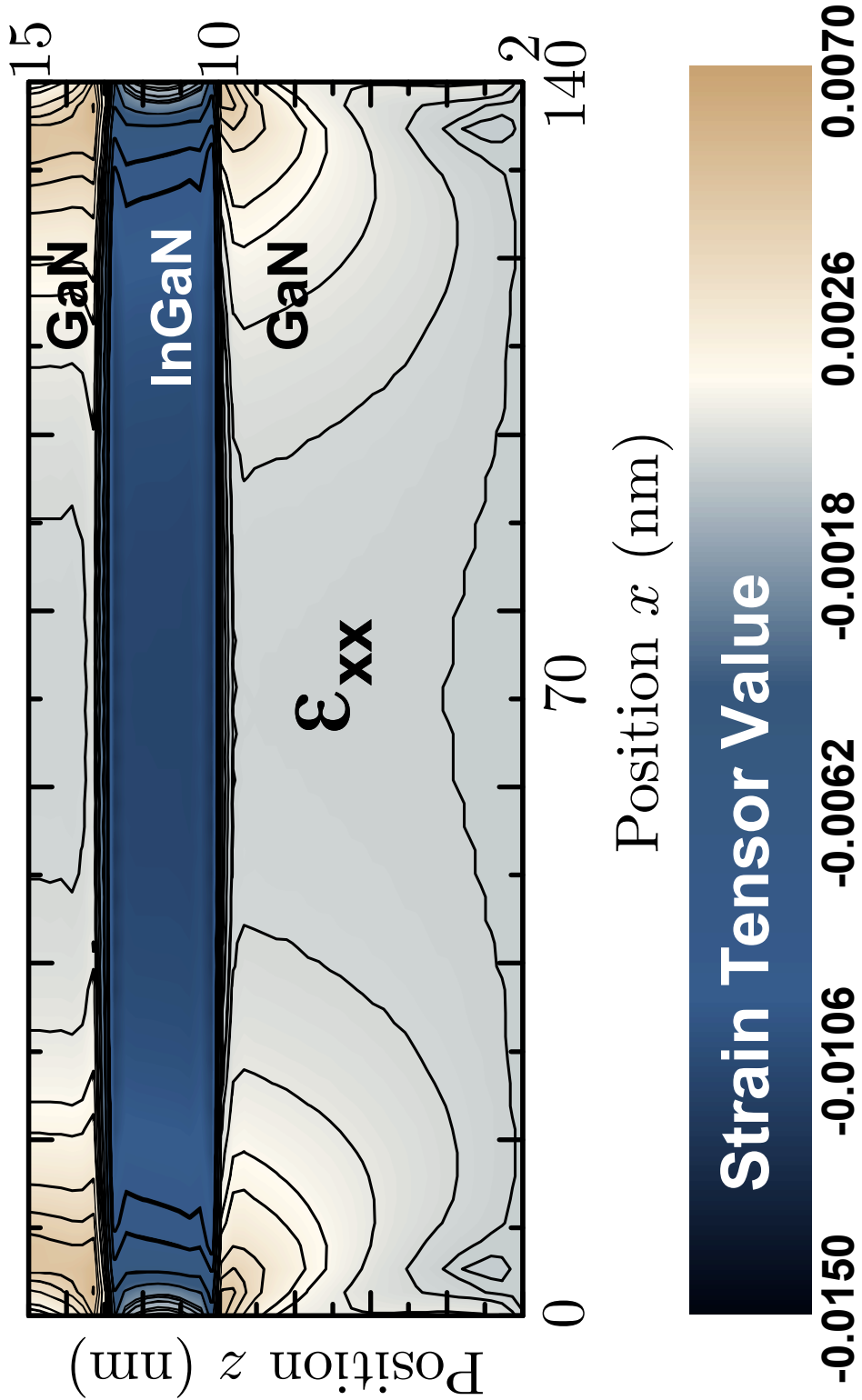


Figure 3.2: the ϵ_{xx} component of the strain matrix in a cross section (xz -plane) through the tip of a GaN nanocolumn containing a single $In_{0.1}Ga_{0.9}N$ QDisk of width 3 nm.

3.3 On the Resulting Carrier Distribution

There are 3 effects which should be given due attention when considering what, if any, the effect of an inhomogeneous strain distribution will have on the carrier distribution and dynamics within the nanocolumn/QDisk system: The (previously discussed) piezoelectric effect, the effect of deformation potentials, and the effect of Fermi surface pinning. These will be individually addressed in sections 3.3.1, 3.3.2 and 3.3.3, respectively.

3.3.1 Piezoelectric Effect (QCSE)

As discussed in the previous chapter, the presence of an electric field in a quantum well structure will invoke the quantum confined stark effect and create an inhomogeneous distribution of charge along the direction of the field. Bastard *et al.* [65] have shown that the energy levels bend with the square of the applied field. As there is an inhomogeneous distribution in the strain across the diameter of the QDisk, it follows that one may expect there to be an inhomogeneous piezoelectric field (the field is stronger in the middle of the QDisk) which will lead to a bending of the conduction and valence bands along the diameter of the QDisk. This effect, *when considered alone*, would cause a carrier distribution such that electrons and holes will find themselves preferentially distributed in the lower energy states existing in the central region of the QDisk.[†] This effect is illustrated in figure 3.3, where the size of the electric field in the QDisk was approximated by

$$E_z^{\text{piezo}} = \frac{\Delta P_z}{\epsilon_0 \epsilon_r}, \quad (3.1)$$

and the piezoelectric polarization, P_z , by equation 2.15. Values of e_{13} and e_{33} were taken from table 2.2 and ϵ_r was set to 10 [36], as the indium content is low in the simulation (10%). The total field in the QDisk will be generated by the differences in polarisation at the QDisk/GaN interface due to both spontaneous and piezoelectric polarizations. However, the spontaneous polarization in InN and GaN are very similar, so that the contribution due to the change in

[†]Of course, they will be still be separated in the growth direction.

spontaneous polarization at the InGaN/GaN interfaces can be neglected in this case [102].

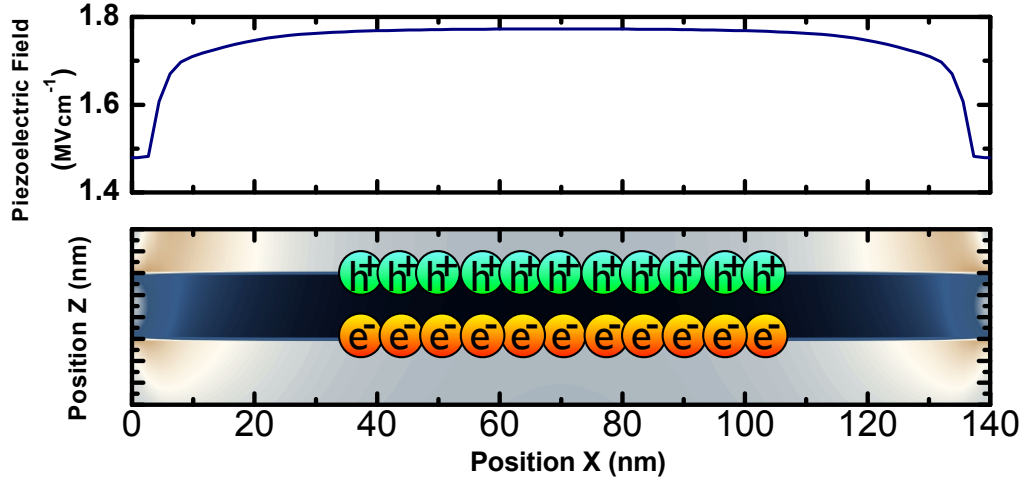


Figure 3.3: A plot of the simulated z -component of the piezoelectric field as a function of position along the diameter of the QDisk. The lower image shows the supposed position of charge carriers due to the lowering of energy by the field.

The spontaneous polarization cannot, however, be neglected at the top (free) surface of the nanocolumn. Here, as the vacuum polarization is 0, The field generated by the sheet of charge at the top surface of the column is given by

$$E_z^{\text{spont}} = \frac{P_{\text{GaN}}^{\text{spont}}}{\epsilon_0 \epsilon_r}, \quad (3.2)$$

where $P_{\text{GaN}}^{\text{spont}} = -0.034 \text{ Cm}^{-2}$ [103]. On assumption that this charge sheet is evenly distributed across the cross-section of the column, the generated field will be uniform across the diameter of the QDisk. The magnitude of this field is estimated to thus be $\sim -1.9 \text{ MVcm}^{-1}$. When this field and previously calculated piezoelectric field are added, the total electric field in the QDisk takes a different profile, as shown in figure 3.4. The carriers, then, will find lower energy states at the edges of the QDisk, and may be found distributed there. This analysis depends on a full understanding of the charge density at the surface, which is unknown at present. It is possible that the free-surface charges due to ΔP^{spont} become trapped in surface states, and that the induced field is reduced. Further screening of this field and band bending may result in a field with much lower magnitude than 1.9 MVcm^{-1} in the QDisk region. In short, the total effect of

these two fields could then be to distribute the carriers a) in the centre of the disk as illustrated in figure 3.3, or b) at the edges as in figure 3.4 depending on their relative strengths. Mojica and Niquet produced a theoretical analysis of the polarization and piezoelectric field in a GaN QDisk surrounded by AlGaIn layers on top of a GaN nanocolumn [104]. They showed that the spontaneous polarization change at the top and at the lower AlGaIn/GaN interface generate an electric field which acts to screen the piezoelectric field in the QDisk. However, in their analysis they didn't account for the lateral strain relaxation, which acts to produce a region in which there still exists an electric field, capable of generating the QCSE. Further understanding of the situation in hand will require the dedicated work of a theoretician.

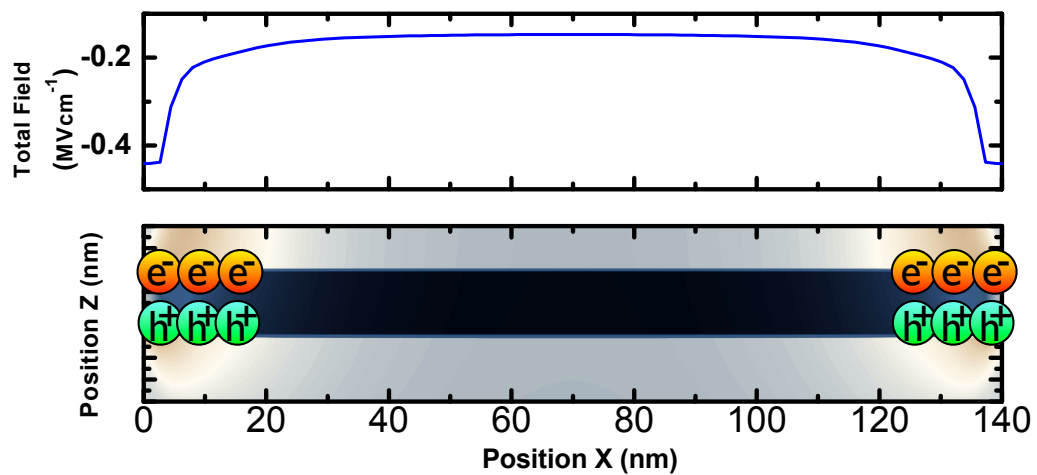


Figure 3.4: A plot of the simulated z-component of the total electric field (piezoelectric plus supposed screening from surface states) as a function of position along the diameter of the QDisk. The lower image shows the supposed position of charge carriers due to the lowering of energy by the field.

3.3.2 Deformation Potentials

Strain has a direct effect on the conduction and valence band edges (CBE,VBE), which is controlled by the so-called deformation potentials [105, 106]. For the case of a diagonal strain

tensor (satisfied in the present study), the shifts of the CBE and VBE are given by;

$$\Delta E_{\text{CBE}} = a_1 \epsilon_{zz} + a_2 (\epsilon_{xx} + \epsilon_{yy}), \quad (3.3)$$

$$\Delta E_{\text{VBE}} = D_1 \epsilon_{zz} + D_2 (\epsilon_{xx} + \epsilon_{yy}) + D_3 \epsilon_{zz} + D_4 (\epsilon_{xx} + \epsilon_{yy}), \quad (3.4)$$

where a_1 and a_2 are the conduction band deformation potentials and D_{1-4} are the relevant valence band deformation potentials. Values of $a_{1,2}$ and D_{1-4} for GaN from the literature can be found in table 3.1. It is clear that the research community have not settled on well defined

	a_1 (eV)	D_1 (eV)	a_2 (eV)	D_2 (eV)	D_3 (eV)	D_4 (eV)
Chuang(1997) [106]	-8.16	-0.89	-4.08	4.27	5.18	-2.59
Vurgaftman(2003) [107]	-4.9	-3.7	-11.3	4.5	8.2	-4.1
Riviera(2007) [100]	-6.5	-3.0	-11.8	3.6	8.82	-4.41
Yan (2009) [108]	$a_1 - D_1 = -5.81$		$a_2 - D_2 = -8.92$		5.47	-2.98

Table 3.1: Values of the deformation potentials for GaN taken from various references in the literature.

values of these potentials, due mainly to the large difficulties in measuring them and the range of techniques used to theoretically predict their values.

In the same way as was done above for the strain induced piezoelectric field, it would be constructive to see how the strain induced change in band gap varies along the diameter of the column. Due to the compressive strain in the QDisk ($\epsilon_{xx}, \epsilon_{yy} \leq 0$), the CBE and VBE are found to bend so that their respective minimum energy points are found at the QDisk sidewall, as can be seen in figure 3.5. Under the effect of deformation alone, then, carriers are likely to be distributed at the periphery of the QDisk. In this calculation the deformation potentials from reference [107] for GaN were used in the calculation for $\text{In}_{0.1}\text{Ga}_{0.9}\text{N}$ as the difference between parameters for the two systems was deemed to be less than the uncertainty in the values stated for GaN.

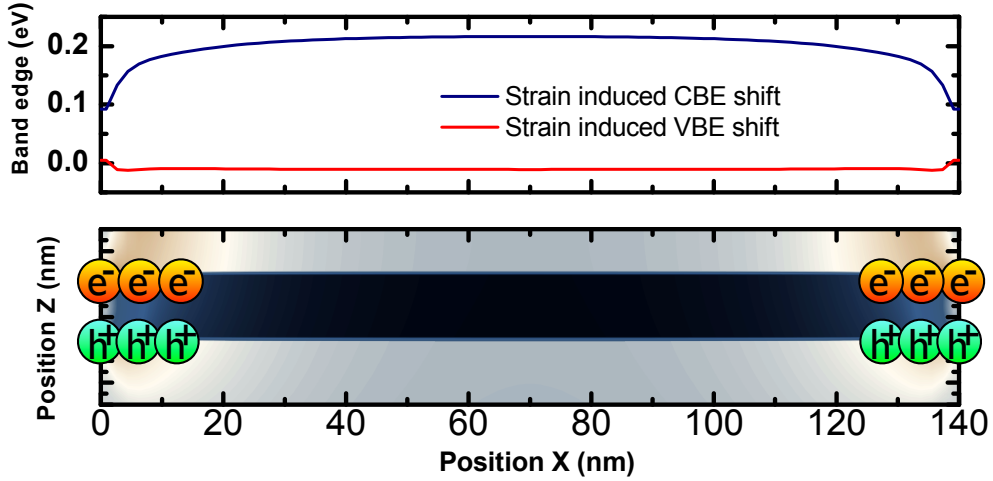


Figure 3.5: A plot of the simulated change to the conduction and valence band edges along the diameter of the QDisk when taking deformation into account. The lower image shows the supposed position of charge carriers due to the lowering of energy by the field.

3.3.3 Fermi-surface Pinning

A final contribution to the bending of bands across the diameter of the nanocolumn is Fermi surface pinning (FSP) [109, 110]; the effect by which the bands bend due to a pinning of the Fermi level at free surfaces. This effect is thus important in thin GaN nanocolumns which exhibit large surface to volume ratios. The band bending creates a charge depletion (or accumulation) region near to the free surface, which in the case of very thin nanocolumns (diameter $\leq \sim 80$ nm) is almost completely insulating [109]. This insulating region can have negative effects on device performance. The effect is described below, and, as in the previous two subsections, a plot of the energy states and predicted carrier distribution is given in figure 3.7.

The existence of surface states within the band gap at the semiconductor vacuum interface allow for the diffusion of charge from the bulk of the material near to the surface into the surface states forming a depletion region. The resulting reduction in Fermi energy relative to the conduction and valence band causes the bands to bend down into the bulk of the system. As the density of surface states is high (approximately equal to the number of atoms at the surface) the Fermi-energy is said to become pinned. In a simple model, we can assume that the width of the depletion region is ω_{dep} and that all of dopants (of density N_D) are ionized

in the depletion region. Upon solving the Poisson equation (with boundary conditions that $V(\omega_{\text{dep}}) = dV/dx|_{\omega_{\text{dep}}} = 0$)

$$\frac{d^2V}{dx^2} = \frac{-eN_D}{\epsilon_r\epsilon_0} \Rightarrow V(x) = \frac{-eN_D}{2\epsilon_r\epsilon_0}x^2 + Bx + C = \frac{-eN_D}{2\epsilon_r\epsilon_0}(x - \omega_{\text{dep}})^2 \quad (3.5)$$

it is revealed that the bending of the bands is quadratic into the material. The process is shown in figure 3.6. Using equation 3.5 it is possible to evaluate the relation between the barrier height (Φ_B), which is the change in potential across the depletion region, and ω_{dep} :

$$\omega_{\text{dep}} = \sqrt{\frac{2\epsilon_r\epsilon_0\Phi_B}{eN_D}} \quad (3.6)$$

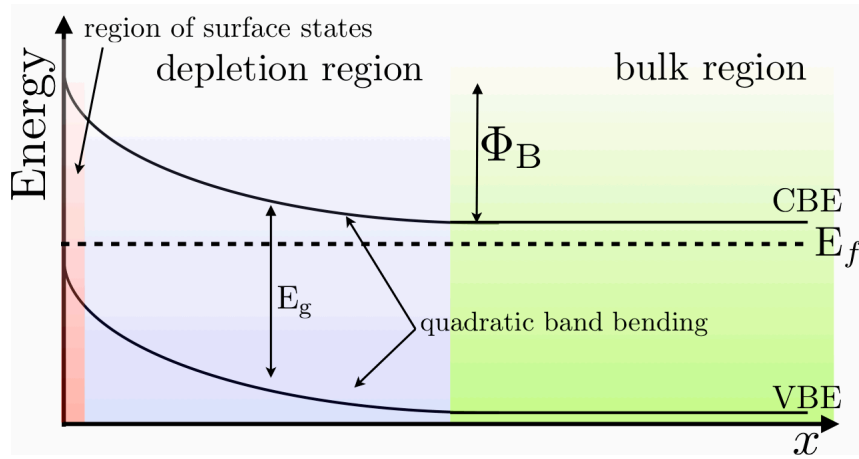


Figure 3.6: The bending of the conduction and valence bands in the depletion region formed due to Fermi surface pinning.

There have been several studies on the effect of FSP in III-nitrides [111, 110, 109, 112, 113, 114, 115]. It is found that the Fermi surface is pinned within the band gap for pure GaN and low indium content $\text{In}_x\text{Ga}_{1-x}\text{N}$, and is pinned above the conduction band edge (CBE) for InN and high indium content $\text{In}_x\text{Ga}_{1-x}\text{N}$ [111]. The size of the barrier, Φ_B is experimentally determined to be 0.3 eV for $\text{In}_{0.1}\text{Ga}_{0.9}\text{N}$, which implies an expected depletion length of ~ 18 nm into the column (assuming a typical intrinsic GaN donor density N_D of 10^{17}cm^{-3}).

For similar GaN nanocolumns, it has been shown that the depletion region due to the pinning induced band bending can extend for about ~ 50 nm into the body of the column from

the surface [109, 115]. In this case, for the purpose of explanation, the Fermi-surface pinning was modelled in the disk as having a barrier height Φ_B of 300 meV, and extending into the nanocolumn quadratically as per equation 3.5 with a depletion width $\omega_{\text{dep}} = 18$ nm. The band bending and resulting carrier distribution is presented in figure 3.7. In this case the electrons gather near the centre of the QDisk and the holes are to be found in the regions near to the edge.

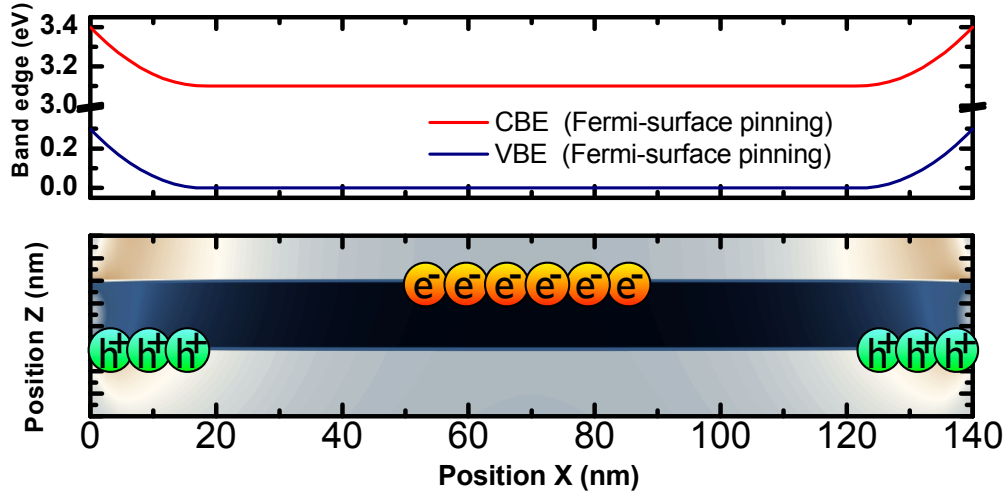


Figure 3.7: A plot of the simulated conduction and valence band edges along the diameter of the QDisk when taking into account Fermi-surface pinning. The lower image shows the supposed position of charge carriers due to the lowering of energy by the field.

3.4 Combination of effects

The 3 effects outlined above individually cause drastically different carrier distributions within the QDisk. The carrier distributions due to the QCSE and the deformation potentials are direct consequences of the inhomogeneous strain distribution, whereas the Fermi pinning occurs regardless of the strain state.[‡] Combining the 3 effects over the 3D grid in the hexagonal column requires considerable computing power (often the simulations do not converge before the limited memory becomes an issue) so here we apply a qualitative treatment of the relative effects and compare to simulations that have been carried out in similar systems by other research

[‡]Provided that the strain doesn't shift the surface states energy band to an energy that is not bounded by the CBE and VBE.

groups. We start by separating the carrier distribution into two orthogonal distributions; a) the distribution along the growth axis of the disk, and b) the in-plane distribution.

a) The carrier distribution along the growth axis

The strain distribution is fairly homogeneous along the growth direction at any given radial coordinate within the QDisk. We should therefore not expect there to be any change in energy of the CBE, VBE within the QDisk directly due to the strain. Hence, the only bending of these bands will be due to the inbuilt electric field, as outlined in section 2.6. A one dimensional simulation of this can easily be performed with `nextnano`³; the output can be found in figure 3.8.

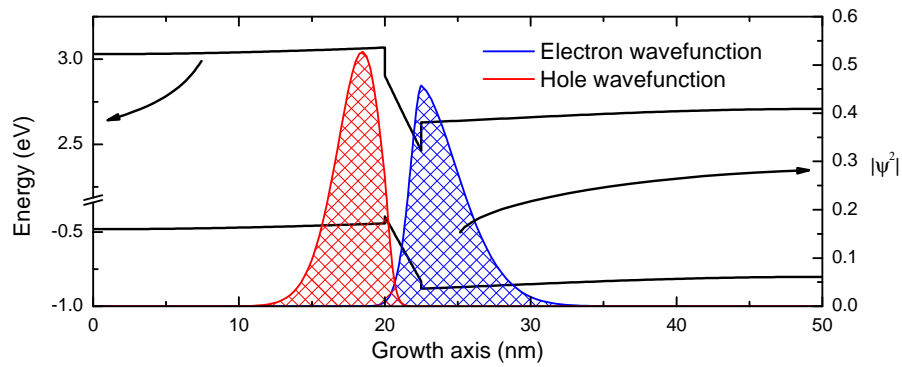


Figure 3.8: One dimensional simulation of an 3 nm thick $In_{0.1}Ga_{0.9}N$ quantum well, corresponding to the situation in the centre of the QDisk.

The effect of the QCSE is to separate the electrons and holes along the growth direction, and the simulation provides us with some idea of the extent of carrier separation that will occur at the centre of the QDisk. In this case the transition energy is 3.1 eV and the wavefunction overlap $|\langle \Psi_{h+} | \Psi_{e-} \rangle|^2$ is just 0.3%. The effect will be come less pronounced towards the edge of the QDisk due to the reduced electric field.

b) The in-plane carrier distribution

The in-plane carrier distribution is far more difficult to analyse quantitatively, and the uncertainty in values for the deformation potentials, and the Fermi pinning barrier, Φ_B , within the

QDisk mean that actual calculated wavefunctions could be speculative at best. Indeed, the induced band bend bending by all 3 effects seem to be of order 10 – 100 meV, and all effects occur within ~ 50 nm of the column side wall. When this uncertainty is coupled with the vastly increased processing power and memory required to produce 3D simulations of this kind, it seems prudent to just give a general discussion on what carrier distributions may arise, and how we could experimentally distinguish them. In the simplest case, the relative strength of the effects outlined in the sections above will determine the overall carrier distribution: If the band bending due to the piezoelectric field is dominant, the resulting carrier distribution will be centred on the QDisk centre. If the deformation is dominant, the carriers will be distributed towards the QDisk edge. If Fermi pinning is dominant, the carriers will be separated in the plane of the disk.

A further complication arises in that, for the cases of deformation and the QCSE, the size of the effect is different in the conduction and valence bands. In the case of deformation potentials, it is clear in figure 3.5 that the degree of band bending is different for both the CBE and VBE, and for the case of the QCSE, the carrier effective mass contributes to the size of the effect, and holes shift less in energy for a given field. This could mean, for example, that while band bending due to deformation is dominant for the CBE, the effect of energy state lowering due to the internal field is dominant for the holes in the valence band; this could also produce a lateral separation of carriers in the QDisk [100, 116, 98].

Indeed, Böcklin *et al.* [116] have calculated that for a (relatively high indium content) $\text{In}_{0.4}\text{Ga}_{0.6}\text{N}/\text{GaN}$ QDisk system, the electrons may be confined at the periphery of the disk, and the holes at the disk centre. This is in contrast to the situation in GaN/AlGaIn QDisk systems where, according to the calculations of Riviera *et al.* [100] it is the electrons that are to be found at the centre of the disk, and the holes at the edges. It should also be noted that the effects of Fermi level pinning at the free surface of the disk have been ignored in models of the two cases outlined above.

It follows that it is quite plausible that, in the special case of low indium content InGaIn QDisks, the three effects in the conduction band (deformation leading to confinement at the

edge, and both polarization fields and Fermi pinning which lead to confinement at the disk centre) can sum to reveal a conduction band that doesn't strongly confine electrons in any one lateral position in the QDisk. Holes, on the other hand, may still be strongly localised, as the deformation of the valence band due to the inhomogeneous strain distribution is not as severe. This situation could lead to a reasonable wavefunction overlap and result in decay lifetimes not too dissimilar to those from planar QWs.

3.5 Additional work on multiple QDisk stacks

In addition to the work on simulations of the strain distribution in a single QDisk presented above, strain distributions have been carried out for nanocolumns containing stacks of 2 and 5 QDisks. The ϵ_{xx} components of the strain tensor in the xz -plane cross section for columns containing 1, 2 and 5 QDisks can be found in figure 3.9. An interesting aspect of these simulations is that as the cumulative strain in the column increases due to the introduction of each successive QDisk, so does the strain in each individual disk decrease. This effect is illustrated in figure 3.10, where, in the case of 5 QDisks, it is clear that the strain at the centre of each successive disk becomes successively reduced. Hence the introduction of a QDisk stack can be seen as a way to artificially engineer the QDisk strain for a particular active region in a device that one may chose to manufacture. However, the observation that the strain at the edge of the QDisks does not reduce with the number of disks may indicate that there is a limit to the amount of strain engineering possible with this method. The investigation of multiple QDisks has not been taken further than this preliminary stage at present, and is left as a project for future work.

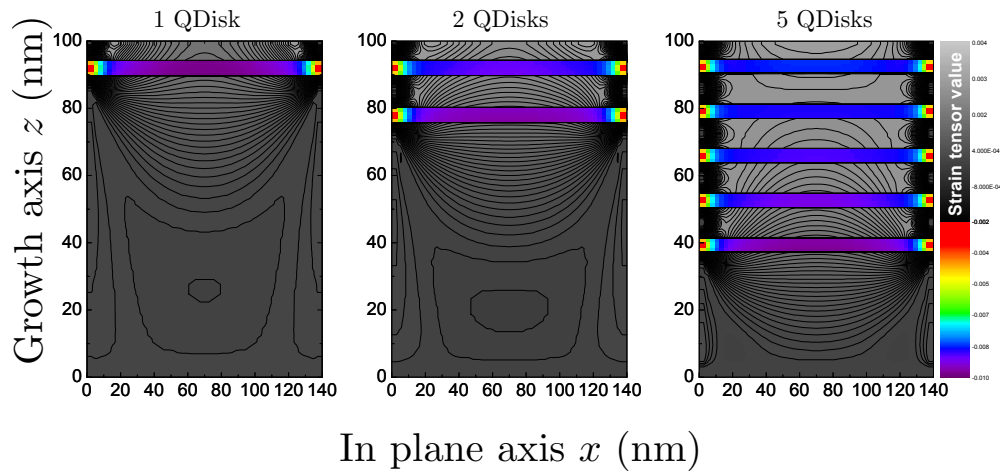


Figure 3.9: the components of the ϵ_{xx} strain element in a cross section (xz -plane) through the tip of GaN nanocolumns containing 1, 2 and 5 $\text{In}_{0.1}\text{Ga}_{0.9}\text{N}$ QDisk of width 3 nm.

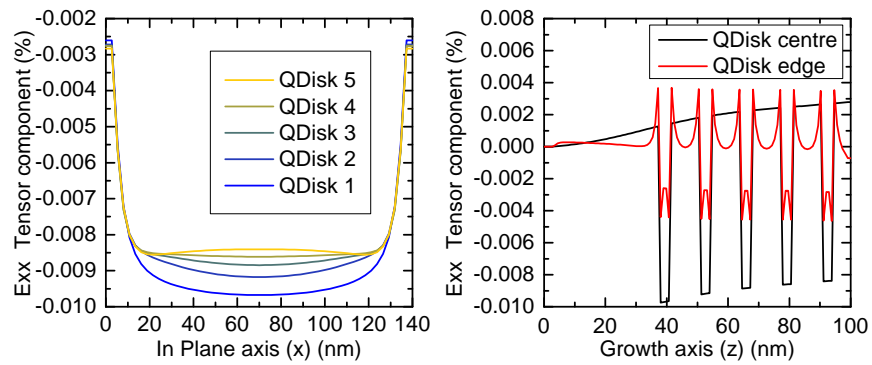
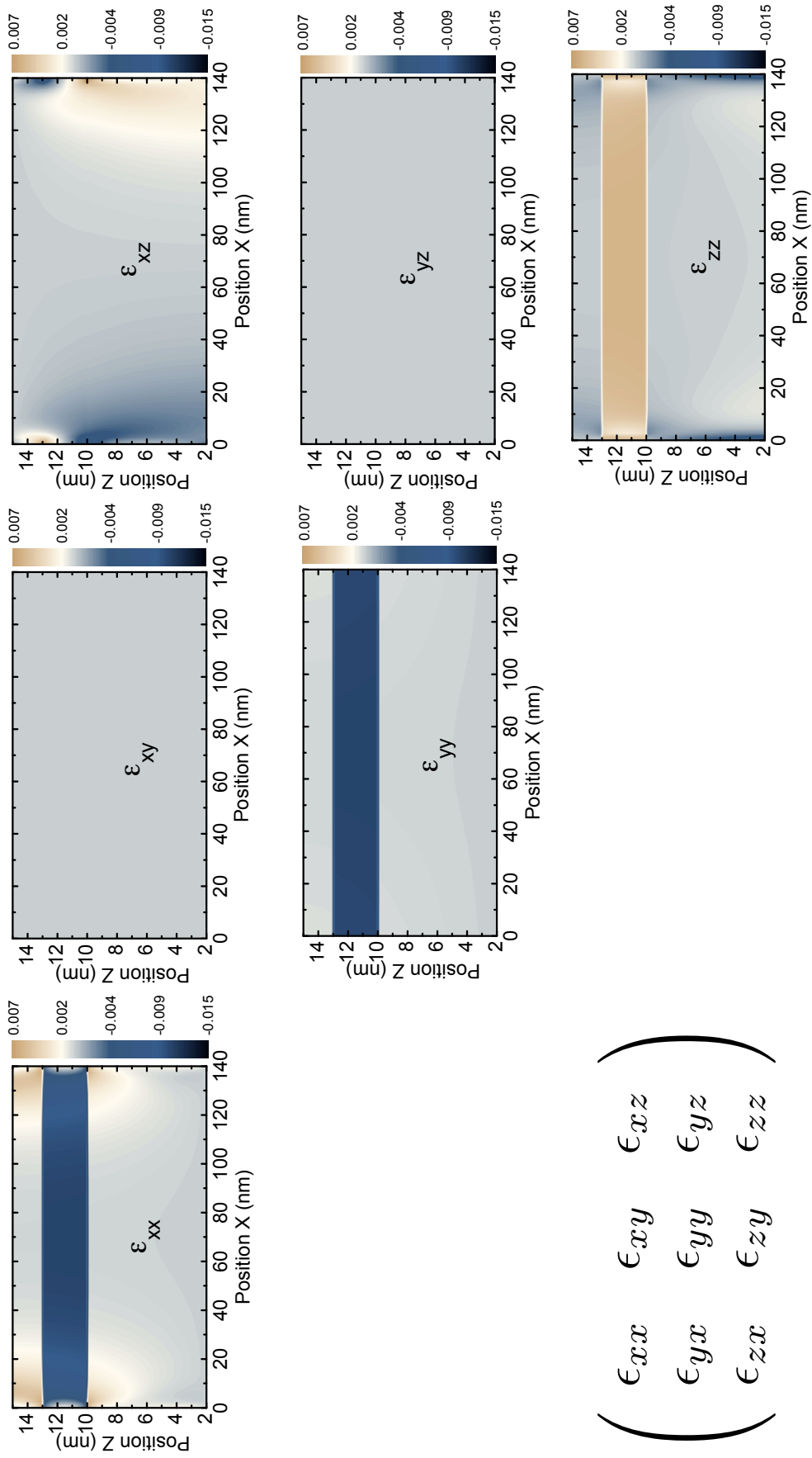


Figure 3.10: the components of the ϵ_{xx} strain element in a line sections along the diameter of the disks, and through the nanocolumn at the centre and edge, for a system with 5 QDisks.



$$\begin{pmatrix} \epsilon_{xx} & \epsilon_{xy} & \epsilon_{xz} \\ \epsilon_{yx} & \epsilon_{yy} & \epsilon_{yz} \\ \epsilon_{zx} & \epsilon_{zy} & \epsilon_{zz} \end{pmatrix}$$

Figure 3.1.1: the components of the strain matrix in a cross section (xz -plane) through the tip of a GaN nanocolumn containing a single $In_{0.1}Ga_{0.9}N$ QDisk of width 2.5 nm.

4

Experimental Techniques

4.1 Introduction

The vast majority of experimental techniques used throughout this study involve the optical excitation of charge carriers in a given sample and somehow detecting the resulting photoluminescence (PL) from the sample. When the photoluminescence is spectrally dispersed and integrated over time one can attain the emission spectrum of the sample. The power and wavelength of the emission source can then be varied to observe certain effects in the sample's emission spectrum. If however, the arrival time of the photons emitted from the sample is collated, one can produce a histogram mimicking the decay statistics of the sample, from which the lifetime of the carriers can be inferred. In section 4.2 we will describe the various excitation sources used for the experiments, before looking in depth at the two main experimental techniques; time integrated-, and time resolved- microphotoluminescence studies, in sections 4.3 and 4.4, respectively. Further cleanroom techniques for the fabrication of masks and grids used for experiments where a higher degree of spatial resolution is required will be outlined in section 4.5.

4.2 Excitation Sources

4.2.1 Ti:Al₂O₃ Laser

A Titanium Sapphire (Ti:Al₂O₃) laser is a amplifier in which the active medium is a titanium ion (Ti³⁺) doped sapphire crystal [117]. The laser can be used to generate laser emission at

wavelengths between ~ 700 and ~ 1000 nm in both continuous wave and pulsed (mode locked) operation. Two models of Ti:Al₂O₃ laser were utilised during this study:

- A *Coherent* Mira[®] 900 series with Kerr lens modelocking (KLM), capable of producing both picosecond and femtosecond pulses. Pumped by a *Coherent* Verdi V8 diode laser ($\lambda = 532$ nm) the Mira 900 can produce emission between 700 – 1000 nm at powers of up to 1.5 W.
- A *Spectra-Physics* Mai Tai[®] series capable of producing emission between 795 – 805 nm at an average power of 800 mW. The Mai Tai is also pumped by a 532 nm diode laser, and produces pulses of duration 100 fs at 80 MHz by KLM.

An explanation of KLM can be found in appendix A

4.2.2 2nd and 3rd Harmonic Generation: Ultrafast Pulses at 400 and 266 nm

A commercial Inrad 5-050 Ultrafast Harmonic Generation System was used to produce 2nd and 3rd harmonics from the Ti:Al₂O₃ amplifier. The system comprised of a non-linear birefringent lithium triborate (LiB₃O₅) crystal onto which the 800 nm beam from from the Ti:Al₂O₃ was focussed. The crystal was positioned such that the phase matching condition was met for frequency upconversion. The output from the crystal thus consisted of 800 nm and 400 nm components. If required, the 400 nm beam could be used for an experiment, however with the aid of a delay line it is possible to temporally overlap the fundamental and 2nd harmonic by the use of a delay line before adding them together using a 2nd non-linear crystal, this time a beta-barium borate (β -LiBaB₂O₄), to generate the 3rd harmonic at 266 nm.

The internal setup of the harmonic generator is presented in figure 4.1. The delay arm is used to force a temporal overlap of the $\lambda = 800$ nm pulses and the $\lambda = 400$ nm at the second non-linear crystal. The filter at the output coupler is used to prevent any remaining 400 and 800 nm pulses from leaving the system, though indeed the 800 nm beam could be directed through a different output and used as a time base (80 MHz) for time resolved experiments. At a typical

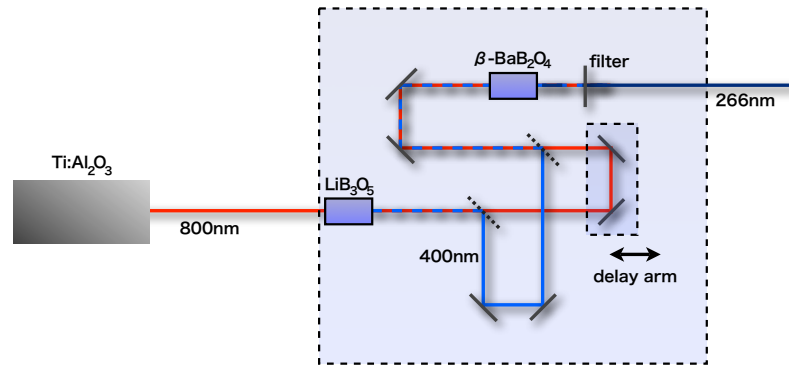


Figure 4.1: Internal setup of the Inrad 5-050 Ultrafast Harmonic Generation System.

input power of 800 mW, a ~ 100 mW 2nd harmonic, or a ~ 12 mW 3rd harmonic could be generated.

4.3 Time Integrated μ -Photoluminescence Studies

Time Integrated μ -Photoluminescence (TIPL) is a technique in which an excitation source is focussed to a spot size of $\sim 1 \mu\text{m}$ on a sample to be measured. The resulting photoluminescence is then collected and collimated by the same objective lens and directed to a grating spectrometer where it is spatially dispersed before falling upon a charge coupled device (CCD) and detected as an intensity distribution over wavelength (spectrum). Figure 4.2 shows a (simplified) schematic of a typical experimental set up in which a frequency tripled Ti:Al₂O₃ laser operating at 266 nm is used as the excitation source.

The micron size laser spot enables a high degree of spatial resolution and thus facilitates the ability to excite just a few nano-structures at a given time. Furthermore, a mask can be created (see section 4.5) such that one can locate nano-structures and carry out optical excitation experiments on them over an indefinite time period.

The experimental setup used in this investigation consists of a pulsed Ti:Al₂O₃ laser that is frequency tripled to 266 nm. The tripled beam is focussed to a spot size of $0.8 \mu\text{m}^2$ by a $36\times$ reflecting objective (Ealing EA-25-0522-000) with a working distance of 8.6 mm and coated so that the average reflectivity is 89 % in the wavelength range 250 nm-10 μm [118]. The numerical

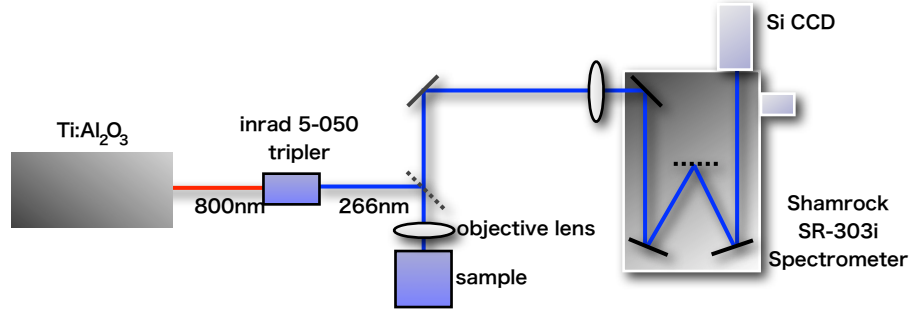


Figure 4.2: A schematic of a typical TIPL experimental setup. The excitation source is focussed upon the sample and the resulting PL is collimated and directed to a grating spectrometer.

aperture of the lens is 0.5. The sample was mounted in a continuous flow helium cryostat (Janis ST-500) with an attached temperature controller (Lakeshore 331) such that the temperature could be measured and controlled accurately between 4.2K and room temperature. The cryostat was equipped with a fused silica window to enable the excitation with, and the collection of, UV light. PL was collected by the same objective and focussed into a 303 mm focal length diffraction grating spectrometer (Andor Technology Shamrock SR-303i) [119]. The PL was dispersed in the spectrometer by a 1200 lmm^{-1} reflecting grating (500 nm blaze) before being measured on a Peltier-cooled silicon charged coupled device (CCD). The CCD used is an *Andor Technology* DU420A-BV device which consists of an array of 1024×255 pixels (full vertical binning was utilized) of size $26 \mu\text{m} \times 26 \mu\text{m}$ [120]. The CCD was cooled to -70°C to reduce thermal noise, and bring down the dark count rate.

The *reciprocal linear dispersion* of such a grating spectrometer (of focal length f and a grating of line spacing d) can be calculated by

$$\frac{d\lambda}{dx} = \frac{d}{f}, \quad (4.1)$$

and as the entrance slit width used was $d_{\text{slit}} = 50 \mu\text{m}$ (i.e. bigger than the pixel width), the resolution can be estimated as

$$\text{bandpass} = d_{\text{slit}} \frac{d\lambda}{dx} = 0.13 \text{ nm}, \quad (4.2)$$

which is equivalent to $\sim 900 \mu\text{eV}$ at for wavelengths of $\sim 370 \text{ nm}$ (3.35 eV).

Although the spectrometer could be automatically calibrated, manual spectral calibration was performed using known mercury emission lines. The commercial software used to control the spectrometer (Andor SOLIS) then automatically calibrated the spectrometer to compensate for the wavelength dependence of the CCD efficiency, and also the effect of the blaze wavelength of the grating.

The confocal nature of the setup meant that only light from the area directly illuminated by the laser spot was focussed onto the spectrometer entrance slit. It was also possible, under white light illumination (using a battery driven LED) to view the magnified image of the sample surface on a separate camera. This enabled for sample aligning, and, in the case of the experiments in chapter 6, facilitated the locating of single nanocolumns that had had their positions registered in a scanning electron microscope (SEM).

4.4 Time Resolved μ -Photoluminescence Studies

In contrast to TIPL, time resolved photoluminescence (TRPL) is a technique with which we can ascertain information on the temporal nature of the emission. A schematic of a typical experimental setup is presented in figure 4.3. A $\text{Ti:Al}_2\text{O}_3$ laser with emission wavelength 800 nm producing 100 fs pulses at 80 MHz is split by a beam splitter such that a fraction of the beam is diverted to a fast photodiode which converts the laser pulses into electrical signals with a regular interval (80 MHz). The non-diverted portion of the beam is frequency tripled as explained above, and focussed on the sample. As before, the PL from the sample is directed to a spectrometer, but in place of the CCD, the signal is filtered with a slit such that a chosen wavelength falls upon a Photomultiplier tube (PMT) or Avalanche Photodiode (APD). The electrical signals (pulses) from both the fast photodiode, and the PMT are sent to the inputs of a commercial time correlated photon counting system (Becker & Hickl SPC-134) which measures the time between the two pulses. As this process occurs at 80 MHz a histogram can be created which shows the statistical properties of the arrival times of the photons. This enables the measurement of

emission decay from the sample, and is known as time correlated single photon counting (TCSPC).

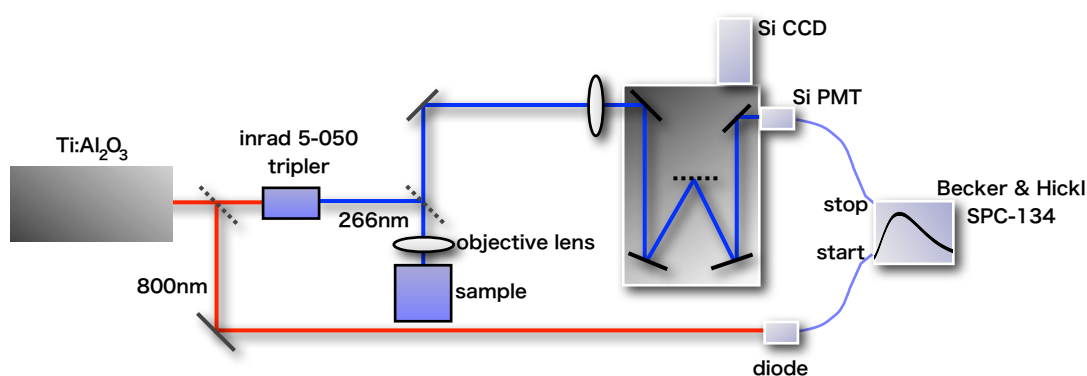


Figure 4.3: A schematic of a typical TRPL experimental setup.

As the TCSPC system measures the time interval between the two signals (one from the laser at the diode, and one from the photoluminescence impinging on the PMT) it is vital that the laser power is low enough that only one emission process occurs in the sample per laser pulse. If, for example, two decay processes were to occur, the second emission would be ignored as the TCSPC clock would stop on detection of the first. A histogram produced under these conditions would not give a true depiction of the underlying process, as only the fast decay processes would be measured, artificially reducing the measured lifetime by means of unfair sampling. In the case of the experiments carried out in this study, the TCSPC system was detecting on average 1000 counts per second, well below the rep rate of the laser (80 million pulses per second); clearly in the regime of fair sampling.

The PMT used in this study (Becker and Hickl PMH-100-0) was optimised for photon detection in the range of 300 – 600 nm, and has a quoted time resolution corresponding to its instrument response function (IRF) of 150 ps [121]. The fast photodiode used in the study (Becker and Hickl PHD-400-N) is optimised for photon detection at 800 nm (The Ti:Al₂O₃ emission wavelength) the rise time of the electrical response after photon detection is ~ 200 ps [122].

The absolute time resolution of the TRPL set-up will be a convolution of the IRFs of the constituent components, including the timing jitter due to electrical noise within the PC

card (quoted at ≤ 8 ps [123]) but in fact we have measured the absolute time resolution to be ~ 135 ps. This is probably due to the resolutions of our specific components being slightly better than quoted.

4.5 Electron Beam Lithography

Throughout the course of this investigation, it has been necessary to create patterns on samples in order that advanced experiments could be performed. For example, it was required that 500 nm apertures be opened in thin silver layers to enable single QD excitation experiments. Patterns have also been made in thin gold layers to facilitate experiments involving the excitation and luminescence mapping of nanocolumns. See figure 4.4 for optical microscope images of a selection of fabricated patterns. The process of creating the patterns will be explained in this section.

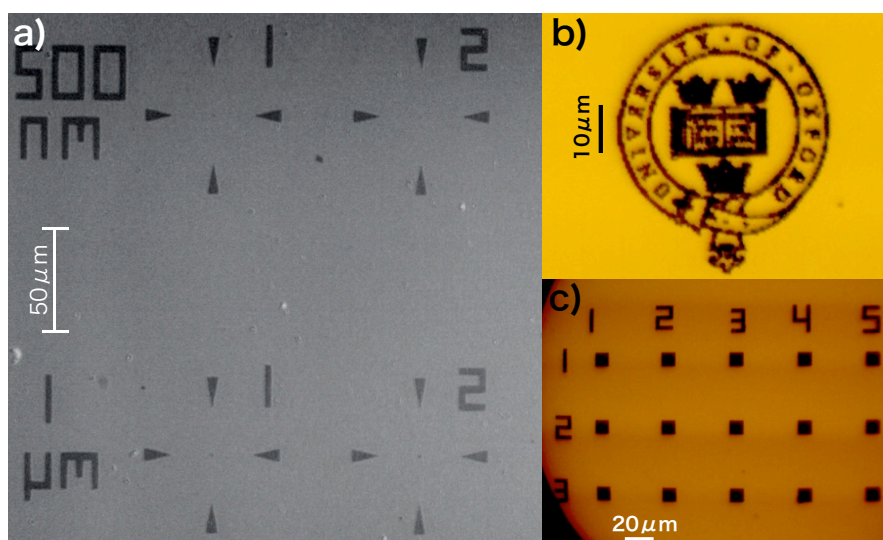


Figure 4.4: A selection of optical microscope images of samples made throughout this investigation. a) shows an aluminium mask layer for single QD excitation. The dark areas are apertures that have been opened up in the aluminium by using a wet etch of Decon 90:H₂O (1:10). b) shows the University of Oxford crest that has been made in a 65 nm layer of gold by using a commercial gold etch solution. c) shows a pattern made in the same sample as b), used for locating, and relocating, deposited GaN nanocolumns investigated in chapter 6.

To perform any successful process of writing, a contrast is required. When ink from a pen flows onto a piece of paper, the different absorption and reflection properties of the ink and paper provide the contrast that enable us to read what is on the page. In electron beam lithography,

the contrast is provided by the interaction between a chemical resist and an electron beam. Areas of the resist which have been exposed by the e-beam become chemically different from those areas which remain unexposed. There are many commercially available e-beam resists, but the most commonly used is poly(methyl-2-methylpropenoate) (PMMA) in anisole solvent. A typical electron beam lithography process consists of 4 steps:

1. Resist spinning
2. Exposure
3. Development
4. Pattern transfer

Each will be explained in full in the following sections, using the processes developed during the course of this study as a basis. After the processes have been explained, an overview of the JEOL JBX-5500ZC e-beam system will be given in section 4.5.1.

Resist Spinning

The resist is dropped via pipette (through a filter to ensure a clean resist) onto a metal-coated sample which is then spun at high speed (~ 4500 rpm). The centripetal force causes the resist to flow and distribute itself evenly across the surface of the sample. Both the angular velocity of the spinning sample, and the density of the resist solution will have an effect on the final thickness of the distributed resist. The sample is then heated for a few minutes (180°C) to cause the solvent to evaporate. Once this step is complete, the sample is ready for exposure. We have measured that spinning 950 PMMA 7% in Anisole at 4500 rpm results in an even layer of 800 nm thickness.

Exposure

The sample is loaded into the e-beam writing chamber and held at a vacuum of $\sim 10^{-5}$ mbar. The electron beam is focussed onto the sample surface by the electron optics system (EOS) and moved across the surface, exposing only the areas that it is incident upon. The exposure process involves the high energy electrons smashing into the PMMA polymers causing them to break

up. The exposed areas are thus more easily dissolved and can be selectively removed during the development process.

Development

Once exposure is complete the sample can be removed from the chamber and developed. Development consists of using a solvent to selectively remove the exposed areas of resist. Although there are many recipes for developing PMMA, It was found that a solution of methyl isobutyl ketone (MIBK) and isopropanol (IPA) 1:3 at room temperature would adequately develop the exposure. The development process takes ~ 60 s.

Pattern Transfer

The developed pattern is transferred into the metal via a wet etch solution. For etching aluminium, a solution consisting of Decon 90 (a strong alkali soap with pH in excess of 13) and water was used. For etching gold, a commercial gold etch was used. Examples of produced patterns can be found in figure 4.4.

4.5.1 JEOL JBX-5500ZC electron beam lithography system

In order to create the patterns shown in figure 4.4, a JEOL JBX-5500ZC series electron beam lithography system was utilised. The system boasts a maximum write resolution of 7 nm, but can be used in one of four different operating EOS modes, which determine the maximum field size, exposure time, and resolution available to the user. The system consists of, in its simplest form, an electron gun and focussing optics, a system to deflect the beam and to blank it when necessary, and a sample holder.

The electrons are emitted from a ZrO/W thermal field emission gun before being accelerated by 3 anodes and aligned by electromagnetic alignment coils and lenses. A stigmator coil then corrects the beam spot from an ellipse to a perfect circle with gaussian profile. The beam is then directed through the objective aperture, and is finally focussed on the sample surface by the objective lens. The beam blanker consists of an electric field perpendicular to the beam that

can be turned on to deflect the beam such that it doesn't pass through the objective aperture. Further deflector coils are used to scan the focussed beam over the sample surface, and are situated in the objective lens. The beam can be rastered across the sample using a 12 bit DAC (4000 × 4000 points) or positioned using an 18 bit position DAC (200000 × 200000 points). The maximum scan rate is 12 MHz. A schematic of the electron beam column can be found in figure 4.5

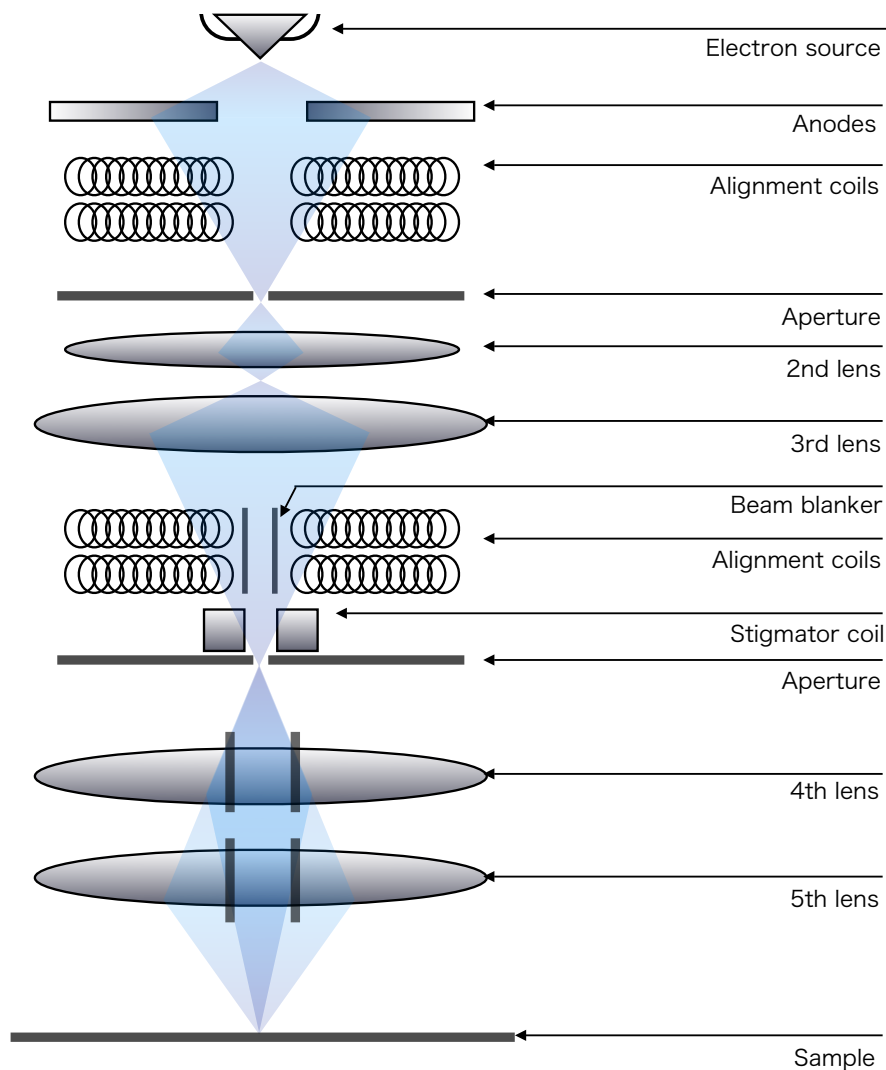


Figure 4.5: A schematic of the electron beam optics in the column of the JEOL JBX-5500ZC E-beam writer system.

The sample is held on a motorised stage in the focal plane of the electron beam. The

stage has a laser interferometer feedback system to accurately position the stage. The laser interferometer has a resolution of $\lambda/1024 = 0.62$ nm. The stage can be driven such that any desired area on the surface of the sample can be exposed with the beam.

The 4 EOS modes are defined by the accelerating voltage (25 kV or 50 kV) and whether or not a fifth lens is used to further focus the beam. An overview of the EOS modes can be found in table 4.1. The beam current can be set to exceed the value set by the EOS mode in order to

EOS mode	Acc. Voltage	Objective lens	Maximum field size	Beam current*	Step size
1	25 kV	4 th	2 mm ²	1 nA	10 nm
2	50 kV	4 th	1 mm ²	1 nA	5 nm
3	25 kV	5 th	200 μ m ²	100 pA	1 nm
4	50 kV	5 th	100 μ m ²	100 pA	0.5 nm

Table 4.1: An overview of the EOS modes for the JEOL JBX-5500ZC E-beam writer system.

reduce the write time required to expose the resist. However, beam widening will result, and a loss of resolution will ensue.

4.6 Cathodoluminescence

Cathodoluminescence spectroscopy has also been employed during this study. This involves using the beam of an SEM to directly excite (inject electrons) into the sample. Light radiated from the sample is collected and directed to a spectrometer for analysis. The system used was a commercial Gatan monoCL4 system [124] which was comprised of a commercial scanning electron microscope (Philips XL 30S FEG), with a liquid nitrogen cooled stage ($T = 90$ K) to which the sample is coupled. The electron excitation is provided directly by the beam, which is scanned across an area of interest on the sample surface. A mirror is positioned such that cathodoluminescence from the sample is collected and sent to a spectrometer with a PMT detector. The grating (1600 lmm⁻¹) is rotated and the spectrum recorded. As the accumulation of a full spectrum takes time, it is usual to use monochromatic imaging mode, in which the grating is aligned such that a fixed photon wavelength is measured, and the intensity then mapped as a function of position while the beam is raster scanned across the sample.

5

The Carrier Dynamics of $\text{In}_x\text{Ga}_{1-x}\text{N}$ Quantum Disks Embedded in GaN Nanocolumns

In this chapter the main experimental results from optical experiments on InGaN QDisk-containing GaN nanocolumns are presented, analysed and discussed. The work presented in this chapter has been published in references [125] and [92].

5.1 Initial investigation into GaN nanocolumns

Before analysing the samples containing QDisks, the emission spectrum of pure* GaN nanocolumns grown on Si(111) substrates is presented. The spectrum, which can be found in figure 5.1a), was acquired by Prof. Y. S. Park of Dongguk University using a commercial renishaw μ -PL system with a continuous wave He-Cd laser as the excitation source ($\lambda = 325$ nm). We see that there are 2 main emission peaks in the photoluminescence spectrum. These are well known emission peaks for GaN nanocolumns, the emission at ~ 3.47 eV is the combined emission from donor bound excitons (D^0X) at ~ 3.468 eV and free excitons (FX) at 3.476 eV, respectively [126]. The broad emission (with FWHM of approximately 30 meV) at 3.417 eV has been attributed to both extended structural defects located at the bottom of the nanocolumns [127] and the recombination of excitons bound to basal stacking faults (BSFs) [128]. The temperature dependence of the PL spectrum is shown in a magnified range, and a log intensity scale in figure 5.1b). It is clear that the FX emission energy becomes red shifted with increasing temperature, in line with the band gap red shift, whereas the D^0X emission is temperature independent. At temperatures

*Pure in the sense that no heterostructure, or no dopants have been purposefully added.

above ~ 60 K, the D^0X becomes delocalized, and contributes to the FX emission.

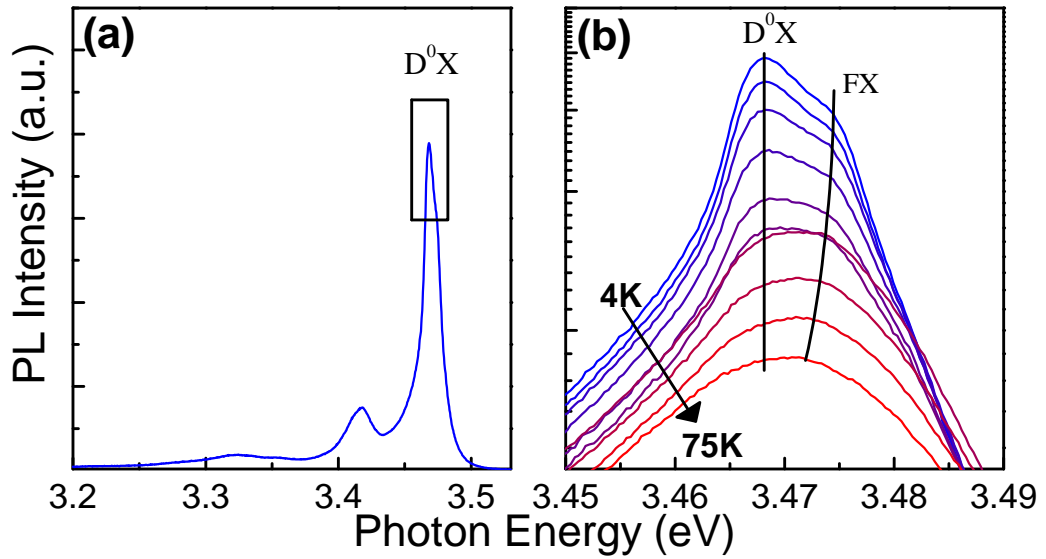


Figure 5.1: *a) Emission spectrum from a GaN nanocolumn at 4 K. b) Magnified region of the GaN excitonic emission, showing the evolution of the spectrum with increasing temperature (Spectra acquired by Prof. Y. S. Park of Dongguk University, Korea).*

5.2 Determination of the nanocolumn/QDisk luminescence spectrum

Next, the luminescence spectrum of nanocolumns containing single InGaN QDisks is compared to that from the pure GaN nanocolumns at 4 K (figure 5.2). In this case both samples were excited with a frequency tripled Ti:Al₂O₃ laser at 266 nm (120 fs pulses at 80 MHz) under the same experimental conditions using the setup as described in figure 4.2. Note that in this figure the luminescence intensity is presented on a log scale. As before, the UV laser spot size is about 1 μ m in diameter, such that in both cases about 8 nanocolumns are excited at any one time. Both samples contain the previously identified GaN and basal stacking fault emissions, but the sample with QDisks contains several additional emissions at energies lower than 3.4 eV. These emissions are highly focus dependent, and are attributed to carrier recombination within the QDisks.

To further elucidate the spatial origin of the emissions, cathodoluminescence at 90 K was employed using a MonoCL4. In figure 5.3 a) the cathodoluminescence (CL) emission spectrum

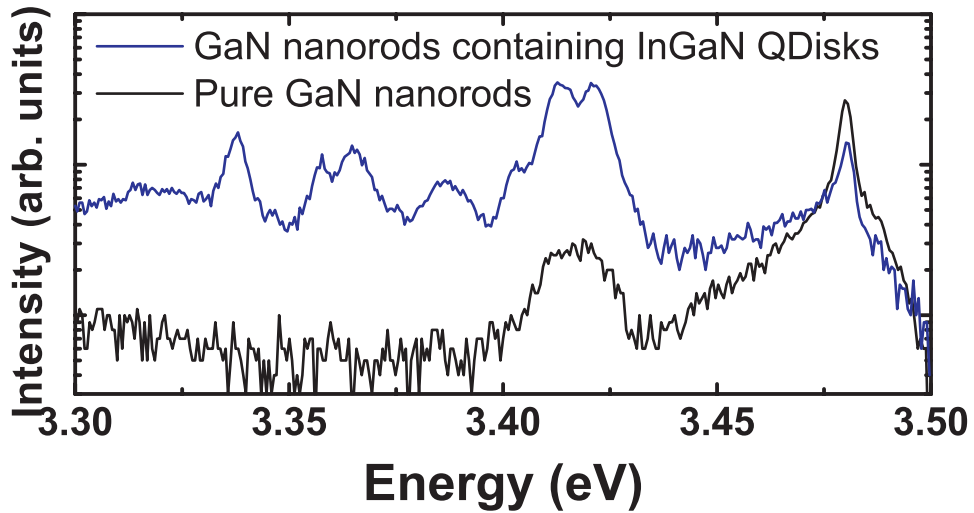


Figure 5.2: *Emission spectra from a selection of as-grown bare nanocolumns, and from nanocolumns containing single InGaN QDisks (both spectra taken at $T = 4$ K). The extra emission peaks from the QDisk sample are attributed to emission from the disks. About 8 nanocolumns lie under the laser spot.*

of an ensemble of nanocolumns is presented. The spectrum was acquired with an accelerating voltage of 10 kV. For comparison, optically obtained μ PL spectra recorded at 4.2 K and 90 K is also shown.

The 3 main emissions are present in both the CL and PL spectra. The elevated temperature CL and μ PL spectra show a much broader emission than the low temperature μ PL spectra. This is most likely due to the increased thermal energy of the carriers injected/excited into the structures. The CL spectrum was recorded by scanning the electron beam across, and integrating the luminescence from, a $5.5 \mu\text{m}^2$ area of the sample. The μ PL spectra were recorded from an area of $0.8 \mu\text{m}^2$ corresponding to the laser spot size. The 90 K μ PL spectra was recorded with a much increased excitation power, as the intensity of the emission is found to decrease for temperatures greater than 20 K, as shown in section 5.3.

The spatial origin of the luminescence was verified by scanning the electron beam across the sample surface on a clump of felled nanocolumns (felled by scratching the sample surface with a pair of tweezers). The results presented in figure 5.4 consist of 3 images showing the emission from the GaN (red), defect (blue) and QDisk (green) superimposed on a secondary electron SEM micrograph of the region under investigation. The accelerating voltage used during the

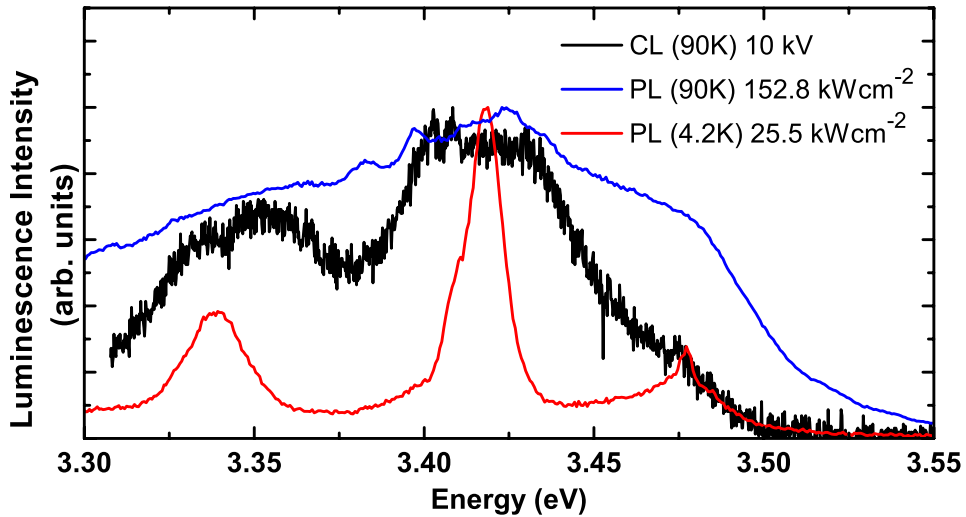


Figure 5.3: CL emission spectrum from an ensemble of QDisk containing nanocolumns recorded at 90 K with an accelerating voltage of 10 kV (black). μ PL spectra from the same sample recorded at 4.2 K (red) and 90 K (blue) are shown for comparison.

acquisition of these images was 5 kV in order to limit the penetration of the beam through several columns.

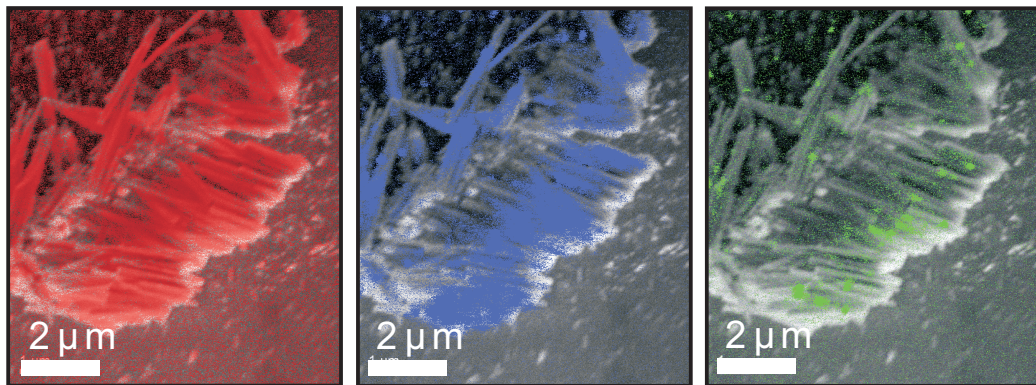


Figure 5.4: The emission from the GaN at 3.48 eV (red), the defect at at 3.41 eV (blue) and the QDisk at at 3.35 eV (green) superimposed on a SEM micrograph of the felled nanocolumns. In contrast to the GaN and defect emission, the QDisk emission is highly spatially localised, and originates near the tips of the columns.

It is immediately apparent that both the GaN and defect emissions originate from the body of the columns, whereas the InGaN QDisk emission is more spatially localised, and comes from the region near the tips of the columns. It is also observed that the bases of the columns appear to be optically inactive, perhaps due to damage incurred during the felling process.

5.3 μ -PL experiments on as-grown columns

In this section time integrated and time resolved μ -PL studies on the as-grown GaN nanocolumns are presented. The experiments were carried out as described in chapter 4.

5.3.1 Temperature dependent time-resolved μ -PL studies and the subsequent implications for the carrier distribution in the QDisk

Typical time-resolved and time-integrated emission spectra at temperatures from 4 K to 70 K (excitation power density = 4.1 kWcm^{-2}) from a single QDisk in a nanocolumn (isolated spectrally) are presented in figure 5.5. The emission decay at 4.2 K in the figure 5.5 b) inset is observed to have a monoexponential profile with a lifetime of $\sim 7 \text{ ns}$. As the temperature is increased above 20 K the decay becomes non-exponential and the characteristic decay time (measured as the time taken for the intensity to reach 1/2 of its peak value) is found to decrease with increasing temperature. This coincides with the decrease in emission intensity of the QDisk emission for temperatures greater than 20 K. This effect is most probably due to non-radiative decay routes opening up at higher temperatures [129]. There is no apparent blue shift (S-curve) of the emission with increasing temperature, indicating that there is not a large degree of carrier localisation due to indium content fluctuations in the disk. Indeed, low indium content QWs are usually observed to have lower indium content variation, and analysis of the peak indicates that the indium mole fraction, x , in this case is ~ 0.07 . It is possible, therefore, to put an upper limit on the energy state variations due to indium fluctuations as half of the peak FWHM: $\sim 4 \text{ meV}$ (in agreement with reference [60]). It is possible, however, that fluctuations in the well width across the diameter of the disk may result in a deeper confinement (of order 50 meV) that we couldn't hope to observe in the temperature range probed here.

As well as providing information on the uniformity of the indium content in the QDisk, this data provides an immediate insight on the nature of the carrier distribution in the QDisk. The low temperature emission occurs with a lifetime of 7 ns, which is comparable to the values of 1 – 10 ns published by Graham *et al.* [130] and Thrush *et al.* [131] for planar InGaN QWs of thickness 2.5 – 2.7 nm and mole fraction 0.05 – 0.12. In this regard, the QDisks act somewhat

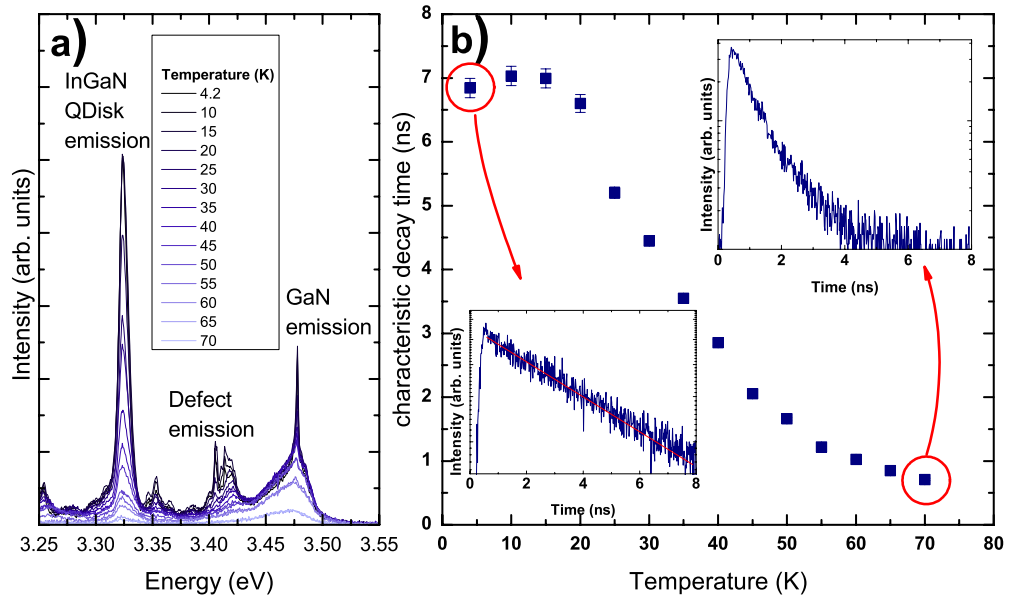


Figure 5.5: a) Time-integrated spectra from the as-grown nanocolumns at temperatures from 4 K to 70 K. b) Time-resolved studies showing a sudden decrease in lifetime for temperatures $T > 20$ K.

like planar QWs, as any further, lateral, separation of electron and hole wavefunctions induced by strain relaxation at the disk edge would most probably result in much longer lifetimes than those measured. Indeed, several studies have experimentally verified that in the InGaN/GaN system, allowing the carrier wavefunctions to be further separated along the c-axis by varying the QW thickness results in a drastic increase of the emission lifetime: Chichibu *et al.* [132] showed that for $\text{In}_{0.1}\text{Ga}_{0.9}\text{N}$ MQWs the emission lifetime increases by an order of magnitude as the well thickness is varied from 1.2 nm to 5 nm. Ryu *et al.* [133] similarly showed that $\text{In}_{0.15}\text{Ga}_{0.85}\text{N}$ MQWs exhibit an order of magnitude increase in lifetime as the QW thickness is increased from 1 nm to 4 nm. A more extreme case was demonstrated by Zhang *et al.* [134] during their investigations on $\text{In}_{0.19}\text{Ga}_{0.81}\text{N}$ MQWs, when they measured a lifetime increase from 5.8 ns to 454 ns as the QW thickness was increased from 2.2 nm to 4.4 nm. In these referenced studies on planar QWs, there is still the possibility that the carriers are indeed somewhat laterally separated by a few nanometers due to individual confinement of electrons and holes at spatially distinct indium fluctuations [135, 136]. The experimental evidence presented here, however, leads to the conclusion that the transition observed here is not due to the recombination of carriers which are

further laterally separated due to the inhomogeneous strain distribution in the disk; a separation which, in the most extreme case, would be ~ 70 nm.

5.3.2 Low temperature μ -photoluminescence studies: The quantum confined Stark effect

PL spectra from a different nanocolumn at 4 K as a function of excitation power density are presented in figure 5.6a. The QDisk emission is observed near 3.325 eV at an excitation power of 3.82 kWcm^{-2} . With increasing excitation power the QDisk emission shifts to higher energy, before saturating at ~ 3.340 eV. The emission energy is plotted as a function of excitation power density in the figure inset. Through a rough analysis of this shift, it is estimated that the indium mole fraction, x , is about 0.07 (see appendix B). The integrated peak intensities of the QDisk emission and GaN emission are presented as a function of excitation power in figure 5.6b. The excitonic emission from the GaN is measured to increase almost linearly whereas the QDisk emission initially increases as the square of the excitation power before becoming linear. The quadratic nature of this increase indicates that the recombination in the QDisk is mainly due to free carriers [137], though this effect could also be attributed to the field induced spatial separation of the electron and hole wavefunctions resulting in a situation where the excitons are weakly bound, and cross recombination between separate excitons occurs. After a small increase in excitation power, the growth of the QDisk peak also becomes linear, as expected for excitonic behaviour.

Time-resolved μ -PL data is presented in figure 5.7. The low excitation power decay in figure 5.7a is a mono-exponential decay from the QDisk, similar to that shown in figure 5.5. As the emission is broader at higher excitation power, it is possible to measure the time resolved characteristics of the emission as a function of energy. Two such decays are presented in figure 5.7b. The decay from the high energy side of the emission is nonexponential, and has an initial rapid decay of 390 ps, before dynamically reverting to a longer decay time. The lower energy side of the emission shows a slightly delayed 3.5 ns monoexponential decay.

TRPL traces at 12.73 kWcm^{-2} were measured at wavelength steps of 0.25 nm across the

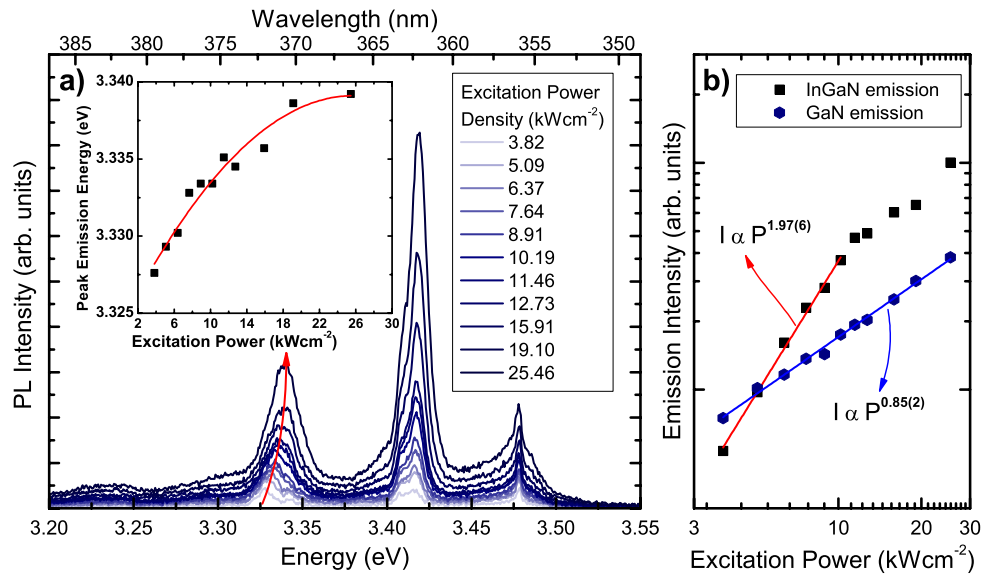


Figure 5.6: a) InGaN QDisk emission as a function of excitation power. The inset shows the QDisk emission peak position with increasing excitation. The fit to the curve is quadratic, and has been used to estimate the indium mole fraction. b) A log-log plot of QDisk and GaN emission intensities.

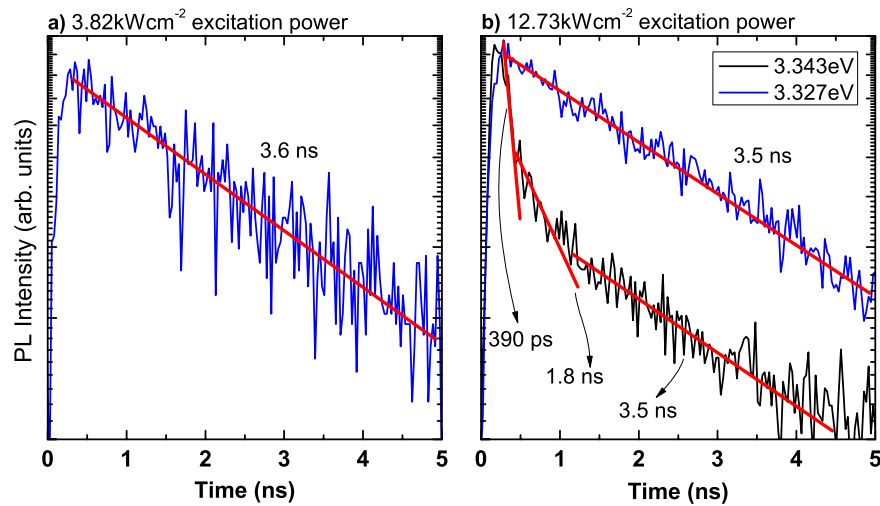


Figure 5.7: a) low excitation power (3.82 kWcm^{-2}), and b) high excitation power (12.73 kWcm^{-2}) emission spectra from the nanocolumn as a function of time. Under high excitation power the QDisk emission peak is observed to dynamically return to that which is observed in the low excitation power regime.

emission peak, and collated into a map showing the luminescence intensity as a function of both emission energy and time (see figure 5.8). It is clear that at high excitation power, the emission starts at higher energy, before dynamically shifting back to that what is observed in the low excitation power regime. This shift is shown in context of the whole emission spectrum in figure 5.9, which was measured from a different area of the sample.

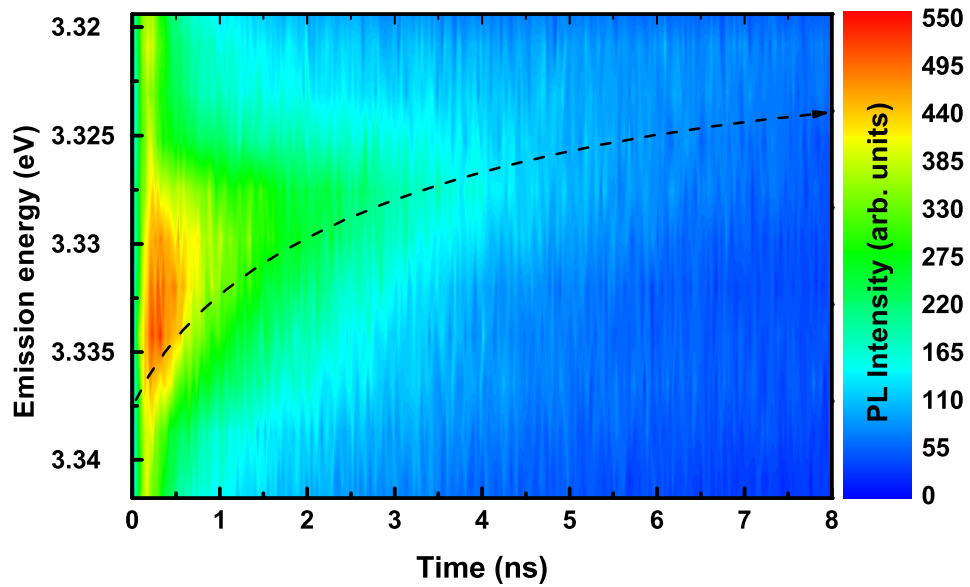


Figure 5.8: *The luminescence intensity as a function of emission energy and time at an excitation power of 12.73kWcm^{-2} . The emission energy is observed to shift during the process of the decay.*

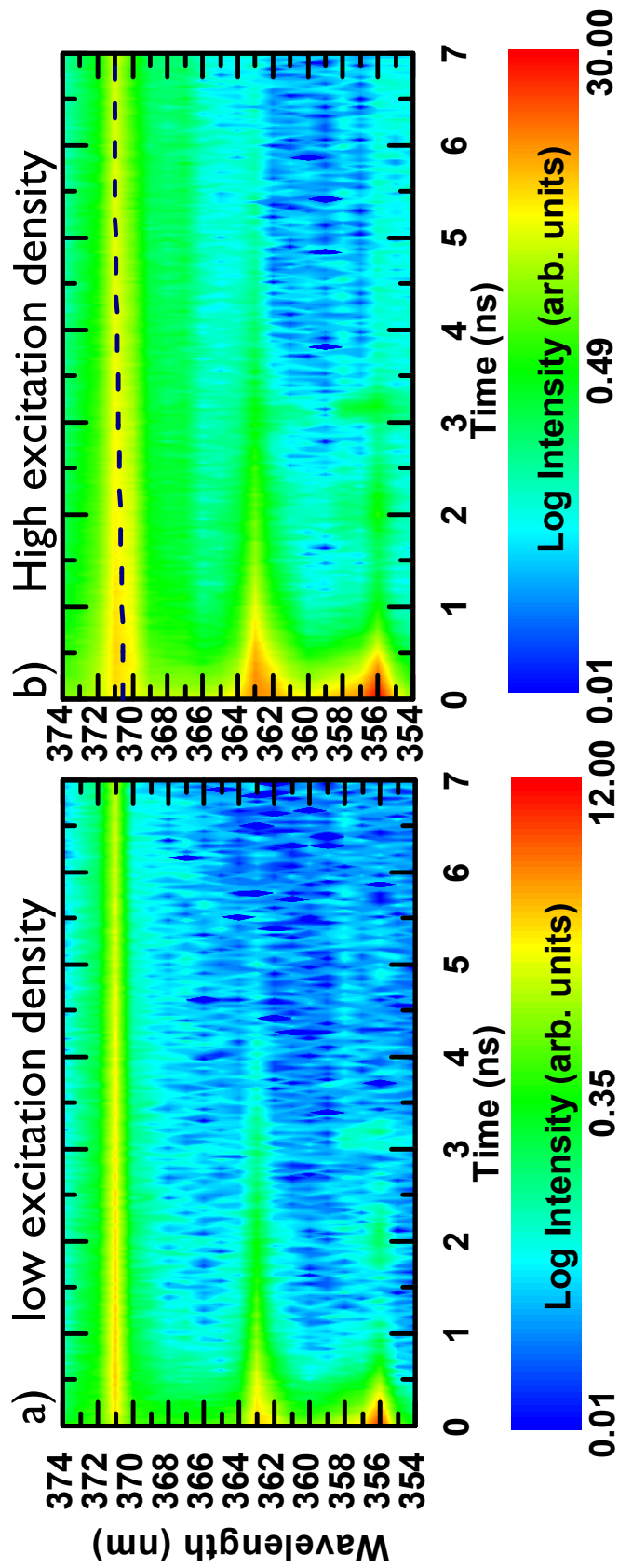


Figure 5.9: a) Time evolution, at an excitation power density of 6.37 kWcm^{-2} , of the PL spectrum from a QDisk sample. b) The temporal progression of the same emission spectrum at 19.1 kWcm^{-2} (In both of these cases, the constituent TRPL data was recorded in wavelength steps of 1 nm across the entire emission spectrum).

The blue shift of a quantum well emission with increasing excitation has been observed before, and can be attributed to either fluctuations in the indium content in the QDisk [138], or to charge screening and the quantum confined Stark effect [139, 140, 141]. The multi-exponential decay at high excitation power, however, is a characteristic feature of a screening of the internal field [142]. In this case, we also note that the measured effect occurs at the same excitation power density range measured by Koukstis *et al.* [138], when they observed the screening of an internal field in an $\text{In}_{0.15}\text{Ga}_{0.85}\text{N}$ quantum well (at excitation power densities almost two orders of magnitude lower than would be expected for the filling of localized states). An additional study by Lai *et al.* [69] corroborates that the shift due to screening occurs at lower excitation densities than that of filling band states. Furthermore, as explained above, no measurable blue-shift is observed in QDisk emission with increasing temperature (see figure 5.5) such that the *maximum* blue shift expected from the filling of these states in this case is 4 meV, $3\times$ smaller than that measured. These observations lead to the conclusion that the effect measured here is mainly due a charge screening process, and that indium content fluctuations play only a minor role, if at all, in the emission shift measured in this case. Local photo-induced heating of the sample is ruled out as a mechanism for the peak energy shift, as the GaN emission is observed at a constant energy for all excitation power densities.

It has been suggested that one way to discriminate between a band state filling process and the QCSE is to look at the width of the emission at different powers. The theory is that if the blue shift is due to the filling of states, then the emission will broaden with increasing excitation density.[†] On the other hand, if the blue shift is due to a screening of the QCSE, then one would expect a *narrowing* of the emission with increasing power. This analysis cannot be used in this case as the spectra acquired here have been integrated for 1 second each. During this integration period, the laser will cycle 80 million times, and the QDisk will be re-excited and the same number of decays will occur. Therefore the broadening of the peak that we observe at high excitation densities could quite conceivably be due to an integration of several narrower

[†]FWHM broadening has been measured, however, by Hou and Tu [143] when they observed field screening in InAsP/InP QWs. It was argued that the broadening is due to interactions between the hot photo-excited carriers, which cannot be ruled out in this case.

peaks over the course of the decay/accumulation.

Indeed, the discrepancy can be alleviated by closer inspection of the data in figure 5.8. It is possible to probe the time evolution of a single decay process in the emission by recreating the spectrum at various times during the decay (see figure 5.10). The expected QCSE broadening is observed with increasing time as the screening effect is reduced and the peak is shifted by the increasingly unscreened internal field. In fact, under this analysis, one would expect the peak to become *narrower* during the decay if the dominant mechanism was the filling (or indeed un-filling) of states. The broadening of the peak is clear evidence of the QCSE process.

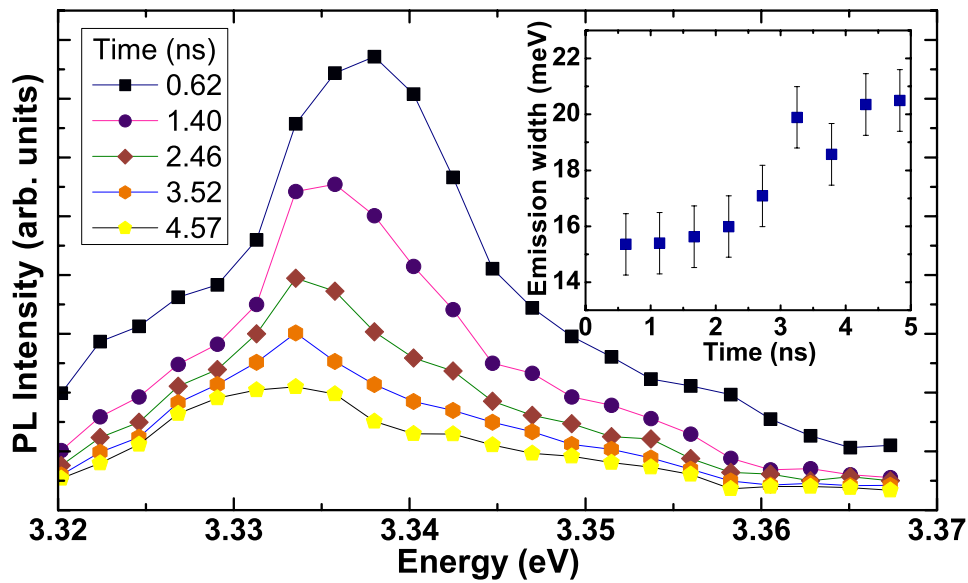


Figure 5.10: The decay spectrum at different times (recreated from the data in figure 5.8). The emission peak broadens as it shifts to lower energy due to the QCSE from the internal field.

The field screening process is explained as follows, and summarised in figure 5.15 at the end of the chapter. At low excitation powers the carriers in the well are acted on by the internal field such that electrons and holes find themselves at opposite sides of the well. This quantum confined Stark effect results in a lifetime of 3.5 ns, and a lower emission energy. At high excitation powers, however, the large number of carriers at the sides of the well generate their own field to screen the centre of the well from the effects of the internal field. The resulting increased wavefunction overlap leads to a rapid decay (in this case 390 ps) which is an order of magnitude faster than that measured at low excitation powers. This fast emission is at higher energy due

to the reduced effect of the internal electric field. As carriers recombine in the disk, the size of the screening field decreases, and the wavefunction overlap reduces, leading to a dynamic change in both the decay lifetime and the decay energy.

5.3.3 Further evidence for the QCSE in $\text{In}_x\text{Ga}_{1-x}\text{N}$ QDisks

In addition to the data presented above, a study was carried out on several columns containing single QDisks. The low excitation power emission was recorded and the lifetime measured by $\mu\text{-PL}$. The data is presented in figures 5.11(a) and (b). It was found that QDisks emitting at lower energy tend to have longer lifetimes. This can be simply explained by the fact that lower energy emitting QDisks are likely to be slightly thicker, (thus having increased wavefunction separation) or have a larger indium mole fraction and thus be under more strain. This increased strain would lead to a larger internal electric field which will reduce carrier wavefunction overlap and enhance the emission lifetime.

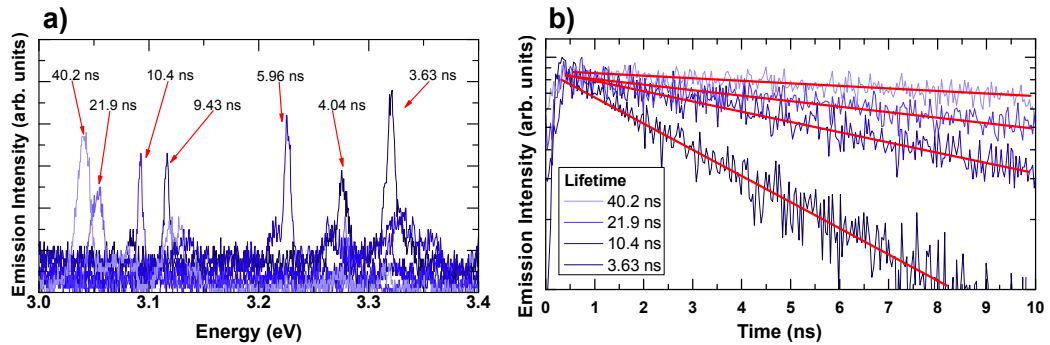


Figure 5.11: a) A selection of spectra showing QDisk emissions, labelled with their low power excitation lifetimes. b) A selection of decay traces, showing the monoexponential decay nature of the emissions.

5.4 Defect emission

In this section the emission band at 3.40 – 3.43 eV is analysed. This has been rigorously characterised by Calleja *et al.* [128] and has been shown to originate from structural defects in the columns. The analysis here is presented for completeness and as a comparison to the data

presented above, and that in the literature.

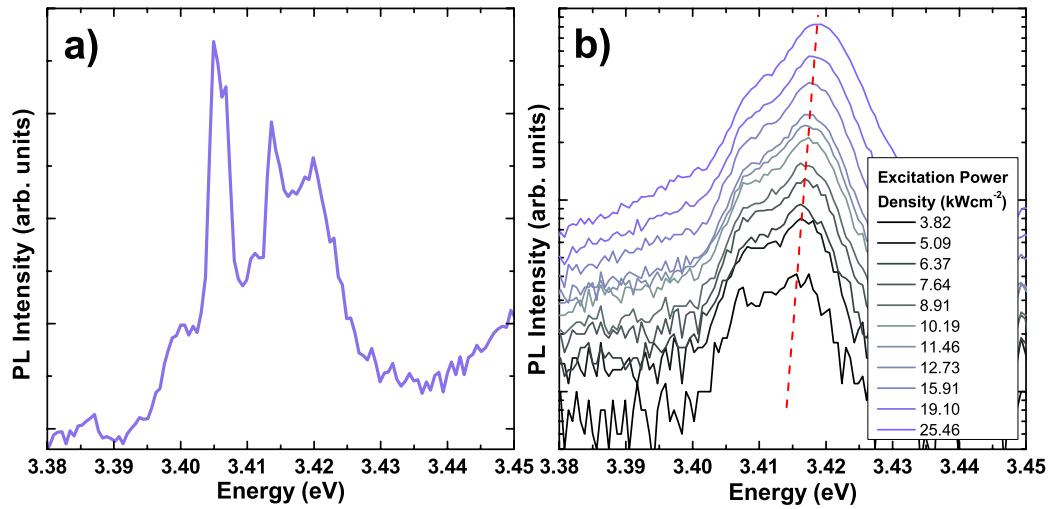


Figure 5.12: a) The emission in the region of 3.4 eV to 3.43 eV measured at 4.2 K and with an excitation power of 4.1 kWcm^{-2} . A structure in the emission is clearly visible. b) Log plot of the emission intensity with excitation power from another part of the same sample where the structure is less apparent. A blue shift of the emission with increasing excitation is observed.

Upon close inspection of the defect emission in figure 5.5, which is now magnified in figure 5.12a, it is observed that the emission consists of multiple narrow peaks. The minimum width measured from these peaks is 2 meV. The relative visibility and peak position vary across the sample, and indeed from sample to sample. The observation of this structure is in agreement with the measurements of Fischer *et al.* [144] who, during their investigation into wurtzite GaN films, observed the emergence of a structure in the emission at 3.41 eV. The structure appears to be more complex in this case however, owing possibly to the measurement technique (μ PL as opposed to PL) or perhaps to varying degrees of strain relaxation in neighbouring columns of differing diameter.

A log plot of defect emission spectra with increasing excitation power (The same spectra first presented in figure 5.6(a)) can be found in figure 5.12(b). In this case the structure of the emission is not as apparent, and a small shift to higher energy ($\sim 3 \text{ meV}$) is observed as the excitation power is increased by an order of magnitude from 3.82 to 25.46 kWcm^{-2} . Calle *et al.* [145] measured a similar ($\sim 5 \text{ meV}$) blue shift for a factor 15 increase in excitation power and attributed it to the saturation of donor-acceptor pairs (DAP). It could be that some of the

structure in the broad emission is due to structural defects in the column body, and part due to DAP recombination.

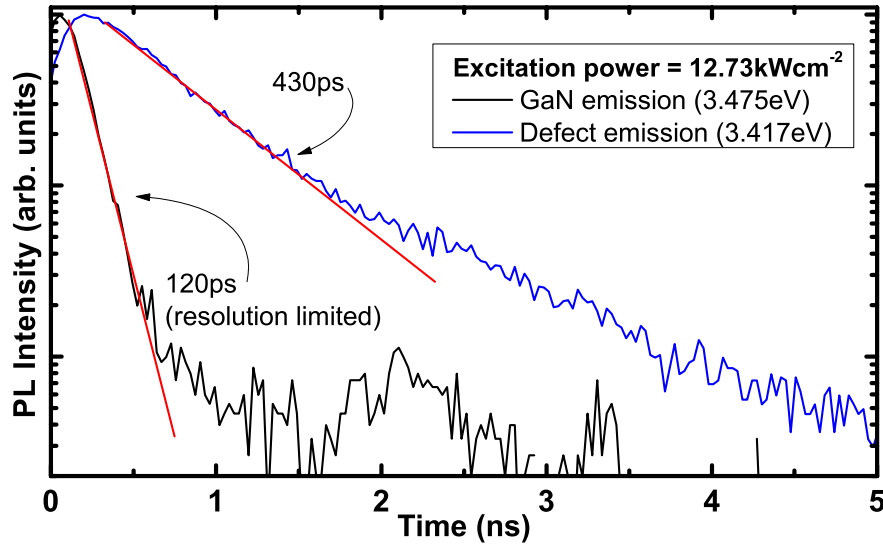


Figure 5.13: Normalised time-resolved decays from the GaN emission at 3.475 eV and the defect emission at 3.417 eV measured with an excitation power of 12.73 kWcm^{-2} .

A time-resolved decay trace from the defect emission (and also the GaN emission, for comparison) at an excitation power of 12.73 kWcm^{-2} is presented in figure 5.13. The decay is non exponential, though has a characteristic decay time of 450 ps, in agreement with the study of Calleja *et al.* [128]. Finally (in figure 5.14) a spectrally and time-resolved map of the emission is presented, akin to that of the QDisk emission presented in figure 5.8. Within the resolution limit of the setup, the defect emission is observed at constant energy during the decay, in contrast to the shifting decay energy of the QDisk emission.

5.5 Chapter Summary

μPL investigations have been carried out on GaN nanocolumns containing low indium content $\text{In}_x\text{Ga}_{1-x}\text{N}$ ($x \sim 0.07$) QDisks. The radiative lifetime of the emission at 4 K indicates that there is no lateral charge separation in the QDisks on length scales comparable to the disk radius. It still remains a possibility that carriers are somewhat laterally separated on length scales of a few nm due to localisation at individual localisation centres within the QDisk (this is the same

as in 2 dimensional quantum wells). The QCSE is observed through the lifetimes of the QDisk emission, and that lower energy emitting disks have longer decay times. The blue shift with increasing excitation density is attributed to a dynamic process of field screening (rather than to the filling of band states) due to the following observations:

1. The excitation density at which the shift occurs is the same as that measured by Kuokstis *et al.* [138].
2. The dynamic shift of the time resolved PL spectrum leads to a peak broadening.
3. There is no observable blue shift under increased temperature, thus limiting the possibility of the existence of localised states.
4. The nonexponential decay at high excitation powers is characteristic of the QCSE [142].

A summary of the measured shift and broadening process can be found along with illustrations of the assumed carrier distributions in figure 5.15.

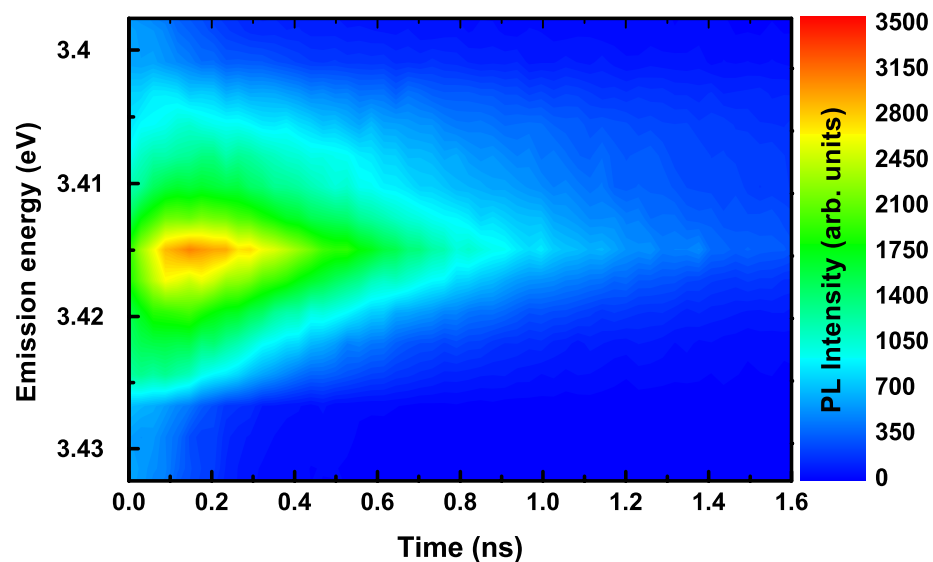


Figure 5.14: *The luminescence intensity as a function of emission energy and time at an excitation power of 12.73kWcm^{-2} . In contrast to the InGaN QDisk emission, the defect emission does not dynamically shift with time.*

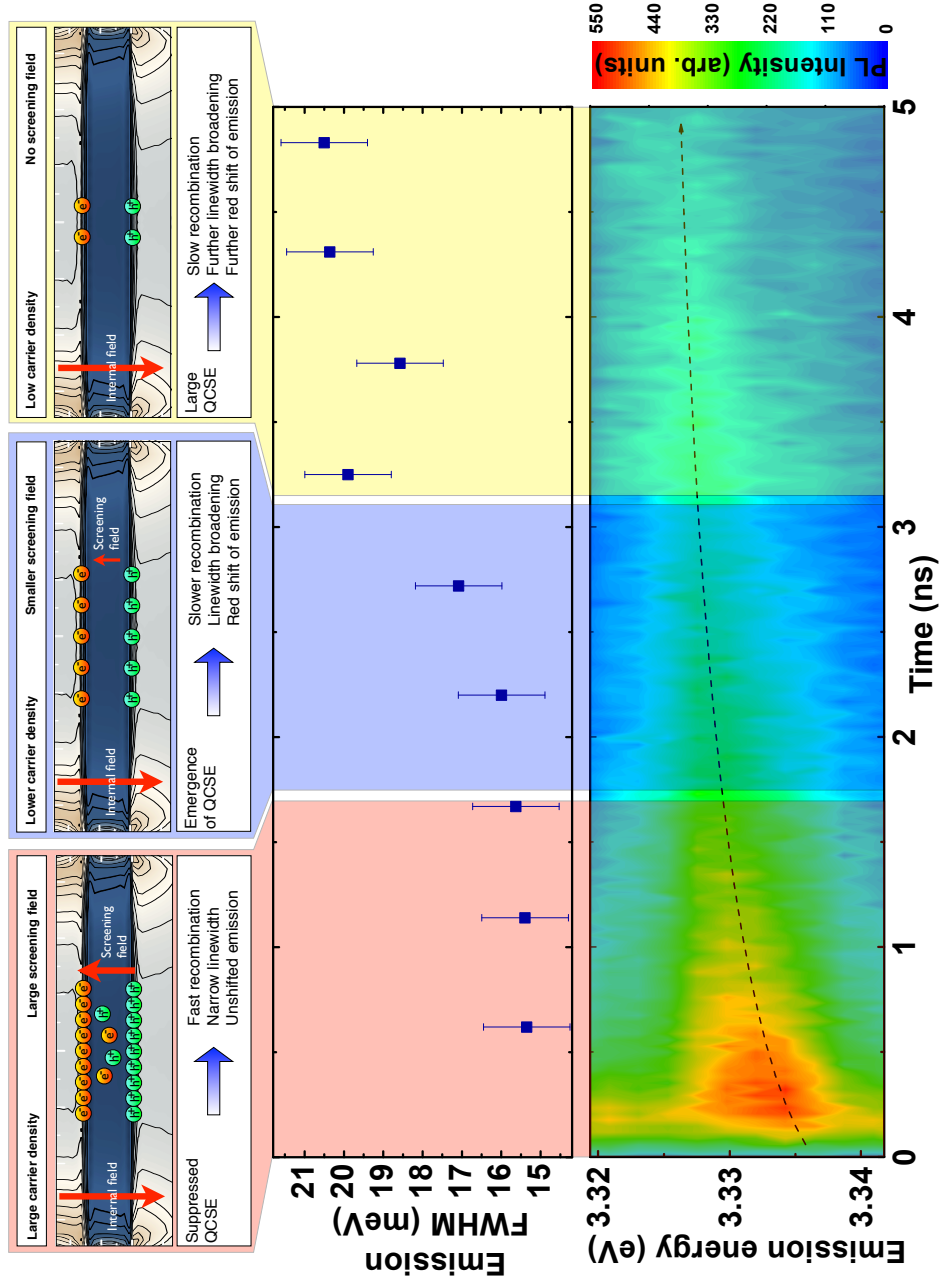


Figure 5.15: Summary of the main data in this chapter, along with accompanying explanation of the emergence of the QCSE during the recombination process.

6

Optical Studies on a Single GaN Nanocolumn Containing a Single $\text{In}_x\text{Ga}_{1-x}\text{N}$ Quantum Disk

In this chapter the experimental studies presented in the previous chapter are continued, but this time investigations into the optical properties of a single, isolated, nanocolumn are presented. The work here has been published in reference [146].

6.1 Isolating and locating a single nanocolumn

As the laser beam spot size is $\sim 1 \mu\text{m}$, excitation of an as-grown sample involves the simultaneous excitation of ~ 8 nanocolumns. To facilitate the optical excitation of a single column, many columns were mechanically removed from their growth substrate, suspended in methanol, and then dispersed over a thin grid of gold (65 nm) on quartz. The gold had been thermally evaporated and its thickness estimated during the evaporation process by monitoring a calibrated crystal. Before being covered with nanocolumns, the gold layer was patterned using electron beam lithography as outlined in section 4.5. An example of a grid made in this way can be found in figure 6.1. In the same figure, a scanning electron micrograph showing an area of the grid once it had been covered with nanocolumns, and a micrograph showing the isolated column that is investigated, are presented.

The SEM was used to identify a single column and acquire a grid reference for its position. This reference point was then used to relocate individual nanocolumns for optical probing using the experimental techniques described in chapter 4.

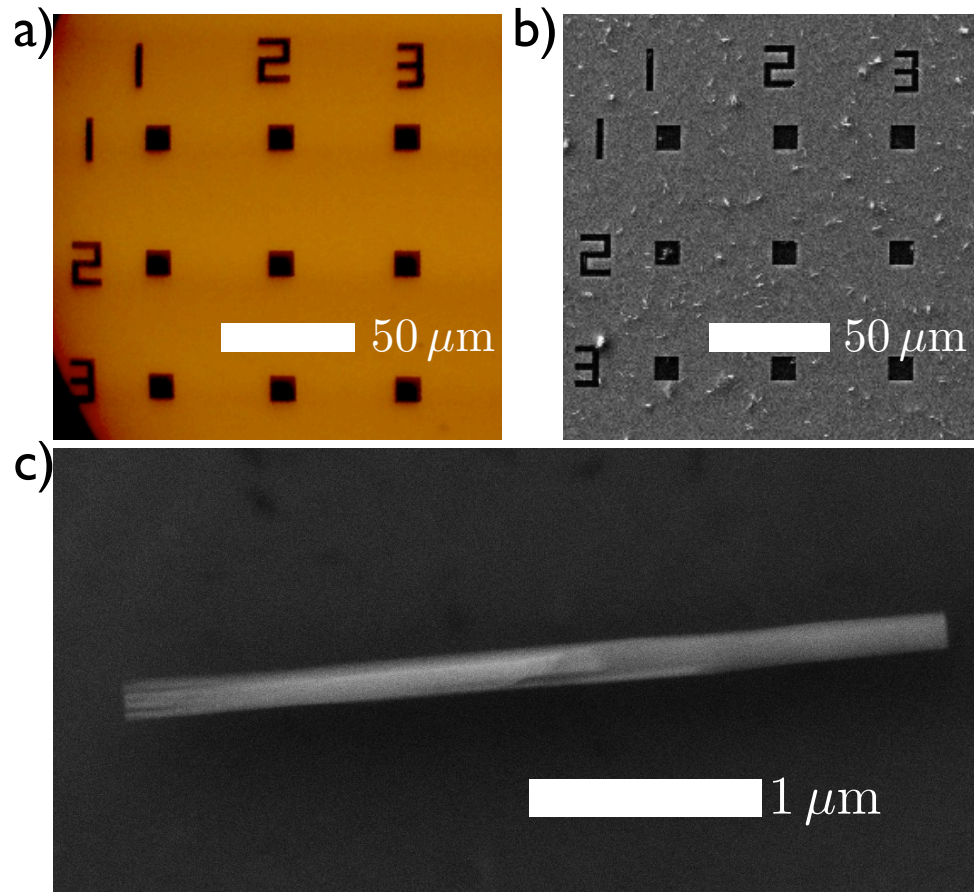


Figure 6.1: a) Optical microscope image of a gold on quartz grid. b) The same grid when viewed in a SEM after being covered in nanocolumns. c) The single nanocolumn investigated in this chapter.

It was found that after the evaporation of the methanol, the columns remained well adhered to the surface of the grid, even after several cooling and warming cycles. This adhesion is presumably caused by Van der Waals forces, as has been previously postulated for carbon nanotubes [147].

As the column under investigation lies on the gold surface, care must be taken to ensure that no plasmonic effects will affect the measurements. In short, it is believed that the gold will have no effect on the optical properties in this case, as is discussed briefly in section 6.2.

6.2 (The lack of) plasmon effects

Surface plasmons are resonances due to oscillations in the free electron density on the surface of a solid. The coupling of semiconductor emission to surface plasmons is used as one way to combat the unwanted internal reflection in III-Nitride based materials: The light couples to the plasmon mode, where it is more easily emitted into the surrounding air. It is not expected that coupling to surface plasmons in the gold will occur in this case because the Au-GaN surface* plasmon frequency (ω_{sp}) is ~ 2.4 eV [149]; well away from the emission energies of the sample under investigation. Indeed, the coupling between InGaN QWs and gold has been shown to be significantly suppressed when compared to the coupling to, for example, plasmons in silver [150, 151].

Furthermore, the gold layer was not artificially patterned on the nanometer scale, such that any emission rate enhancement due to plasmon coupling would be further limited [149]. Indeed, no substantial emission lifetime difference between columns scattered on the gold, and columns attached to their growth substrate, is observed, indicating a lack of plasmon coupling in this case [152].

6.3 Initial Optical studies on the single column

The grid was placed in a continuous flow He cryostat and cooled to 4 K. The laser was focused on the grid reference of the previously identified single column and the excitation position was scanned across the column and surrounding area using a piezo stage (PI nanocube P-611.3SF). The collected PL was directed to the spectrometer for analysis. Using this surface scanning technique it was possible to measure spatially resolved PL spectra, and hence map the PL from the column along the length of the column with a spatial resolution of $\sim 1 \mu\text{m}$ (the laser spot size).

Spectra acquired in this way are presented in figure 6.2. The maps in a), b) and c) show

*For the gold-air interface, the plasmon resonance is found to be at ~ 2.25 eV [148]. This energy is also far from the spectral range that we are interested in (3.2 eV-3.5 eV)

the luminescence intensity (measured from a single pixel \implies an integrated spectral range of ~ 0.07 nm at each respective energy) of the emission peaks at 3.46 eV (GaN), 3.41 eV (defect) and 3.34 eV (QDisk), acquired over a $4.2 \mu\text{m} \times 2.6 \mu\text{m}$ area using $0.2 \mu\text{m}$ steps of the piezo. The data was collected under an excitation power density of 62 kWcm^{-2} . This comparatively large power was necessary as, due to vibrations and drift in the continuous flow cryostat, the maps had to be acquired with celerity. The high excitation power ensured that the photoluminescence signal was high enough that 0.1 s accumulation times could be used per pixel in the map.

The column can be clearly identified in the maps, and a white line has been added as a guide to the eye. The GaN and defect emission originate along the length of the column whereas the QDisk emission is observed at only one end, as expected. The spectra presented in d), e) and f) are from the areas to which the arrows point in the SEM images in the respective figure insets.

It is apparent from the map in a) and the spectra in d), e) and f) that the GaN emission becomes somewhat suppressed towards the end of the column containing the QDisk. In tandem with this effect, the defect emission appears to increase in intensity, indicating a larger defect density towards the tip of the column. This is in agreement with the spectra in figure 5.2, which show an enhanced defect emission from the QDisk-containing nanocolumns, and indeed, may add further weight to the classification of this emission as defect related, as the number of defects might be expected to increase with the lattice mismatch induced strain in the vicinity of the QDisk. The monochromatic CL images of figure 5.4 also show this effect.

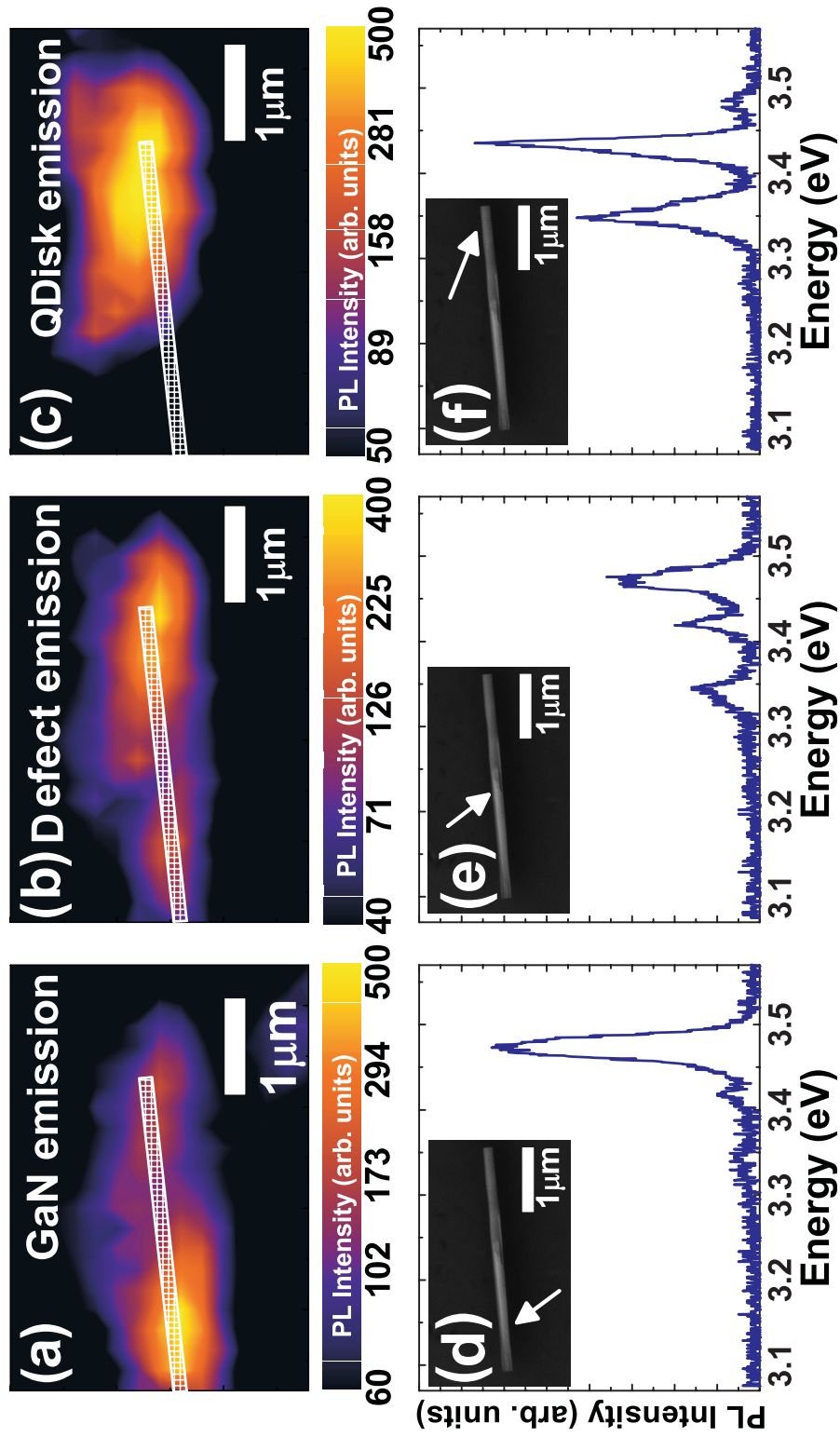


Figure 6.2: a) b) c) Spatial PL maps from the column under investigation at emission energies of 3.46 eV (GaN), 3.41 eV (defect) and 3.33 eV, respectively. d) e) f) Emission spectra at various positions along the column length as shown in the figure insets.

As in chapter 5, TRPL data was measured across the spectrum (in this case in 0.5 nm steps across the main peaks of the emission spectrum). The decays measured at the peak intensities of the 3 main emissions can be found in figure 6.3. These decay histograms were measured under an excitation power density of 19 kWcm^{-2} . The GaN emission has a resolution limited lifetime of 130 ps (compare to values in the literature of 170 ps [128] and 92 ps [126] for pure GaN nanocolumns), whereas the defect emission lifetime is 370 ps and the QDisk lifetime is $\sim 2 \text{ ns}$. A further point of interest in this figure is that the decay of both the defect and the QDisk are slightly delayed in time due to a rise time comparable to the decay time of the GaN. This information, along with the data presented in figure 6.2 can be explained as follows: Upon above band gap illumination ($\hbar\omega = 4.66 \text{ eV}$, $E_{g\text{GaN}} = 3.5 \text{ eV}$), carriers are excited in, and are free to move around, the GaN column (and form excitons). Carriers at the end of the column nearest to the InGaN QDisk are likely to become captured in the well or defects, and, in doing so will recombine at the well/defect energy, respectively. This process reduces the number of carriers available to recombine in the GaN, resulting in a suppressed GaN emission from the region of the column in the vicinity of the QDisk.

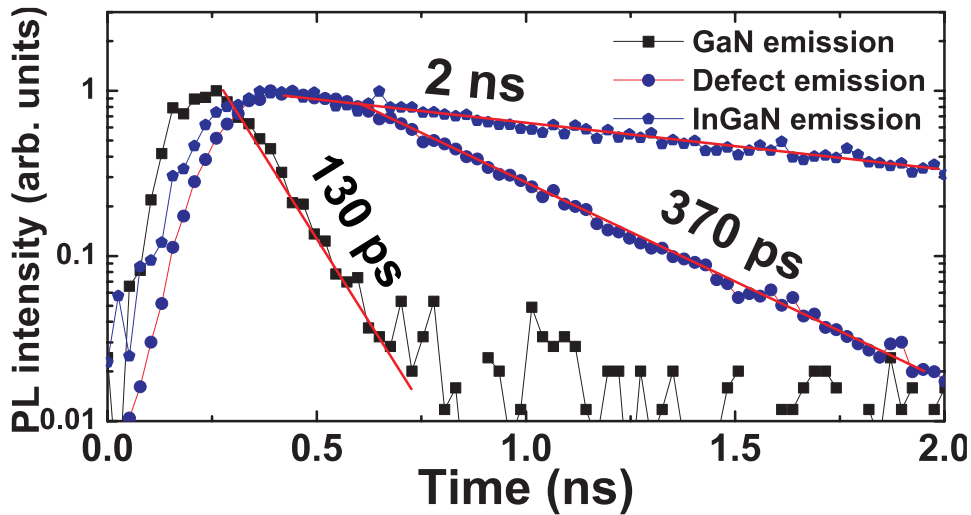


Figure 6.3: Photoluminescence decay traces measured from the 3 main emissions from the nanocolumn (at peak intensity).

It is possible to plot spatially and time resolved emission maps of *all* of the light emitted from the nanocolumn by evaluating, and summing, the temporally and spatially variant emission

intensity of the three luminescence peaks. In order to perform this analysis the TRPL traces were normalised such that their time integrated intensities were set to 1, hereafter labeled $T_E(t)$, where the subscript E labels the emission energy at which the decay was measured. These time dependent functions were then multiplied by their spatially dependent functions $S_E(x, y)$ (similar to those in figure 6.2) such that the total luminescence from the nanocolumn/QDisk as a function of position and time could be calculated by

$$I(x, y, t) = \sum_E S_E(x, y) \times T_E(t), \quad (6.1)$$

where the sum is performed over *all* of the energies at which the decay curves were measured.

It is assumed that the lifetime of each emission is not spatially dependent (this is reasonable for analysis of this experimental data as any change in the GaN emission lifetime would anyway not be resolvable temporally, and the defect/QDisk emissions are highly localised spatially). The maps can then be evaluated as direct indications of the carrier density in the column in slices of time. Here the total of all light is being measured so it is of no concern that, for example, that lifetime of the GaN decay from the region of the column near to the QDisk will be decreased due to non radiative transfer of carrier density from the column to the QDisk. In fact, the luminescence due to the recombination of these carriers will be accounted for by the increasing weighting factor of the Qdisk/defect luminescence at this spatial location. In the calculation it is assumed that there are no other non-radiative states. The calculated maps indicate the density of carriers that directly contribute to the luminescence output of the column/Qdisk system.

The resulting maps, calculated using equation 6.1 can be found in figure 6.4, which gives a depiction of the carrier density in the column at slices of time. The maps have been rotated 90° counter clockwise with respect to the maps shown in figure 6.2. As before, an SEM micrograph of the column is presented for clarity. On the right hand side of the figure, the total carrier density as a function of time, at 3 positions along the column, is plotted. The decay is non exponential in the 3 regions due to the fact these decays are of the total carrier density, which

are linear combinations of the decays from individual luminescence peaks.

The dynamic shift in the spatial carrier distribution function is apparent. As expected, the distribution of carriers at $t = 0.13$ ns is fairly homogeneous along the length of the column, owing to the fact that at this early time very few carriers have had the chance to recombine and leave the system. As time progresses, carriers become trapped in the QDisk and defect states and we begin to see a corresponding larger carrier density in the vicinity of the QDisk. At time $t = 2$ ns the recombination of GaN related excitons has been occurring for several lifetimes, and less than 7% of the initial carriers remain in the system; almost entirely distributed in the QDisk.

6.4 Chapter Summary

In conclusion, both spatially and temporally resolved photoluminescence spectra from a single GaN nanocolumn containing a single InGaN QDisk have been measured. The spatially resolved PL shows a reduced luminescence intensity of GaN related emission in the vicinity of the QDisk. This is most likely due to carriers being transferred into the QDisk, or into a higher density of defect states in this region. The luminescence has been collated into maps in slices of time that show the evolution of the carrier distribution in the column, direct evidence that the distribution varies considerably with time under pulsed operation.

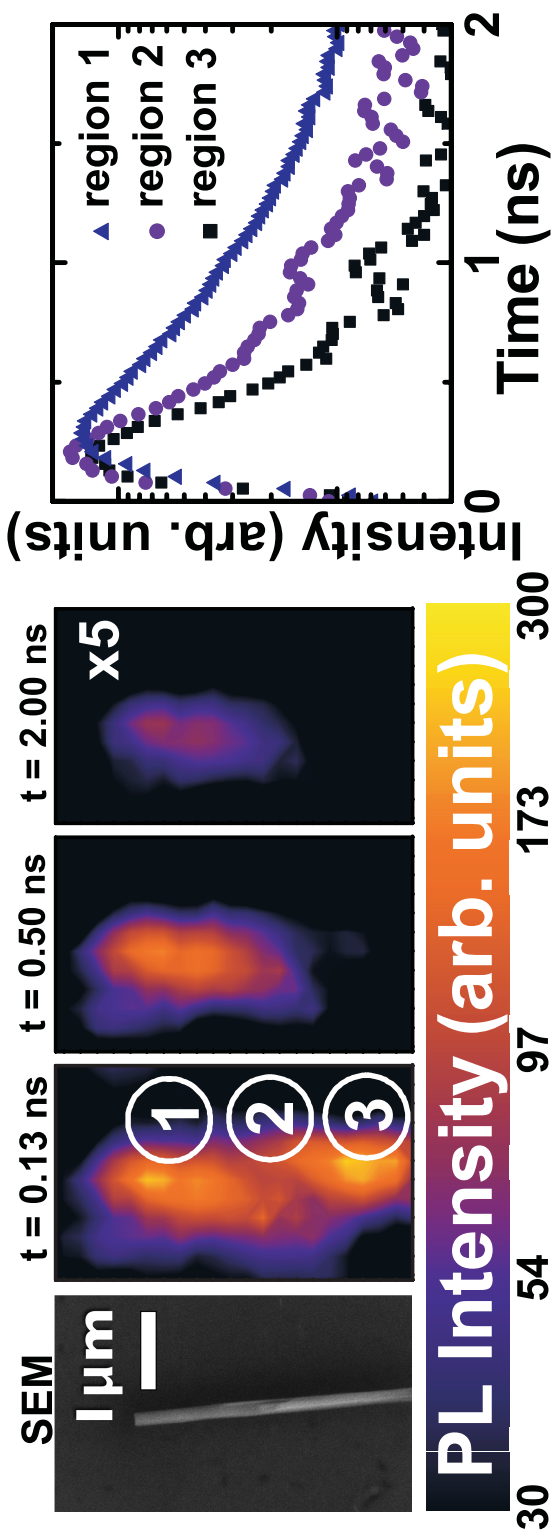


Figure 6.4: Spatially resolved PL intensity at slices in time after the laser excitation pulse. At low values of t the distribution is fairly homogeneous, whereas at large values of t almost all remaining carriers are in the QDisk. The plot on the right shows the total PL intensity as a function of time from the regions labelled 1, 2 and 3.

7

Self Assembled III-Nitride Nanotubes and Nanopyramids

In this chapter some initial experimental results are presented from novel structures that are based on GaN nanocolumns; namely self assembled GaN nanotubes and nanopyramids. Although optical studies on GaN based nanotubes and pyramids have been reported in the literature, the samples studied here have been grown using a self assembly process. The chapter is split into two sections; the first documenting the studies on GaN nanotubes, and the second on GaN nanopyramids. The work is currently being written up for publication.

7.1 The Optical Properties of Self-Assembled Crystalline GaN Nanotubes

The discovery of carbon nanotubes in 1991 [153], induced fervent research efforts towards the synthesis and understanding of physical properties of nanoscale tubular structures composed from a variety of materials [154, 155, 156, 157, 158, 159]. Amongst these materials, the physical properties of GaN nanotubes have also been investigated mainly *theoretically* [160, 161, 162, 163]. Experimental studies on GaN nanotubes, however, have been much less frequently reported [154, 164]. This is presumably due to difficulties with their synthesis. Indeed, the literature on the fabrication of GaN nanotubes involves complex processes using templates and etching. In this chapter section, some properties of crystalline GaN nanotubes, formed by a novel self-assembly process on the top of GaN nanocolumns using plasma-assisted molecular beam epitaxy, are presented. The growth process is not yet well understood, but could become significant as

it provides a, hitherto elusive, technically simple synthesis method for GaN nanotubes. It is postulated that the nanotubes form from the coalescence of nanocolumns. The nanocolumns themselves were grown by Prof. Y. S. Park of Dongguk University, Korea, on a Si(111) substrate as described in chapter 2.8. A plan view SEM image of the nanotubes can be found in figure 7.1a), and a profile view in 7.1b). From the plan view it appears that both nanotubes and nanocolumns form during the growth process. The nanotubes form with an average wall thickness of 50 to 80 nm and an inner diameter of ~ 100 nm. A TEM image of a single column/tube is presented in figure 7.1c). It is clear that the nanotube forms on top of the nanocolumn, so it is postulated that the growth process starts via the formation of nanocolumns, before the onset of the appearance of nanotubes. One possible process is that the tubes form from the coalescence of 2 or more geographically close nanocolumns with a slight tilt between their (0001) axes, followed by, presumably, the filling in of some material between the columns to produce the nanotube side wall.

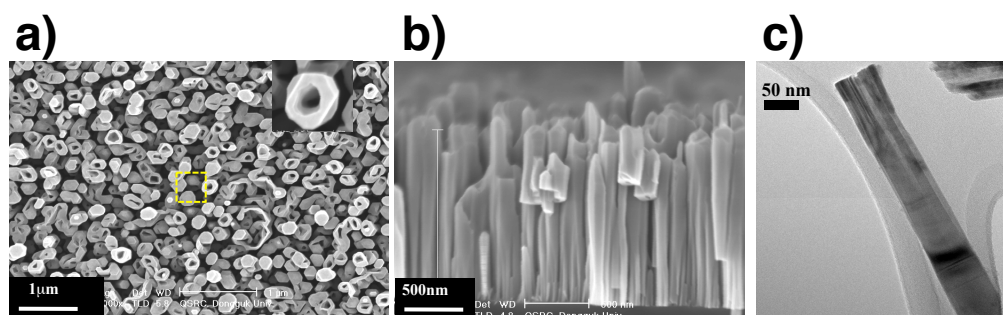


Figure 7.1: a) SEM micrograph in plan view of synthesised GaN nanotubes. b) SEM micrograph in profile view. c) Bright field TEM image of a single nanotube/nanocolumn. These electron microscope images were acquired by Prof. Y. S. Park of Dongguk University, Korea.

Some optical properties of these self-assembled GaN nanotubes will be presented here. Time resolved and time integrated microphotoluminescence studies (as described in chapter 4) have been performed in order to understand the properties of the nanotubes.

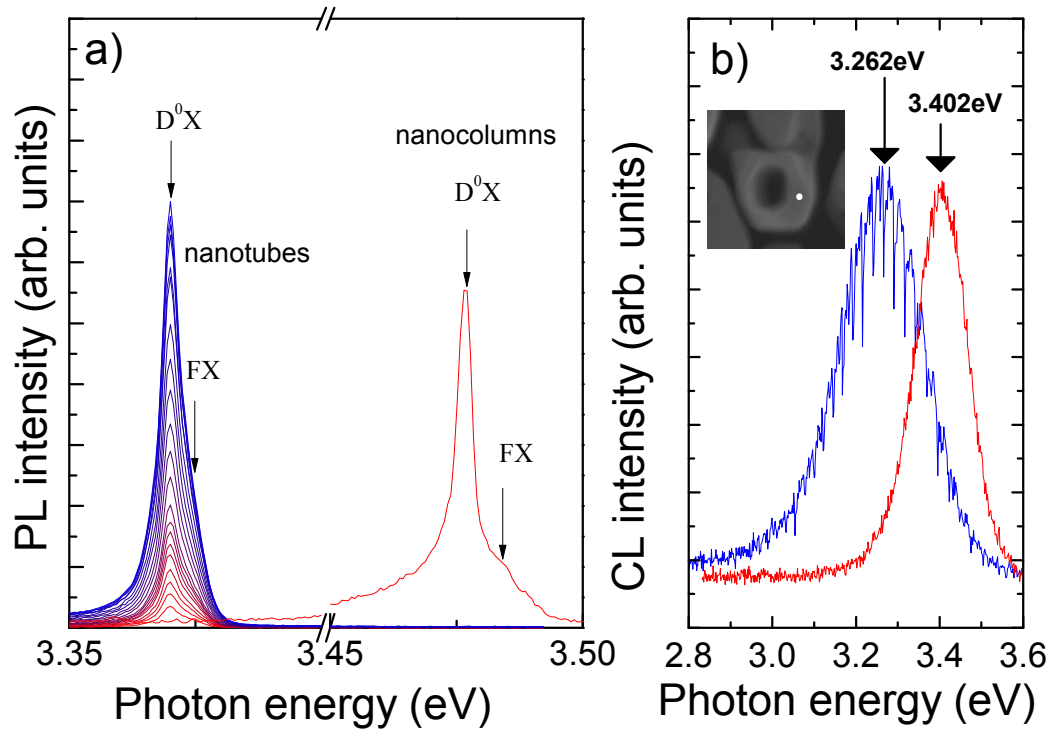


Figure 7.2: a) μ PL spectra measured as a function of excitation power density for nanotubes (from 1.3 kWcm^{-2} (red) to 21.6 kWcm^{-2} (blue)). The emission from a sample of nanocolumns is also presented for comparison, clearly showing the emission energy difference between the two samples. b) Spatially resolved CL spectra; The blue line is measured directly from a nanotube whereas the red line is measured from a nanocolumn. The inset shows the area of the nanotube that was excited by the electron beam (CL spectroscopy was performed by Prof. Y. S. Park of Dongguk University, Korea.)

7.1.1 Experimental studies on GaN nanotubes

μ -PL spectra from the GaN nanotubes (together with a spectrum of the GaN nanocolumns, for comparison) at 4.2 K are presented in figure 7.2a). As before, the excitation source was a frequency tripled pulsed Ti:Al₂O₃ laser at 266 nm, and the optical setup was exactly the same as that used for the experiments in the previous 2 chapters. Interestingly, the main emission of the nanotubes is observed to be red-shifted by $\sim 100 \text{ meV}$ with respect to the GaN nanocolumns/bulk GaN emission. This is in agreement with reference [154], in which a large unexplained red-shift was observed. The red-shifted emission is confirmed to originate from the nanotubes, by spatially resolved cathodoluminescence studies as shown in figure 7.2b).

It is clear that the main emission contains two peaks, these are found to be at $\sim 3.370 \text{ eV}$

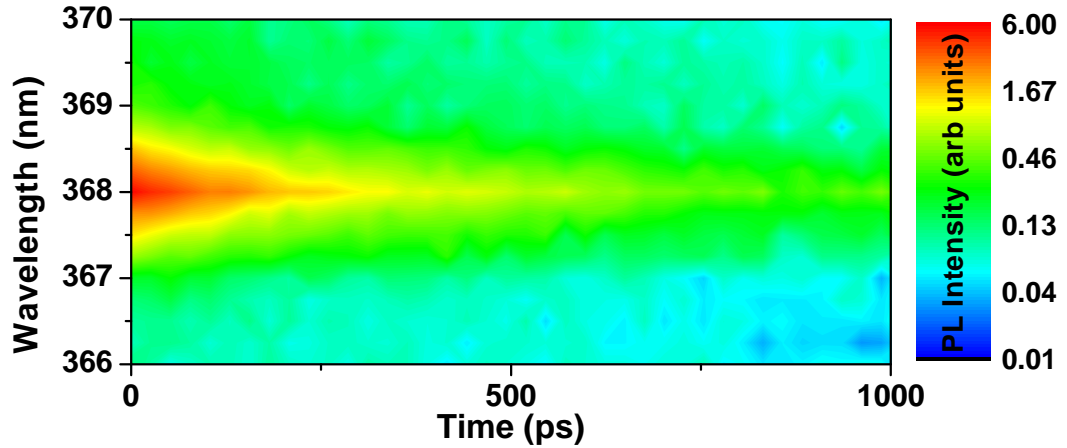


Figure 7.3: The TRPL decays measured across the emission peak from the GaN nanotubes. The emission is observed at constant energy throughout the decay.

and $\sim 3.374\text{eV}$ which are tentatively assigned to donor bound excitons and free excitons, respectively, as was done for the nanocolumns spectra in figure 5.1.

The temporal properties of the emission have also been investigated using the setup described in chapter 4. This time, due to fact that the dynamics occur on a faster scale than those of the QDisks investigated in chapter 5, an avalanche photo diode (APD) with time resolution of 40 ps was used (ID Quantique id100 series [165]) to detect the emission. The decays measured across the main emission peak (at 0.25 nm wavelength steps) from the nanotubes are presented in figure 7.3. It is clear that there is no shift in emission energy during the decay (within the resolution of the experiment). The peak emission decay is measured to be a monoexponential with lifetime $\sim 90\text{ ps}$ at 4.2 K^* . This lifetime is observed to decrease with increasing temperature (as shown in figure 7.4), probably due to increased non-radiative recombination. There is also the possibility that increased thermal energy of the carriers leads to enhanced non-radiative surface recombination (the surface volume ratio of nanotubes is enhanced) [166] though it is unclear how much this surface recombination effects the low temperature PL decay as the 90 ps lifetime measured for the nanotubes is very similar to the lifetime measured from pure GaN nanocolumns.[126]

*The decay time is not observed to change with excitation power.

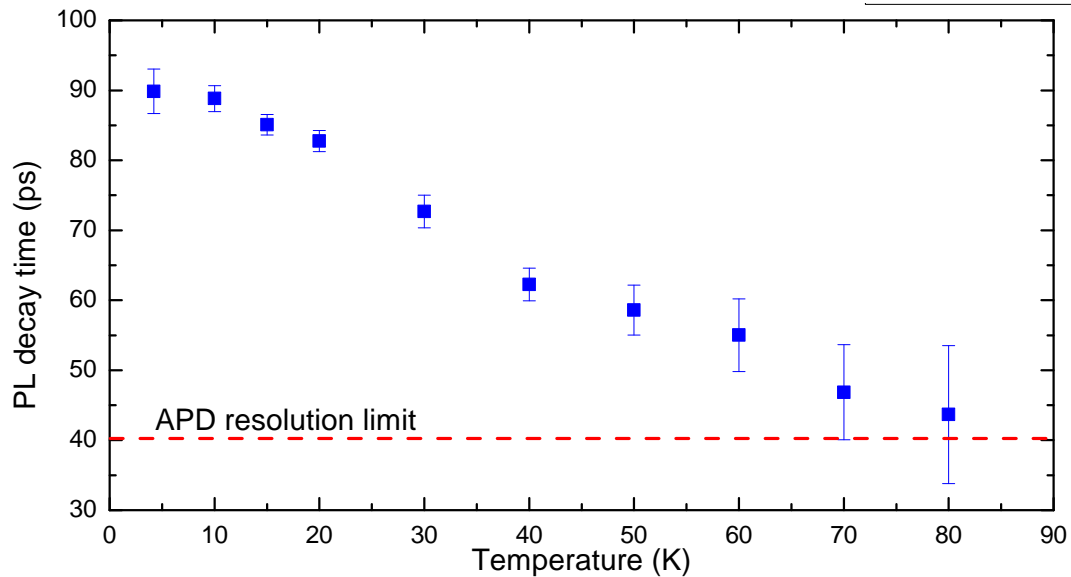


Figure 7.4: The decay lifetime of the nanotubes with increasing temperature. The lifetime becomes shorter as the temperature increases.

7.1.2 The red-shifted emission

The main contributing effects on the emission dynamics in nano-structured semiconductors are their dimensional size, potential variations, and internal strain. The GaN nanotubes wall thickness is > 50 nm, so it is not expected that any quantum confinement could effect the optical transition. As the nanotubes are composed of the binary material GaN, we should not expect any potential traps due to content fluctuations. Therefore, it seems reasonable that the change in emission energy could be produced by some internal strain[†]. Unfortunately, nextnano³ cannot be used to analyse this problem, as the c-axis of the constituent nanocolumns may not be pointing along the same direction. Thus, to confirm the existence of strain in the samples, Raman spectroscopy has been performed on the same samples by D. Wang, Y. Wang and M. Park of Furman University, South Carolina, USA, and Auburn University, Alabama, USA. The data that they have taken is presented in figure 7.5, along with a comparison from a sample of nanocolumns. The Raman peak from the Si substrates were observed at the same shift for both samples. For bulk single-crystalline GaN, the first-order phonon frequency of the $E_2^{(2)}$ mode

[†]Goldberger et. al. demonstrated that PL spectra in GaN nanotubes having thicker walls were more redshifted compared with those in GaN nanotubes having thinner walls (see the supplementary information of reference [154]) indicating that perhaps the strain does have an effect.

is 567 cm^{-1} at room temperature [167]. The energy of this peak is sensitive to stress and has been reported to shift at a rate of $-4.2\text{ cm}^{-1}/\text{GPa}$ when under tensile stress.[168] It can be seen clearly that the nanotubes are under at least 0.14 GPa more tensile stress than the nanocolumns are. Furthermore, it is important to note that the Raman spectrum of the nanotubes is contaminated by a contribution from nanocolumns which lie underneath the nanotubes. The actual difference in strain, then, could be much larger.

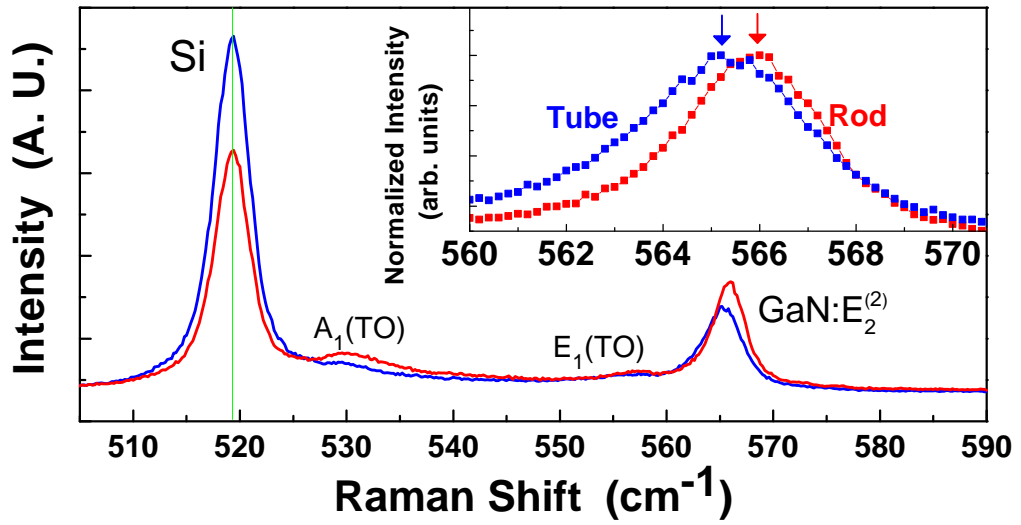


Figure 7.5: Raman spectra measured by D. Wang, Y. Wang and M. Park in the USA. The $E_2^{(2)}$ phonon energy is shifted for the case of GaN nanotubes, revealing that the nanotubes are under strain.

By making a quick calculation using equations 3.3 and 3.4 , it is clear that this value of stress is not enough to account for the red shift of 100 meV: By assuming an equi-biaxial strain ($\epsilon_{xx} = \epsilon_{yy} = -\frac{1}{2}\epsilon_{zz}\zeta_3/\zeta_1$ where $2\zeta_3/\zeta_1 \approx 2.26$ [169]) and using the values of the linear compliance tensor from reference [170], a stress of $\sim 1.67\text{ GPa}$ is required to account for the shift of 100 meV. It is clear that some other mechanism is producing the red shift in the emission. This is a continuing investigation.

7.2 Self-assembled GaN nano-pyramids grown on InGaN/GaN nanocolumns

As outlined in chapter 2.7, the induced strain in a epitaxially grown semiconductor due to lattice mismatch with the substrate can lead to the formation of dislocations within the material. One way to combat this was to perform epitaxial lateral overgrowth on specially patterned substrates, which resulted in the formation of hexagonal pyramid structures representing the underlying wurtzite structure of the GaN. Selective overgrowth on these pyramids then results in GaN layers with a lower density of dislocations [171].

These GaN pyramids have attracted considerable attention in their own right, due to their potential application in LED devices due to the strong field emission which they exhibit [172]. They are also seen as locations to grow quantum wells [173], and a possible method for site controlled growth of quantum dots [174, 175]. which would be a necessity for the real life implication of quantum key distribution protocols using semiconductor devices. To date most studies on GaN pyramids have focussed on micron scale pyramids (basal diameter), very few have been on nanopyramids [173, 176].

It has recently been discovered that by creating a nanocolumn with a stack of multiple quantum disks (10 QDisks in this case) and then performing further overgrowth,[‡] pyramidal structures grow from the *side wall* of the nanocolumn. This is a novel procedure for the growth of GaN pyramids, and, furthermore, the pyramids are only a few 100's of nanometers in diameter. The overgrowth procedure also results in continued nanocolumn growth along the axis of the original nanocolumn.

In figure 7.6(a), a high-resolution FESEM image of the self-assembled GaN nano-pyramids grown on the side walls (m-plane) of GaN nanocolumns is presented. The inset shows a zoomed in image in which the pyramids are clearly identifiable. The average diameter (measured from edge to edge) of the basal plane is about 150 nm. The angle between basal plane and the facets is 50°. In figure 7.6(b) an SEM image of the GaN nano-pyramids from above the columns is presented.

[‡]The overgrowth was performed using RF-plasma assisted molecular beam epitaxy, with the standard GaN growth conditions referenced in section 2.8.

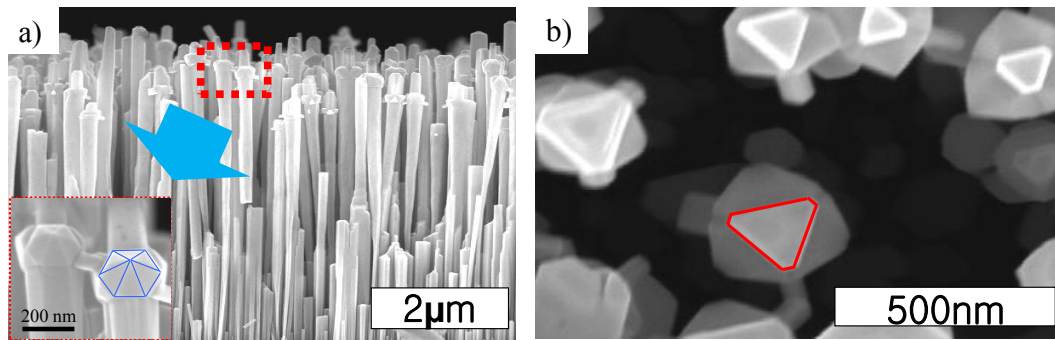


Figure 7.6: *a) SEM image of nanocolumns with protruding nanopillars (highlighted in the figure inset). b) Plan view of the same sample. These electron microscope images were acquired by Prof. Y. S. Park of Dongguk University, Korea.*

The nano-pyramids are clearly observed to protrude from the column in the lateral direction. Interestingly, the nano-pyramids preferentially grow along three axes, on alternate planes of the GaN nanorod. The growth of the nano-pyramids occurs only in the region of the InGaN QDisks, leading to the conclusion that the QDisks somehow seed the growth of the pyramids. This seeding may be due to some surface roughness after the growth of 10 QDisks, or be somehow related to the strain distribution on the sidewall of the column containing several QDisks (see figure 3.9). At present the mechanism that allows for c-plane growth of nanopillars on the m-plane of a GaN nanocolumn is unclear, and will require much more work and analysis at the growth stage. In the rest of this chapter the pyramids will be analysed.

Due to the proposed strain seeding of the pyramid growth, calculations of the strain tensor through the spatial extent of a nanopillar were also performed using `nextnano3`, as in chapter 3 for the nanocolumns and QDisks. As the exact induced strain from the column to the pyramid is unknown, a substrate of repeating units has been employed in the simulation to induce a strain at the base of the nano-pyramid with an arbitrarily chosen magnitude, but with the same spatial symmetry of the stack of the underlying 10 QDisks that induce the strain in the real case. The result can be found in Figure 7.7, in which the relaxation of strain is clearly visible along the growth axis of the nano-pyramid. The strain at the base of the pyramid mimics the pattern of the underlying QDisk stack, but soon averages to a smoothly varying distribution that decreases in magnitude towards the peak of the pyramid. The tip of the pyramid is fully

relaxed, in agreement with previous studies on GaN micro-pyramids [177]. This relaxation in strain will result in a luminescence emission energy that becomes increasingly blueshifted as we move from the base to the tip of the pyramid. In order to elucidate the strain status of the nano-pyramids, CL studies were performed at room temperature on a single nanorod/nano-pyramid system at discrete positions along the axis of the rod by Prof Y. Park of Dongguk University, Korea. (See Figure 7.8(a)).

The CL studies were performed at room temperature using a 10 kV electron beam. In this experimental configuration, the nanocolumn is being excited laterally by the electron beam, whereas the nanopyramid is being excited along its growth axis. The collected CL then also comes laterally from the nanorod and on-axis from the nano-pyramid. CL spectra were taken from 9 positions along the length of a single nanocolumn, the positions are labelled P1-P9 in figure 7.8. A strong emission with a FWHM of ~ 110 meV near 3.41 eV is observed at

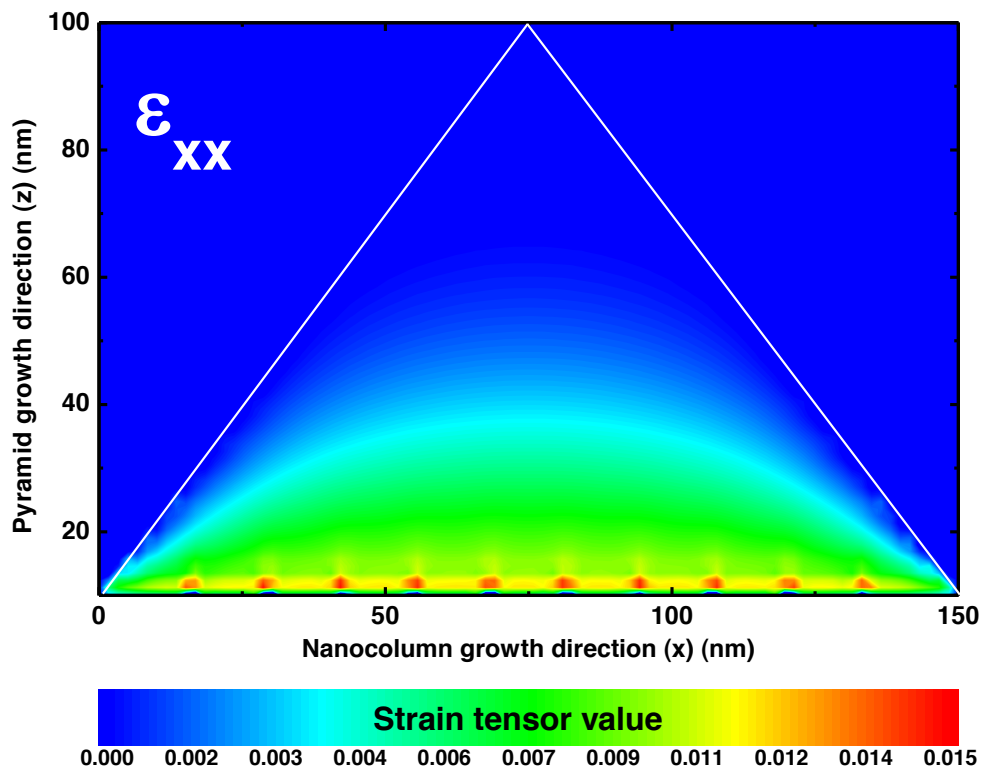


Figure 7.7: A plot of the ϵ_{xx} component of the strain tensor for a cross section through a nanopyramid. The strain becomes relaxed towards the tip of the pyramid.

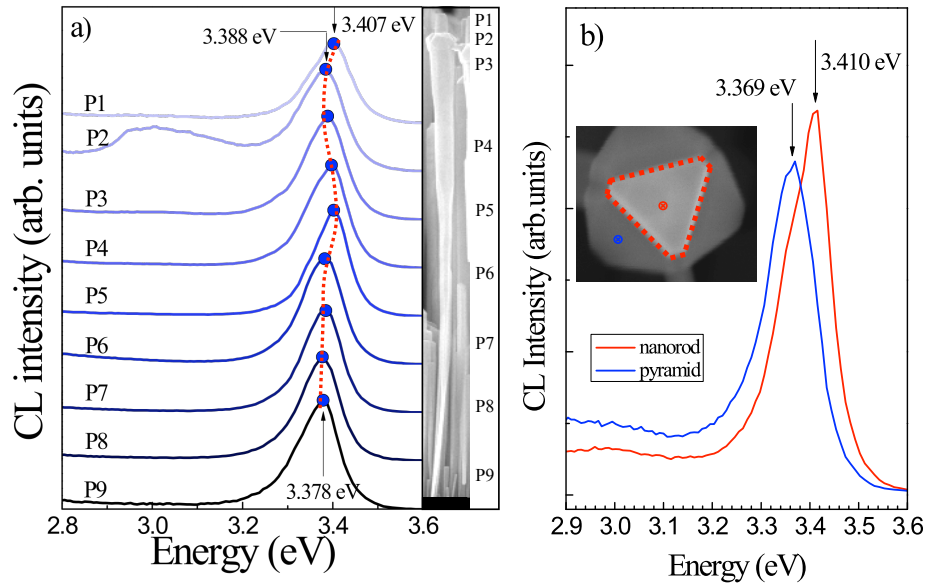


Figure 7.8: a) CL spectra measured at various positions along the length of the nano column. b) CL spectra measured from the tip of the column (red) and the side of a nanopillar (blue). The CL spectroscopy was performed by Prof. Y. S. Park of Dongguk University, Korea.

position P1, corresponding to the tip of the nanocolumn. This emission line comes from the room temperature GaN band edge emission. At position P2 (corresponding to the GaN nanopillars and InGaN/GaN QDisk region) the emission line red-shifts to 3.39 eV, which is in good agreement with that previously measured from GaN micro-pillars reported by Cho *et al.* [178]. The red shift from the nanocolumn emission indicates the presence of strain in the nano-pillar. Moreover, an additional broad emission near 3.00 eV is observed, due to emission from carriers localized in the InGaN/GaN quantum disks (this is effectively the luminescence that has been analysed in the previous two chapters). As the electron beam is brought towards position P5, the QDisk emission becomes diminished and the main CL emission is observed to gradually blue-shift back to the energy at which it was initially observed in position P1. As the electron beam is directed to positions P7-P9, the emission line again begins to red-shift to a value of 3.38 eV (most probably due to increased strain near the GaN-Si interface).

One may expect there to be a variation of emission energy within the pillars themselves due to the strain relaxation along the growth axis. However, due to the nature of the

nanopyramids, it is very difficult to observe any spatial variation in the emission energy (even CL techniques, which offer the same spot size as the host electron beam microscope, do not have the required resolution due to spreading of the electron beam within the material.) However, it is possible to observe the shift in emission between the base and the tip of the pyramid by electron beam excitation in different orientations, as explained below.

Figure 7.8(b) shows additional CL spectra measured this time from the top of the column as indicated in the figure inset. Note that this corresponds to a lateral excitation and collection of the pyramid CL, and an on-axis excitation/collection of the nanorod CL. In this orientation the emission energy of the GaN nanorod is observed near 3.41 eV, which is the same as the emission when excited and collected laterally. The CL energy of the nano-pyramid, however, is observed near 3.369 eV, which is redshifted by ~ 19 meV compared to when it was excited along its growth axis. This can be explained by analysis of the excitation geometry: When the pyramid was excited along the growth axis, the tip of the pyramid (and the region below the tip) was selectively excited, whereas in this orientation it is the middle and base that is being excited, which results in a small, but resolvable red-shifted pyramid emission. A similar analysis was performed by Zeng *et al* on micropyramids using μ -PL techniques [179].

7.2.1 Summary

In summary, a novel method for the production of self assembled GaN pyramids via a lateral growth on a stack of InGaN QDisks has been shown. Furthermore the pyramids formed by this method are nano-sized, and thus orders of magnitude smaller than GaN pyramids in the current literature. The strain within one of these nano-pyramids was simulated and a relaxation was found along the nanopyramid growth direction, which is in agreement with previous studies on micron-scale pyramids.

8

Summary, Outlook, and Concluding Remarks

The work presented in this thesis is a step along the road to the fabrication and understanding of many devices using III-Nitride nanocolumns. These structures may well find several future uses in UV, or blue light detection systems, biosensors, or indeed more efficient LED structures. The manufacture of any of these devices will require a sound understanding of the underlying physics and internal dynamic processes of the structures. In this case the strain, an inherent problem for nitrides in this current stage of maturity, has been considered for QDisks embedded in nanocolumns. It has been established that there is no extreme lateral charge separation within the QDisks, but that there is a separation of charge along the growth axis due to the quantum confined Stark effect. Further to this, both the spatial and temporal distribution of carriers after laser excitation along a single column has been mapped.

Other work on the optical characterisation of GaN nanopyramids and nanotubes has also been presented. These structures are still in their infancy, but may contribute to further interesting device technologies in the future. The seeding of quantum dots, for example on the side walls of nanocolumns which themselves are aligned in a regular array into which a photonic crystal waveguide can be produced could lead to a direct one chip system for the addressing and read-out of qubit states from a fixed location. Indeed, the same chip could be used to investigate

cavity quantum electrodynamics by having the active quantum dots located at the centre of a microcavity, or indeed nanocavity. Of course, that is not to mention that fact that this could be done at wavelengths across all of the visible range of the electromagnetic spectrum (and into the IR and UV too) all with a single material system.

It is clear that III-Nitride materials will play an important role in the future of the semiconductor electronics/optoelectronics industry. They provide an excellent platform for the architecture of an incredible variety of devices. Although undoubtedly a key factor of their widespread use will be their uptake in the lighting industry (LEDs), the opportunities to further increase device performance by nanoscale fabrication, or indeed the fabrication of novel device systems, will lead to a long future of use.

Appendices



Non Linear Optical Effects

Non linear optical effects are effects that manifest themselves through a non-linear response in the polarisation, \mathbf{P} , of a medium to an applied electric field, \mathbf{E} . This is generally written as a power series,

$$\mathbf{P} = \epsilon_0[\chi^{(1)}\mathbf{E} + \chi^{(2)}\mathbf{E}^2 + \chi^{(3)}\mathbf{E}^3 + \chi^{(4)}\mathbf{E}^4 + \dots], \quad (\text{A.1})$$

where $\chi^{(n)}$ is the n^{th} -order electric susceptibility tensor. The elements of each successive tensor become increasingly smaller such that higher order non-linear effects are observed only at very high intensities.

A.1 The Kerr Effect and Kerr Lens Modelocking

The Optical Kerr effect is a third order ($\chi^{(3)}$) non-linear effect that establishes itself as an intensity dependent index of refraction. The dielectric constant, ϵ_r , for a non-linear medium is given by

$$\begin{aligned}
\epsilon_r^{nl} &= 1 + \chi^{(1)} + \chi^{(3)} \mathbf{E}^2 \\
&= \epsilon_r + \chi^{(3)} \mathbf{E}^2.
\end{aligned}
\tag{A.2}$$

The total, non-linear, refractive index, n^{nl} , is thus given by

$$\begin{aligned}
n^{nl} &= \sqrt{\epsilon_r + \chi^{(3)} \mathbf{E}^2} \\
&= \sqrt{\epsilon_r} + \frac{\chi^{(3)}}{2\sqrt{\epsilon_r}} \mathbf{E}^2 \\
&= n_0 + n_2 I,
\end{aligned}
\tag{A.3}$$

which is clearly dependent on the Intensity of the electric field. Thus, a laser beam propagating through a medium which exhibits a non-zero $\chi^{(3)}$ will affect the refractive index of the medium as it passes through it. The profile of a laser beam is well approximated to a Gaussian function and the centre of the beam is more intense than the extremities. A laser beam propagating through such a medium will thus undergo self focusing due to the refractive index differential across it's profile.

One can take advantage of this effect in laser cavities. Pulsed modes of the cavity will have a lower mode volume than CW modes, due to the Kerr Lens effect. A slit positioned in the cavity can thus be used to create losses in the CW mode (partially blocked by the slit) but not in the pulsed mode (passing directly through the slit). The presence of the slit can thus lock the laser to emit pulsed packets of high peak intensity. This effect is used in the Ti:Al₂O₃ lasers used through this study.

B

Estimating the $\text{In}_x\text{Ga}_{1-x}\text{N}$ QDisk Indium Content

In order to estimate the indium content of the InGaN QDisks, we use a simple model to evaluate the expected emission energies for a 20 \AA thick QDisk with diameter 140 nm . The internal field, and the screening thereof is assumed to perturb these energy states. The data for this analysis is presented in figure B.1.

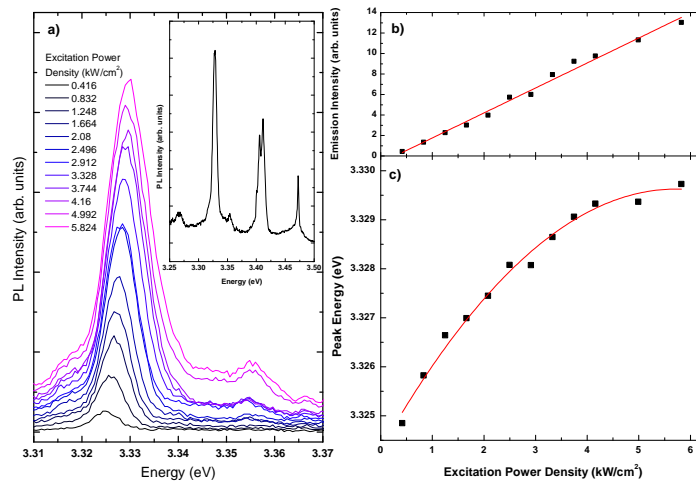


Figure B.1: The excitation power density dependence of the PL emission from a single $\text{In}_x\text{Ga}_{1-x}\text{N}$ QDisk embedded in a GaN nanocolumn at 4 K.

The QDisk has been modelled with a circular cross section of radius ρ , and finite width w as shown in schematic form, contrasting to the actual situation, in figure B.2. The indium content was assumed constant throughout the volume of the disk, and the GaN band gap was set to 3.515 eV [180]. The confinement provided at the $\text{In}_x\text{Ga}_{1-x}\text{N}/\text{GaN}$ interfaces produces a finite quantum well of width w and depth, V , which is equal to the band offset between $\text{In}_x\text{Ga}_{1-x}\text{N}$ and GaN. Limited confinement is provided by the finite diameter of the column, which has been modelled as an infinite well of width 2ρ .

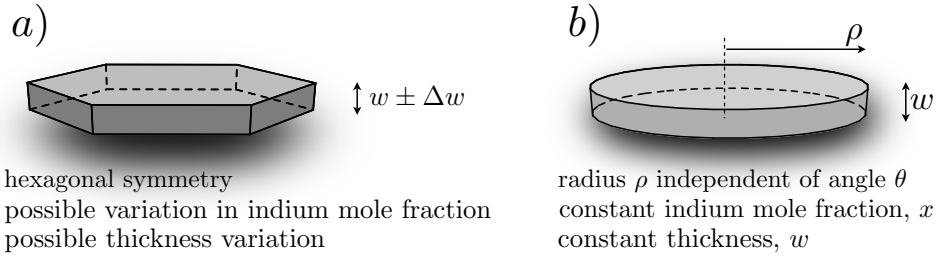


Figure B.2: A Schematic diagrams of a) a hexagonal disk, and b) the modelled quantum disk.

The QW energy levels (in the absence of an electric field) of such a confinement geometry can be readily calculated as the sum of contributions from both the confinements parallel and perpendicular to the axis of the disk: $E_{n,F=0} = E_n^{\text{fqw}} + \hbar^2 \epsilon_{\alpha m}^2 / 2m^* \rho^2$, where E_n^{fqw} is the n^{th} energy level of a finite quantum well, m^* is the carrier effective mass in the well, and $\epsilon_{\alpha m}$ is the m^{th} root of the Bessel function (J_α) of integer order α . As E_n^{fqw} is proportional to w^{-2} , and $\rho \gg w$, the confinement energy due to the finite extent of the disk is much smaller than that due to the bandgap offset between $\text{In}_x\text{Ga}_{1-x}\text{N}$ and GaN. These energies are levels are found numerically, and it is found that only one bound state exists for both electrons and holes in the conduction and valance bands respectively for the range . This is in agreement with the spectra observed in figure B.1, in which no $n = 2$ emission is observed.

The shifts of the ground state energy levels in the presence of an electric field F (the quantum confined Stark effect) have been calculated using the results of the variational technique of Bastard *et al* [65] for a weak field, parallel to the axis of the disk. The weak field limit is valid in this case as the total shift is measured to be ~ 5 meV, whereas the energy of confinement is

~ 100 meV and ~ 20 meV for electrons and holes respectively. The electrons are about 5 times lighter than the holes so they will be affected more strongly by the field, such that the energy shift for electrons and holes is ~ 4.2 meV and ~ 0.8 meV respectively. These values are over an order of magnitude lower than the respective energies of confinement. The shift of the ground state energy level for the case outlined above is,

$$\Delta E_1 = -\frac{\Omega^2 m^* e^2 w^4}{8 \hbar^2} F^2, \quad (\text{B.1})$$

where

$$\Omega(k_0, q_0) = A \left[\frac{1}{3} + \frac{\sin k_0}{k_0} + \frac{2 \cos k_0}{k_0^2} - \frac{2 \sin k_0}{k_0^3} + \frac{2}{q_0} \left[1 + \frac{2}{q_0} + \frac{2}{q_0^2} \right] \cos^2 \left[\frac{k_0}{2} \right] \right], \quad (\text{B.2})$$

$$A = \left[1 + \frac{\sin k_0}{k_0} + \frac{2}{q_0} \cos^2 \left[\frac{k_0}{2} \right] \right]^{-1}, \quad (\text{B.3})$$

and q_0 and k_0 are the wavevectors

$$q_0^2 = \frac{2m^* w^2}{\hbar^2} (V - E_1), \quad k_0^2 = \frac{2m^* w^2}{\hbar^2} E_1, \quad (\text{B.4})$$

respectively [65].

Bringing together the coefficients of the magnitude of the ground state energy shifts, the transition energy, ξ , between the conduction and valence band $n = 1$ states can be expressed as

$$\xi(F) = \xi(0) - (\gamma_{cb} + \gamma_{vb}) F^2, \quad (\text{B.5})$$

where γ_{cb} and γ_{vb} are the coefficients of the shift in the conduction and valence bands respectively. The photo-generated carrier density in the well is proportional to the excitation power density for a pulsed excitation when the pulse separation is much longer than the carrier lifetime. We finally

assume that the screening field is proportional to the carrier density such that $F \approx F_{\text{int}} - \phi P$, equaling just the internal field in the limit of zero excitation. A similar assumption was used by Kuokstis *et al.* [138] when they measured the internal field in InGaN multiple quantum wells. Equation B.5 can thus be rewritten as a function of the internal field and excitation power density;

$$\xi(P, F_{\text{int}}) = \xi(0, 0) - \gamma F_{\text{int}}^2 + 2\gamma\phi F_{\text{int}}P - \gamma\phi^2 P^2, \quad (\text{B.6})$$

where $\gamma (= \gamma_{cb} + \gamma_{vb})$ can be calculated for a range of values of indium mole fraction and well depth. For this study the values of the electron and hole effective masses were assumed temperature independent and taken from Takeda *et al.* [181]. The conduction and valance band offsets were interpolated from data by Wu *et al.* [182] with a bowing parameter of 1.43 eV [43] and a band offset ratio of $V_c : V_v = 0.55 : 0.45$ [181].

Equation B.6 can be fit to the data in figure 5.6c, and hence, from the constants of the fit and the calculated values of γ , a parameter space of indium mole fraction, well width, and ground state emission energy can be evaluated. A plot of this parameter space is shown in figure B.3.

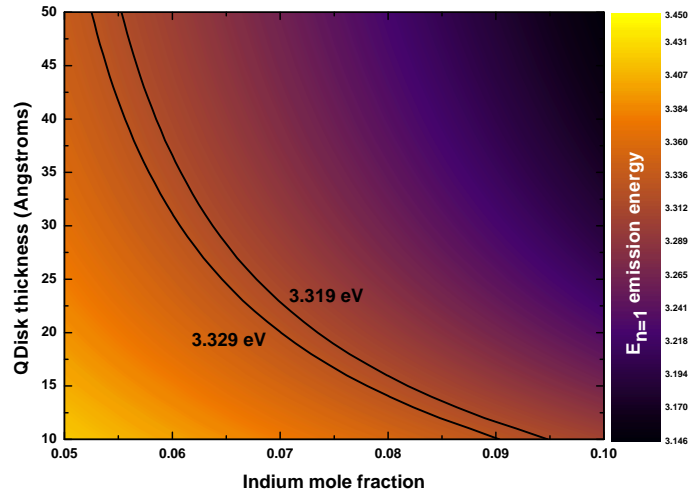
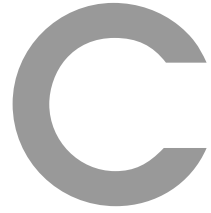


Figure B.3: The parameter space for ground state emission energy ξ , indium mole fraction x , and quantum well width, w . The space has been calculated from the energy shift model outlined here and the fit to experimental data. The contours at 3.319 eV and 3.329 eV bound the values of x and w .

As the zero compensated emission lies at $\xi = 3.324$ eV (extrapolated from the data in

figure 5.6), contour lines at energies of 3.319 eV and 3.329 eV have been added to the plot to establish bounds on the region in which we are interested. The indium mole fraction is found to be $x \approx 0.07$, which is a little lower than the value of 0.1 which was aimed at during growth, though not too surprising given the low incorporation rates of indium during MBE growth.

In this analysis the exciton binding energy has been neglected, resulting in a slight over-estimation of the indium content.



Cleanroom Processing

C.1 E-beam lithography

Resist	PMMA A8	ZEP 520A
Spin	4500 rpm for 60 s (800 μm)	4500 rpm for 60 s (600 μm)
Bake	180 °C for 90 s	180 °C for 120 s
Exposure	500 $\mu\text{C}/\text{cm}^2$	120 $\mu\text{C}/\text{cm}^2$
Development	MIBK:IPA (1:3) 60 s	ZED-N50 90 s (23 °C)
Removal	Acetone	DMAC or NMP (30-35 °C)

C.2 Process: Single nanocolumn sample

Process step	Comments
<p>Metal Evaporation</p> <ul style="list-style-type: none"> • Clean quartz sample in Acetone and IPA. • Load into Edwards auto 306 evaporator & pump to 10^{-6} mbar. • Evaporate 65 nm Au at a current of ~ 3 A (0.1 nms^{-1}). • Leave to cool for ~ 30 minutes and remove sample. 	
<p>Coating with PMMA</p> <ul style="list-style-type: none"> • Use a syringe to place 2-3 drops of PMMA A7 on sample through a filter. • Spin the sample at 4500rpm for 60s. to produce ~ 800 nm layer of PMMA. • Heat the sample to 180°C for 90s to evaporate solvent. • Check to see if sample is coated evenly. 	
<p>Electron beam lithography.</p> <ul style="list-style-type: none"> • Load sample into JEOL 5500ZC e-beam writer and check chamber pressure $\leq 1.5 \times 10^{-5}$ mbar. • Set beam current to 1 nA and EOS to mode 2. Calibrate system. • Expose pattern Au_mask.sdp at desired positions on sample. Make sure Dose is at $500 \mu\text{Ccm}^{-2}$. • Remove sample from e-beam writer. 	
<p>Development and wet etch</p> <ul style="list-style-type: none"> • Develop exposed sample in MIBK:IPA (1:3) for 60s (room temperature). • Rinse in IPA. • Check exposure in optical microscope. • Etch Au using gold etch (neat) for 5s. 	
<p>Scattering of nanocolumns</p> <ul style="list-style-type: none"> • Pipette 2-3 drops of nanocolumns in methanol solution onto the sample. • Wait for methanol to evaporate and check sample in optical microscope. 	

C.3 Process: Mask for single QD excitation

Process step	Comments
<p>Metal Evaporation</p> <ul style="list-style-type: none"> Al evaporation performed by Richard Makin of Thin Film Facility using e-beam evaporator (100 nm). 	
<p>Coating with PMMA</p> <ul style="list-style-type: none"> Use a syringe to place 2-3 drops of PMMA A7 on sample through a filter. Spin the sample at 4500 rpm for 60s. to produce \sim 800 nm layer of PMMA. Heat the sample to 180 °C for 90 s to evaporate solvent. Check to see if sample is coated evenly. 	
<p>Electron beam lithography.</p> <ul style="list-style-type: none"> Load sample into JEOL 5500ZC e-beam writer and check chamber pressure $\leq 1.5 \times 10^{-5}$ mbar. Set beam current to 1 nA and EOS to mode 2. Calibrate system. Expose pattern qd_mask.sdp at desired positions on sample. Make sure Dose is at $500 \mu\text{Ccm}^{-2}$. Remove sample from e-beam writer. 	
<p>Development and wet etch</p> <ul style="list-style-type: none"> Develop exposed sample in MIBK:IPA (1:3) for 60 s (room temperature). Rinse in IPA. Check exposure in optical microscope. Etch Al using Decon 90:H₂O (1:10). 100 nm in 60s. Check sample in optical microscope. 	



nextnano³ input file

A brief explanation of the input file used to generate the strain profiles in nextnano³ can be found here. For simple strain calculations, the input file consists of 2 main sections. they are:

1. Initial set-up
2. Domain geometry

The initial setup consists of several subsections, though they are mainly attributed to more advanced functions, such as $k \cdot p$ modelling and Shrodinger equation solving. These functions are not employed in this study due to lack of computer processing power. Initially the maximum number of strain iterations and also the minimum residual that must be returned (defining convergence) are set.

```
!-----!  
$numeric-control !  
  varshni-parameters-on = yes !  
  strain-iterations      = 2000 !  
  strain-residual        = 1d-16 !  
$end_numeric-control !  
!-----!
```

Next the dimension of the simulation are defined to be 3, and the orientation to be 1 1 1 (meaning that the simulation will be carried out in all 3 dimensions). The global parameters are also set now (the lattice temperature is held at 4K).

```

!-----!
$simulation-dimension      !
  dimension      = 3      !
  orientation = 1 1 1    !
$end_simulation-dimension  !
!-----!

```

```

!-----!
$global-parameters      !
  lattice-temperature = 4d0 !
$end_global-parameters  !
!-----!

```

Next the method of strain simulation is chosen. In this case a strain minimisation model is selected. This minimises the elastic strain energy of the system in order to find the strain tensor at the grid points of the simulation which are defined in the domain geometry section. The *substrate-cluster-number* parameter defines which part of the structure will be chosen as the substrate (zero strain). *Neumann* boundary conditions are selected to ensure that derivative of the stress tensor is zero at the boundaries (i.e. no external forces act on the system).

```

!-----!
$simulation-flow-control  !
  flow-scheme      = 0    !
  strain-calculation = strain-minimization !
$end_simulation-flow-control !
!-----!

```

```

!-----!
$strain-minimization-model !
  substrate-cluster-number = 4 !
  boundary-condition-x     = neumann !
  boundary-condition-y     = neumann !
  boundary-condition-z     = neumann !
$end_strain-minimization-model !
!-----!

```

Once the initial set-up section of the file has been prepared, the domain geometry of the system to be simulated (in this case the nanocolumn and QDisk) must be chosen. In order to do this, the volume of the simulation, then crystal axes of our structure, and the growth direction, are all defined. The domain type is set to be (111)* before the size of the area to be simulated is input. In this case the volume within which the simulations will occur is a cuboid of dimension 140 nm×140 nm×100 nm. Next, the relation between the co-ordinate axes of the material system (wurtzite GaN) and the cartesian co-ordinates of the simulation volume is defined.

*the same condition as the orientation, above.

```

!-----!
$domain-coordinates
domain-type      = 1 1 1
x-coordinates    = 0d0 140d0
y-coordinates    = 0d0 140d0
z-coordinates    = 0d0 100d0
hkil-x-direction = 1 0 -1 0
hkil-y-direction = -1 2 -1 0
hkil-z-direction = 0 0 0 1
growth-coordinate-axis = 0 0 1
pseudomorphic-on = GaN
$end_domain-coordinates
!-----!

```

Now the regions that the structure comprises of must be defined, and then materials can be attributed to them. Each region has a unique number, and if any two regions occupy the same space, the region with the higher number takes precedence. It is possible to define many shapes in nextnano³, but for the purpose of simulating the strain in a hexagonal nanocolumn, just cubes and hexagonal obelisks will suffice. In the section below, region one will be air, which will completely fill the simulation volume. Here, region 5 will be the substrate, and regions 2, 3 and 4 form the main body of the nanocolumn, the QDisk and the capping layer respectively.

```

!-----!
$regions
region-number    = 1
base-geometry    = cuboid
region-priority  = 1
x-coordinates    = 0d0 140d0
y-coordinates    = 0d0 140d0
z-coordinates    = 0d0 100d0

region-number    = 5
base-geometry    = cuboid
region-priority  = 1
x-coordinates    = 0d0 140d0
y-coordinates    = 0d0 140d0
z-coordinates    = 0d0 2d0

region-number    = 2
base-geometry    = hexagonal-obelisk
region-priority  = 2
base-coordinates = 0d0 140d0 0d0 140d0 2d0 2d0
top-coordinates  = 0d0 140d0 0d0 140d0 92d0 92d0

region-number    = 3
base-geometry    = hexagonal-obelisk
region-priority  = 3
base-coordinates = 0d0 140d0 0d0 140d0 92d0 92d0
top-coordinates  = 0d0 140d0 0d0 140d0 95d0 95d0
!-----!

```

```

region-number      = 4
base-geometry      = hexagonal-obelisk
region-priority    = 2
base-coordinates   = 0d0 140d0 0d0 140d0 95d0 95d0
top-coordinates    = 0d0 140d0 0d0 140d0 100d0 100d0
$end_regions
!-----!

```

The grid over which the simulation will be run must now be defined. These grid points are the locations at which the strain will be calculated, so more grid points will enable a more accurate simulation, but the processing time will increase rapidly as the simulation has been defined to be in 3D. Once the grid is defined, clusters are defined; each cluster can contain several region numbers, but is made of a single material. This may seem like an annoyance for simple structures like those simulated here, but is useful when simulating complicated structures, with many spatially distinct parts consisting of the same material.

```

!-----!
$grid-specification
grid-type          = 1 1 1
x-grid-lines       = 0d0 140d0
x-nodes            = 50
x-grid-factors     = 1d0
y-grid-lines       = 0d0 140d0
y-nodes            = 50
y-grid-factors     = 1d0
z-grid-lines       = 0d0 2d0 92d0 95d0 100d0
z-nodes            = 2 90 3 5
z-grid-factors     = 1d0 1d0 1d0 1d0
$end_grid-specification
!-----!

```

```

!-----!
$region-cluster
cluster-number = 1    region-numbers = 1 6
cluster-number = 2    region-numbers = 2 4
cluster-number = 3    region-numbers = 3
cluster-number = 4    region-numbers = 5
$end_region-cluster
!-----!

```

Finally the clusters are filled with materials, and the mole fraction of the $\text{In}_x\text{Ga}_{1-x}\text{N}$ QDisk is input.

```

!-----!
$material
material-number = 1
material-name    = Air-wz
cluster-numbers = 1
!-----!

```

```

material-number = 2                                     !
material-name   = GaN                                  !
cluster-numbers = 2                                     !
                                                        !
material-number = 3                                     !
material-name   = In(x)Ga(1-x)N                       !
cluster-numbers = 3                                     !
alloy-function  = constant                             !
                                                        !
material-number = 4                                     !
material-name   = GaN                                  !
cluster-numbers = 4                                     !
$end_material                                        !
!-----!
!-----!
$alloy-function                                       !
material-number   = 3                                  !
function-name     = constant                           !
xalloy            = 0.1d0                              !
$end_alloy-function                                    !
!-----!

```

This file, when run in `nextnano3` will generate a strain profile through out the entire hexagonal obelisk that defines the GaN nanocolumn containing an $\text{In}_{0.1}\text{Ga}_{0.9}\text{N}$ QDisk. Further information on the operation of `nextnano3` can be found on the website of the software [93].



Superconducting Nanowire Single Photon Detector

The nanocolumnar samples investigated in this thesis emit in the UV-blue region of the electromagnetic spectrum. Silicon is a suitable material to use to detect this light. For devices made to emit in the IR though, there is a lack of suitable detection material. In this appendix the manufacture and characterisation of a superconducting detector for IR single photons is presented.

E.1 Current State of the Art

Silicon based diodes are used for detecting visible and UV photons (200nm-1100nm) [183], but their sensitivity, and thus detection efficiency dies off towards the extremes of this range.* InGaAs based diodes are used in the infra-red [185, 186, 187], but are usually cooled to ~ 200 K and are less efficient than their Si-based brethren.† InGaAs APDs have time resolutions of approximately 0.5 ns [189], which is limited due to jitter and electrical noise, whereas good Si APDs can have time resolutions of ~ 20 ps. There is a lack of commercially available high efficiency detectors for the infra-red that have good time resolution. A summary of current single photon detectors can be found in table E.1

In order to be able to detect single photons from, and indeed measure the lifetimes of, InAs QDs, A relatively novel type of detector: a Superconducting Single Photon Detector (SSPD) is

*Si based APDs have, however been used to detect X-rays [184].

†Germanium based detectors have also been investigated, but require cooling to ~ 77 K [188].

Detector Type	T (K)	QE (η)	IRF FWHM	Dark Counts	Count rate
Si APD	250	70 %	50 ps	25 Hz	10 MHz
InGaAs APD	200	10 %	370 ps	90 Hz	10 kHz
SNSPD	3	0.7 %	60 ps	10 Hz	100 MHz
TES	0.1	50 %	100 ns	3 Hz	100 kHz

Table E.1: A summary of the properties of current state of the art Single Photon Detection systems.

being constructed, which could boast electronic noise limited time resolutions down to ~ 20 ps [190, 189]- comparable to that of Si APDs. This particular breed of detector works by holding a niobium nitride (NbN) nanowire in its superconducting phase, carrying a current just below its critical current I_c . The nanowire is used as the detector, and coupled to it is an optical fibre to carry the input signal. When a photon is incident on the nanowire, the absorbed energy causes a ‘hotspot’ to be formed, from which the supercurrent is expelled. The current is thus forced to circumvent the hotspot, increasing the current flow in the surrounding region to a value exceeding I_c . The nanowire almost instantaneously loses its superconducting properties, and the photon is detected as a voltage spike on the nanowire [191, 189, 192, 193, 194]. An obvious benefit of such a set-up is that although there will be inherent wavelength dependence, the detector may be used to detect single photons across all of the visible spectrum and far into the infra-red, theoretically up to $\lambda = 10 \mu\text{m}$ [190].

E.2 Theory of Superconducting Nanowire Single Photon Detectors

As with all photon detectors, the principle operation of the SNSPD is to convert an optical signal into an electrical signal which is then counted with sophisticated counting system. The conversion of the optical signal to an electrical signal is fairly simple. A superconducting nanowire is cryogenically cooled to below its critical temperature, T_c , such that it enters the superconducting phase [195, 196] and expels magnetic flux due to the Meisner-Oschenfeld effect [197]. In this state, current in the nanowire is carried by Cooper pairs [198] generated by electron phonon interactions. The superconducting state is fragile and bound by three parameters; The critical temperature,

T_c , critical field, H_c and critical current density, J_c . Should either the temperature, field or current density exceed their respective critical values, a catastrophic fail of the superconductor will result whereby the nanowire will no-longer support a superconducting current and will return to a state with finite non-zero resistance. The SNSPD works on detecting the transition of the nanowire from superconducting to normal state invoked by the absorption of a photon.

The nanowire is biased with a dc voltage source such that it carries a current density $J < J_c$. Photons incident on the detector will cause break up of the Cooper pairs by creating a local hotspot [199], which the superconducting current is forced to circumvent. The current density in the region into which the diverted current flows locally exceeds J_c and the nanowire is forced to enter its normal resistive mode. With the sudden onset of finite resistance, a potential is dropped over the wire. This occurs on a time scale of ~ 200 ps (rise time) and remains for ~ 10 ns as the nanowire returns to its superconducting state (see figure E.5). The width of the voltage spike defines the dead time of the detector, i.e. the duration within which further photons cannot be detected. The dead time is limited by the kinetic inductance, L_k , of the wire [200, 201, 202] and can be thought of as a relaxation time, within which electrons are diverted through a 50Ω shunt resistor. A dead time of 10 ns enables the detector to theoretically detect photons at a rate of 100 MHz. The process is explained diagrammatically in figure E.1.

E.3 Niobium Nitride Nanowire

The detectors used in this investigation consist of fibre coupled niobium nitride (NbN) nanowires that were created at the National Institute of Information and Communications Technology (NiCT) in Japan. A ~ 4 nm thin film of NbN was deposited epitaxially onto a single crystal MgO substrate by reactive dc-magnetron sputtering and the processed by electron beam lithography (EBL) and reactive ion etching (RIE) into a nanowire meander. The critical temperature, T_c , for bulk NbN is 17.3 K [203] but this has been measured to be as low as 7 – 10 K for thin film NbN [204, 205].[‡]

[‡]High T_c superconductors have not been used for SNSPDs to date due to the lack of suitable substrates onto which high quality thin films can be deposited.

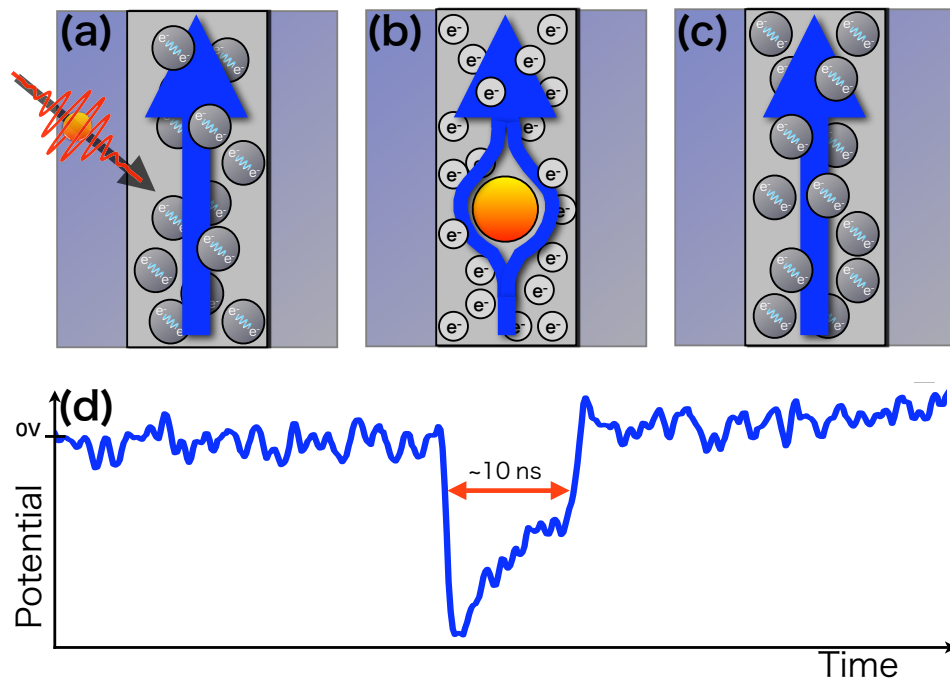


Figure E.1: *The operational principle of the SNSPD. (a) Photon is incident on a superconducting nanowire. (b) The absorbed photon creates a hotspot which the superconducting current must circumvent. Upon diversion the current density increases beyond J_c and the wire enters the normal mode and exhibits a potential drop. (c) The nanowire relaxes back to the superconducting state. (d) The potential vs. time plot shows the typical output of the detector during this process.*

E.4 Construction and Operation of the SNSPD System

The NbN nanowire must be cooled to lower than T_c such that it enters its superconducting phase. To achieve this, a commercial Sumitomo Heavy Industries RDK-101D 4K cold head is used to provide cooling. The head is a two-stage GM cycle cryo-refrigerator, delivering continuous, closed-cycle, refrigeration in the range of 40-60 K at the first stage and 3-4 K in the second phase, depending on the applied heat load. During pre-shipping inspection, the head was recorded at temperatures as low as 3.32 K with an applied heat load of 0.1 W. In order for the cold head to function it must be held in a vacuum chamber (to reduce the overall heat load). Such a chamber was constructed, from stainless steel, and tested to hold a vacuum down to 2×10^{-6} mbar. In order to further reduce the heat load on stage 2, a radiation shield consisting of a 3 mm thick aluminium cylinder closed at one end was attached to stage 1. Stage 2 was thus surrounded by the shield, sitting at ~ 40 K. Three silicon diode temperature sensors (*Lakeshore DT-670-CU*) were thermally contacted with Apiezon[®]-N grease to the 40K and 4K stages of the cold head, and the detector head assembly. These diodes were independently monitored using a Stanford Research Systems SIM922 diode temperature monitor such that the temperature of both stages and of the detector head could be checked during cool down. Upon switching on the Helium compressor, Helium is pumped to the cold head and the cooling process begins. A plot showing the temperature of the 2 stages during cool down can be found in figure E.2. It takes about 4 hours before stage 2 of the cold head reaches a steady ~ 3.5 K.

The detector heads were fibre coupled by C. M. Natarajan at Herriot Watt University. The process involves sending light down the fibre and then butt coupling the fibre to the detector whilst viewing the detector in transmission using a specialised jig. The fibre was then passed through a panel on the side of the vacuum can and glued in place using an epoxy resin to form a seal and ensure that the system was vacuum tight. The electrical contacts to the detectors were standard co-axial cables that were thermally coupled to both stage 2 and stage 1 of the cold head and connected internally to sma connectors on a separate panel on the vacuum can. The detectors could then be individually biased by sma connectors on the outside of the can,

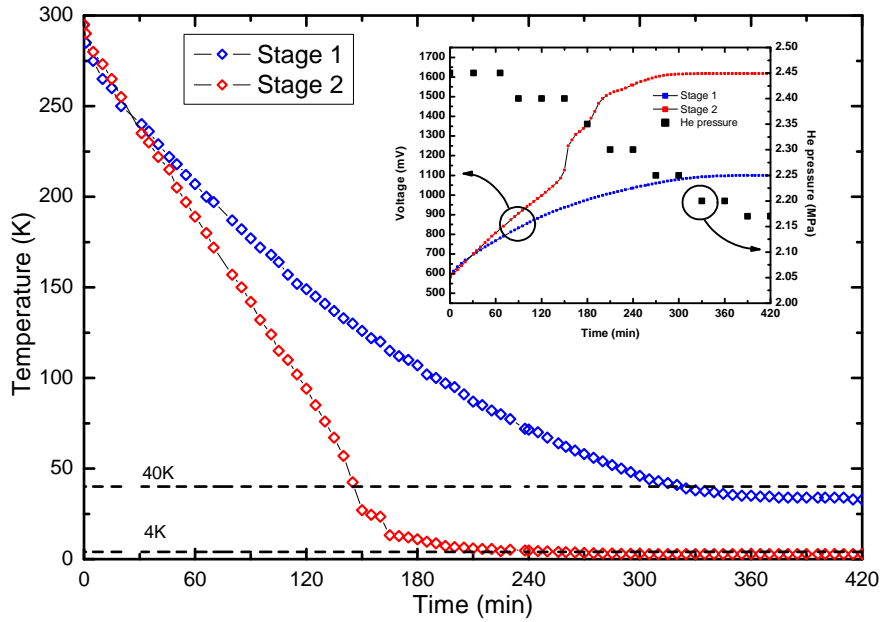


Figure E.2: *The temperature of the 2 cold head stages during the cool down process. The inset shows the raw response of the silicon diodes and also the helium pressure in the compressor unit.*

and optically addressed by coupling light into the fibre protruding from the input panel on the system.

Stanford Research Systems 928 rechargeable isolated voltage sources were used to provide the dc bias to the detectors enabling the bias to be set with mV accuracy. Both of the voltage sources and also the diode temperature monitor were housed in a Stanford Research Systems SIM900 mainframe rack system. A schematic of the detector is shown in figure E.3.

The circuit diagram for the bias and signal readout of the detector is presented in figure E.4. The dc bias voltage, V_{bias} , is passed through a 5575A bias tee consisting of an 8 mH inductor and a $0.22 \mu\text{F}$ capacitor. The signal from the detector after an event is detected (intrinsically ac) passes through the capacitor arm of the bias tee is then amplified by two amplifiers (LNA 580 and LNA 1000) before being measured. A 50Ω shunt resistor is placed in parallel with the detector to draw the current once the detector has gone normal, allowing it to recover it's superconducting status.

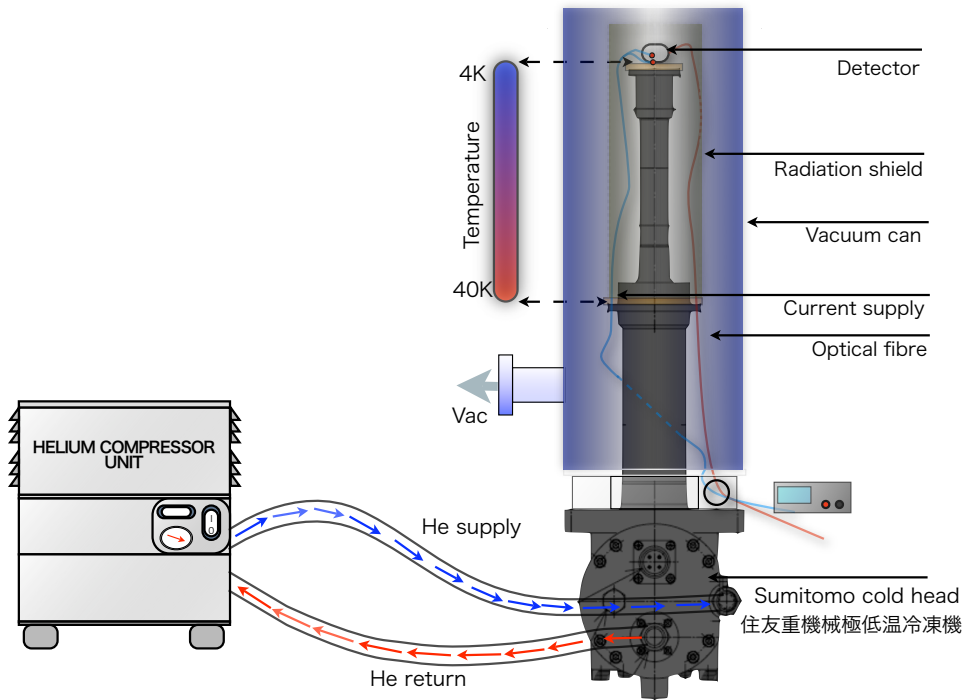


Figure E.3: A schematic of the SNSPD showing the critical components.

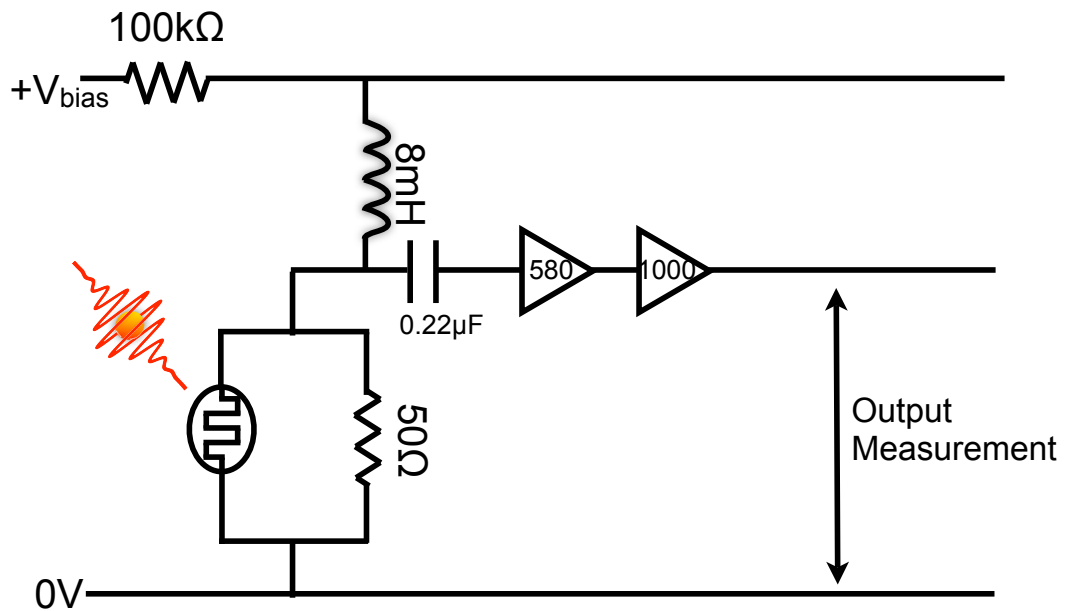


Figure E.4: The bias and signal read-out electronics for the superconducting nanowire single photon detector.

E.5 Characterisation

Initially the dead time of the detector was measured by feeding the amplified output into a 500 MHz oscilloscope [TEKTRONIX TDS 3052B]. A trace of the output signal during a dark count event is presented in figure E.5. The drop in potential is very clear, with the peak reaching -300 mV on a background of 0 mV. The superconducting nanowire turns normal on a very short time scale, seen as the sharp falling edge at the beginning of the pulse. This was measured with the oscilloscope to be ~ 200 ps. The detector takes comparatively much longer to recover its superconducting status, as can be seen by the ~ 15 ns relaxation time. It is this time which will ultimately limit the rep rate of the detector to ~ 66 MHz.

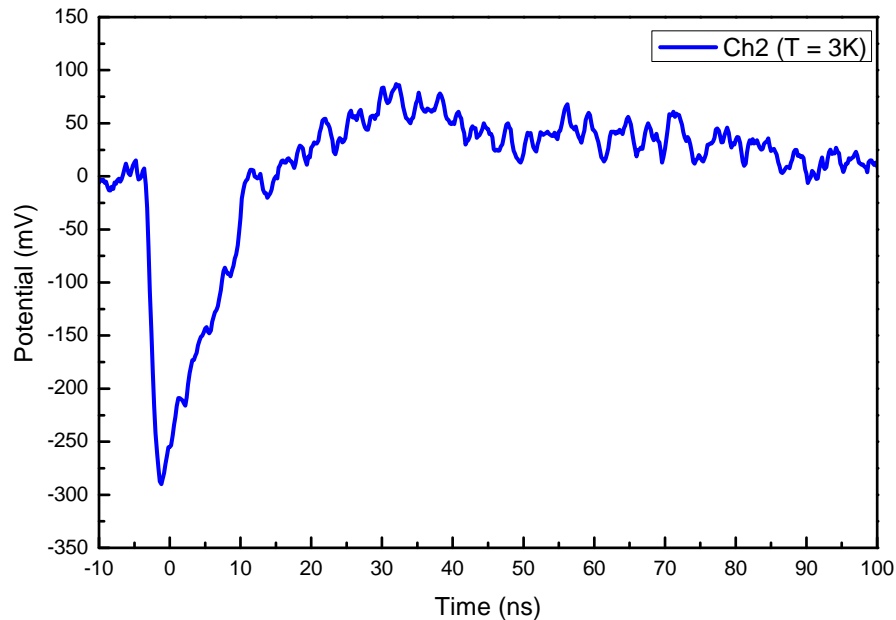


Figure E.5: *The trace of the channel 2 detector showing the sharp leading edge with which events will be measured. The decay time is ~ 15 ns, limiting the detector operation to 66 MHz.*

The Instrument response function (IRF) of the detector was characterised with an 800 nm pulsed Ti:Al₂O₃ laser operating with 150 fs pulses at 75.5 MHz. The laser pulse acts as a regular delta function so that the measured time distribution of pulses is exactly the IRF of the detector. The laser beam was split on a beam splitter such that the reflected beam was directed to a fast photo-diode [becker & Hickl PHD-400-N] and used as a measure of time. The unreflected beam

was coupled into a fibre which couples the light output directly to the nanowire detector. Each photon absorption event results in a spike in potential, like that that shown in figure E.5, which was sent to a commercial time correlated single photon counting module [Becker & Hickl SPC-134]. The time lapse between the count on the fast photodiode and the measurement of the output from the detector for each event is measured and entered into a histogram. After many events have been measured, the resulting histogram shows the IRF of the detector. It is limited by both jitter in the detector and the read out electronics. The IRF of channel 2, measured to have a full width at half maximum of 139.4 ps, is presented in figure E.6.

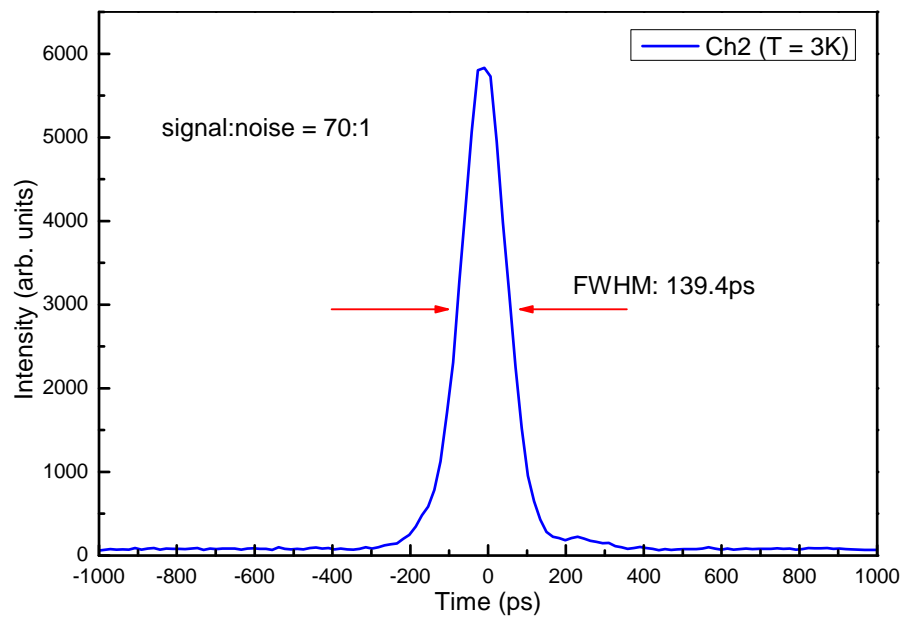


Figure E.6: *The Instrument response function of the channel 2 detector. The FWHM limited by jitter is 139.4 ps.*

It is immediately obvious that the IRF width, fitted with a Gaussian function, is very regular, and should prove fairly simple to de-convolve, if required, from any lifetime measurement that may be carried out using the detector. The signal to noise ratio is shown here to be 70:1 though this could in principle be made better with background subtraction (The dark counts, being random in time, create a steady background independent of time whereas the signal comes at regular intervals at the frequency of the excitation source).

The IRF was measured at a range of setup parameters. Both the bias of the nanowire

and the discrimination voltage were varied. Results, along with a plot of the dark count rate vs bias potential, are presented in figure E.7. As expected, the IRF increases in width when the nanowire is biased close to its critical current; increased dark counts and thermal noise conspire to broaden the detector response in time. The variation in width when the discrimination is varied is also easily understood by analysis of the detector trace. At low discrimination voltages the SPC detects background noise as real counts, and at high discriminations the sharp leading edge of the peak becomes more rounded, resulting in increased jitter.

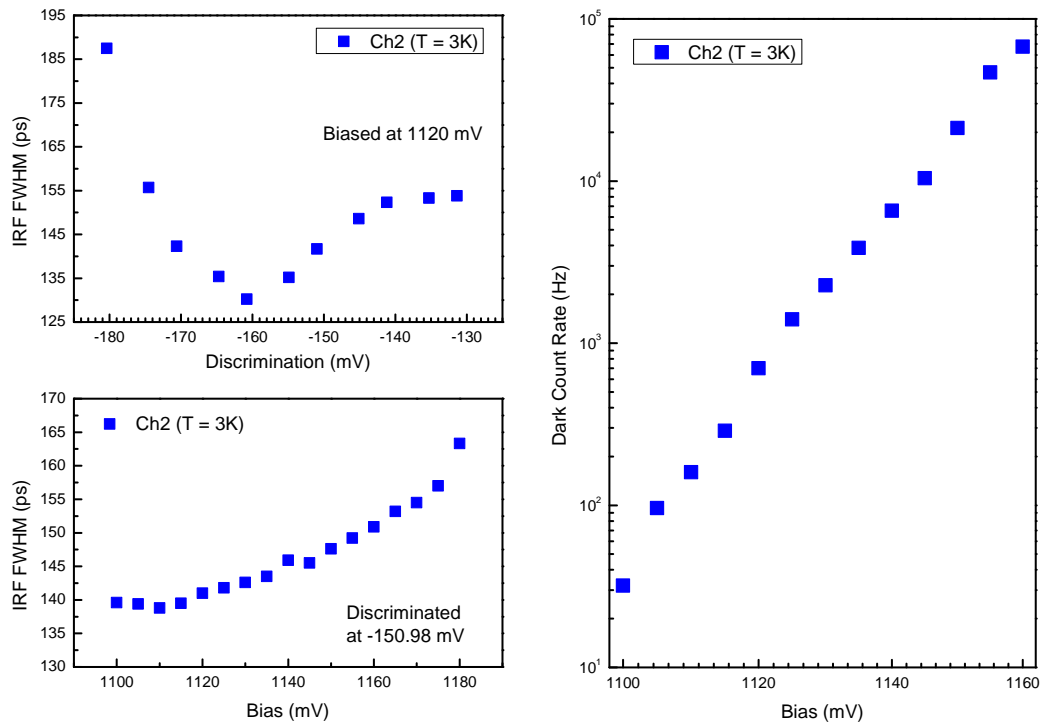


Figure E.7: *The effect of nanowire bias and discrimination setting on the IRF FWHM. The increase of dark count rate with nanowire bias is also presented.*

The result is that the IRF goes through a minimum at some intermediate discrimination potential, measured to be -161 mV in the case of a 1120 mV nanowire bias. The Dark count rate increases with bias due to random thermal events making the current in the nanowire exceed the critical current.

The quantum efficiency (QE), η , of the detector could also be measured by taking the ratio of detected events to the number of photons entering the detector within the same time

period. Due to the nature of the detector, a single photon pulse would be detected exactly the same (albeit with smaller probability) as a pulse with many photons: the detector has no photon number resolving capability. Therefore, to be absolutely sure that a fair measurement of the quantum efficiency is being made, it is imperative that the average number of photons per pulse be < 1 . This is achieved by attenuating the laser with ND filters. In the case of this experiment, the laser was attenuated to 3.699×10^{-12} W such that the mean number of photons per pulse, \bar{n} , was equal to 0.2, ensuring that each photon entering the detector had a fair chance of being detected. Data showing the dependence of η on the dark count rate, and hence on the detector bias, is presented in figure E.8. The dark count rate is kept below 10^6 Hz to make sure that the detector is far below its saturation frequency of 66 MHz. The quantum efficiency is measured to increase exponentially with increasing dark count rate. The detector can thus be biased according to the needs of the application. If a high QE is required but low signal to noise is acceptable (remember that the noise can be subtracted as its temporal properties are different from any signal) then the dark count rate can be set to $\sim 10^6$ Hz with appropriate bias and the detector will exhibit a QE of $\sim 2.5\%$.

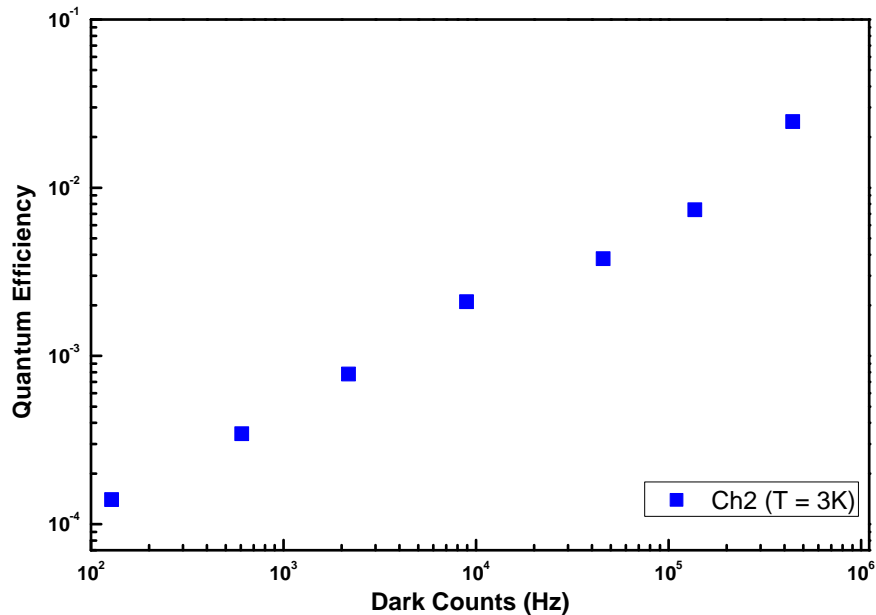


Figure E.8: The quantum efficiency ($N_{\text{detected events}}/N_{\text{photons in}}$) of the channel 2 detector when illuminated with 800 nm radiation from a Ti:Al₂O₃ laser.

E.6 Experimental use

The SNSPD was used to measure the lifetimes of an ensemble of InAs/GaAs quantum dots. The data can be found in figure E.9. A peak emission lifetime of 0.82 ns was observed under 1.5 mW excitation from a pulsed Ti:Al₂O₃ laser at 800 nm. This shows that the SNSPD can be used to detect emission in the near IR, and will be a useful tool for the measurement of lifetimes for QDs designed to emit at telecommunications wavelengths.

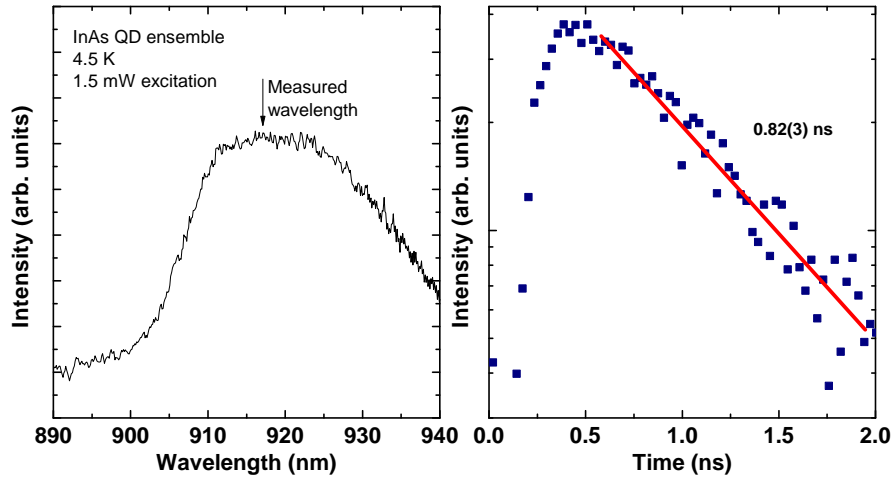


Figure E.9: *Emission spectrum and lifetime data of an ensemble of InGaAs quantum dots. The TRPL decay was acquired using the SNSPD described here.*

E.7 Summary and outlook

A SNSPD for use in the near IR has been successfully manufactured and employed in an experimental setting. The time resolution is acceptable, improving 3-fold on typical InGaAs APDs, but the efficiency is quite low, so the usefulness of this specific device will be limited. The measurement of single QD lifetimes may be possible, but will require minimal vibrations and long time accumulations. Novel designs for the detector heads can be found in the literature, some of which involve placing the nanowire at the mode maximum of a microcavity, maximising the probability of photon absorption [206].

- [1] M. E. Levinshtein, S. L. Rumyantsev, and M. S. Shur. *Properties of Advanced Semiconductor Materials*. Wiley-Interscience, 2001.
- [2] V. Tilak, A. Vertiatchikh, J. Jiang, N. Reeves, and S. Dasgupta. Piezoresistive and piezoelectric effects in GaN. *phys. stat. sol. (c)*, 3(6):2307, 2006.
- [3] U. K. Mishra, P. Parikh, and Y-F. Wu. AlGaIn/GaN HEMTs—an overview of device operation and applications. *proceedings of the IEEE*, 90(6):1022, 2002.
- [4] S. Rajan, H. Xing, S. DenBaars, U. K. Mishra, and D. Jena. AlGaIn/GaN polarization-doped field-effect transistor for microwave power applications. *Appl. Phys. Lett.*, 84(9):1591, 2004.
- [5] S. Nakamura, S. Pearton, and G. Fasol. *The Blue Laser Diode: The Complete Story*. Springer, Berlin, 2000.
- [6] Hiroshi Amano, Masahiro Kito, Kazumasa Hiramatsu, and Isamu Akasaki. P-type conduction in Mg-doped GaN treated with low-energy electron beam irradiation (LEEBI). *Jpn.J.Appl.Phys.*, 28(12):L2112, 1989.
- [7] S. Nakamura, T. Mukai, and M. Senoh. High-power gan p-n junction blue-light-emitting diodes. *Jpn.J.Appl.Phys.*, 30(L1998), 1991.
- [8] Isamu Akasaki and Hiroshi Amano. Breakthroughs in improving crystal quality of GaN and invention of the p-n junction blue-light-emitting diode. *Jpn.J.Appl.Phys.*, 45(12):9001–9010, 2006.
- [9] Anas F. Jarjour, Robert A. Taylor, Rachel A. Oliver, Menno J. Kappers, Colin J. Humphreys, and Abbes Tahraoui. Cavity-enhanced blue single-photon emission from a single InGaIn/GaN quantum dot. *Appl. Phys. Letts.*, 91:052101, 2007.

-
- [10] K. Bejtka, F. Reveret, R. W. Martin, P. R. Edwards, A. Vasson, J. Leymarie, I. R. Sellers, J. Y. Duboz, M. Leroux, and F. Semond. Strong light-matter coupling in ultrathin double dielectric mirror GaN microcavities. *Appl. Phys. Lett.*, 92:241105, 2008.
- [11] S. Christopoulos, G. Baldassarri H“oger von H”ogersthal, A. J. D. Grundy, P. G. Lagoudakis, A. V. Kavokin, J. J. Baumberg, G. Christmann, R. Butte and E. Feltin J.-F. Carlin, and N. Grandjean. Room-temperature polariton lasing in semiconductor microcavities. *Phys. Rev. Letts*, 98(126405), 2007.
- [12] J. J. Baumberg, A. V. Kavokin, S. Christopoulos, A. J. D. Grundy, R. Butte, G. Christmann, D. D. Solnyshkov, G. Malpuech, G. Baldassarri H“oger von H”ogersthal, E. Feltin, J.-F. Carlin, and N. Grandjean. Spontaneous polarization buildup in a room-temperature polariton laser. *Phys. Rev. Letts*, 101(136409), 2008.
- [13] A. Kikuchi, M. Kawai, M. Tada, and k. Kishino. InGaN/GaN multiple quantum disk nanocolumn light-emitting diodes grown on (111) Si substrate. *Jpn. J. Appl. Phys.*, 2(43):L1524, 2004.
- [14] A. Kikuchi, M. Tada, K. Miwa, and K. Kishino. Growth and characterization of InGaN/GaN nanocolumn LED. *Proc. of SPIE*, 6129:1, 2006.
- [15] T. Kouno, K. Kishino, K. Yamano, and A. Kikuchi. Two-dimensional light confinement in periodic InGaN/GaN nanocolumn arrays and optically pumped blue stimulated emission. *Op. Express*, 17(22):20440, 2009.
- [16] N. Sofikiti, N. Chaniotakis, J. Grandal, M. Utrera, M. A. Sanchez-Garcia, E. Calleja, E. Iliopoulos, and A. Georgakilas. Direct immobilization of enzymes in GaN and InN nanocolumns: The urease case study. *Appl. Phys. Lett.*, 95:113701, 2009.
- [17] J-W. Lee, K-J. Moon, M-H. Ham, and J-M. Myoung. Dielectrophoretic assembly of GaN nanowires for UV sensor applications. *Sol. Stat. Comm.*, 148:194, 2008.

-
- [18] H. Sekiguchi, K. Kishino, and A. Kikuchi. Formation of InGaN quantum dots in regularly arranged GaN nanocolumns grown by rf-plasma-assisted molecular-beam epitaxy. *phys. stat. sol. (c)*, 7(10):2374, 2010.
- [19] H. Sekiguchi, K. Kishino, and A. Kikuchi. Emission color control from blue to red with nanocolumn diameter of InGaN/GaN nanocolumn arrays grown on same substrate. *Appl. Phys. Lett.*, 96:231104, 2010.
- [20] K-Y. Lee, S. Shim, I-S. Kim, H. Oh, S. Kim, J-P. Ahn, S-H. Park, H. Rhim, and H-J. Choi. *Nanoscale. Res. Lett.*, 5:410–415, 2010.
- [21] C. Xie, L. Hanson, W. Xie, Z. Lin, B. Cui, and Y. Cui. Noninvasive neuron pinning with nanopillar arrays. *nanoletters*, 10(10):4020, 2010.
- [22] F. A. Ponce and D. P. Bour. Nitride-based semiconductors for blue and green light-emitting diodes. *Nature*, 386:351, 1997.
- [23] W. Shan, W. Walukiewicz, E. E. Haller, B. D. Little, J. J. Song, M. D. McCluskey, N. M. Johnson, Z. C. Feng, M. Schurman, and R. A. Stall. Optical properties of InGaN alloys grown by metalorganic chemical vapor deposition. *J. Appl. Phys.*, 84:4452, 1998.
- [24] M. Laugt, J. Massies, B. Gil, P. Lefebvre, M. Leroux, N. Grandjean, and P. Bigenwald. Quantum confined stark effect due to built-in internal polarization fields in AlGaIn/GaN quantum wells. *Phys. Rev. B*, 58(20):R13371, 1998.
- [25] J. Simon, R. Langer, A. Barski, and N. Pelekanos. *Phys. Rev. B*, 61(7211), 2000.
- [26] W.-H. Chang, K.-U. Tseng, C.M. Lee, C.-C. Chuo, C.Y. Lai, T.M. Hsu, and J.-I. Chyi. Direct measurement of piezoelectric field in InGaIn/GaN multiple quantum wells by electrotransmission spectroscopy. *J. Appl. Phys.*, 91(1):531, 2002.
- [27] B. Daudin, G. Feuillet, J.L. Rouviere, N.T. Pelekanos, F. Widmann, and J. Simon. Blue light emission from GaN self-assembled quantum dots due to giant piezoelectric effect. *Phys. Rev. B*, 58(4):989, 1998.

-
- [28] C. Y. Yeh, Z. W. Lu, S. Froyen, and A. Zunger. Zinc-blende-wurtzite polytypism in semiconductors. *Phys. Rev. B*, 46(16):10086, 1992.
- [29] T. C. Ozawa S. J. Kang. Balls and sticks: easy-to-use structure visualization and animation program. *J. Appl. Cryst.*, 37(4):679, Aug 2004.
- [30] J. A. Majewski, M. Stadele, and P. Vogel. *MRS Internet Journal of Nitride Semiconductor Research*, 1:1, 1996.
- [31] Bernard Gil, editor. *Low-Dimensional Nitride Semiconductors*. Oxford University Press, 2002.
- [32] J. F. Nye. *Physical Properties of Crystals (Their Properties by Tensors and Matrices)*. Oxford University Press, 1985.
- [33] S. J. Pearton, editor. *Optoelectronic properties of semiconductors and superlattices volume 2: GaN and related materials*. Gordon and Breach science publishers, 1997.
- [34] G. D. Chen, M. Smith, J. Y. Lin, H. X. Jiang, S-H. Wei, M. A. Khan, and C. J. Sun. Fundamental optical transitions in GaN. *Appl. Phys. Lett.*, 68(20):2784, 1996.
- [35] W. Y. Liang. Excitons. *Phys. Educ.*, 5:226, 1970.
- [36] B. Gil, editor. *Group III Nitride Semiconductor Compounds*. Oxford University Press, 1997.
- [37] B. Monemar. Fundamental energy gap of GaN from photoluminescence excitation spectra. *Phys. Rev. B*, 10(2):676, 1974.
- [38] M. Tchounkeu, O. Briot, B. Gil, J. P. Alexis, and R-L. Aulombard. Optical properties of GaN epilayers on sapphire. *J. Appl. Phys*, 80(9):5352, 1996.
- [39] D. Volm, K. Oettinger, T. Streibl, D. Kovalev, M. Ben-Chorin, J. Diener, B. K. Meyer, J. Majewski, L. Eckey, A. Hoffmann, H. Amano, I. Akasaki, K. Hiramatsu, and T. Detchprohm. Exciton fine structure in undoped GaN epitaxial films. *Phys. Rev. B*, 53(24):16543, 1996.

-
- [40] R. W. Martin, P. R. Edwards, R. Pecharroman-Gallego, C. Liu, C. J. Deatcher, I. M. Watson, and K. P. O'Donnel. Light emission ranging from blue to red from a series of InGaN/GaN single quantum wells. *J. Phys. D*, 35:604, 2002.
- [41] T. L. Tansley and C. P. Foley. Optical band gap of indium nitride. *J. Appl. Phys*, 59(9):3241, 1986.
- [42] V. Y. Davydov, A. A. Klochikhin, R. P. Seisyan, V. V. Emtsev, S. V. Ivanov, F. Bechstedt, J. Furthmuller, H. Harima, A. V. Mudryi, J. Aderhold, O. Semchinova, and J. Graul. Absorption and emission of hexagonal InN. evidence of narrow fundamental band gap. *phys. stat. sol. (b)*, 229(3):R1, 2002.
- [43] J. Wu, W. Walukiewicz, K. M. Yu, J. W. Ager III, E. E. Haller, H. Lu, and W. J. Schaff. Small band gap bowing in In_{1-x}Ga_xN alloys. *Appl. Phys. Lett.*, 80:4741, 2002.
- [44] J. Wu, W. Walukiewicz, K. M. Yu, J. W. Ager III, E. E. Haller, H. Lu, W. J. Schaff, Y. Saito, and Y. Nanishi. Unusual properties of the fundamental band gap of InN. *Appl. Phys. Lett.*, 80(21):3967, 2002.
- [45] T.V. Shubina, S.V. Ivanov, V. N. Jmerik, D. D. Solnyshkov, V. A. Vekshin, P. S. Kop'ev, A. Vasson, J. Leymarie, A. Kavokin, , K. Shimono, A. Kasic, and B. Monemar. Mie resonances, infrared emission, and the band gap of InN. *Phys. Rev. Lett.*, 92(11):117407, 2004.
- [46] B. R. Nag. Comment on band gap of InN and In-rich InGaN alloys. *phys. stat. sol. (b)*, 233(3):R8, 2002.
- [47] M. Moret, B. Gil, S. Ruffenach, O. Briot, Ch. Giesen, M. Heuken, S. Rushworth, T. Leese, and M. Succi. Optical, structural investigations and band gap bowing parameter of GaInN alloys. *J. Cryst. Growth*, 311:2795, 2009.

-
- [48] H. P. D. Schenk, M. Leroux, and P. de Mierry. Luminescence and absorption in InGaN epitaxial layers and the Van Roosbroeck-Schockley relation. *J. Appl. Phys.*, 88(3):1525, 2000.
- [49] C. A. Parker, J. C. Roberts, S. M. Bedair, M. J. Reed, S. X. Liu, N. A. El-Masry, and L. H. Robins. Optical band gap dependence on composition thickness of InGaN grown on GaN. *Appl. Phys. Lett.*, 75(17):2566, 1999.
- [50] Z. Dridi, B. Bouhafs, and P. Ruterana. First-principles investigation of lattice constants and bowing parameters in wurtzite AlGa_nIn_{1-n} alloys. *Semicond. Sci. Technol.*, 18:850, 2003.
- [51] M. Ferhat, J. Furthmuller, and F. Bechstedt. Gap bowing and Stokes shift in InGaN alloys: first principle studies. *Appl. Phys. Lett.*, 80(8):1394, 2002.
- [52] A. R. Denton and N. W. Ashcroft. Vegard's law. *Phys. Rev. A*, 43(6):3161, 1991.
- [53] I. Akasaki and H. Amano. *GaN*. Academic Press, 1998.
- [54] D. Gerthsen, B. Neubauer, A. Rosenauer, T. Stephan, H. Kalt, O. Schon, and M. Heuken. InGaN composition and growth rate during the early stages of metalorganic chemical vapor deposition. *Appl. Phys. Lett.*, 79(16):2552, 2001.
- [55] Y-H. Cho, G. H. Gainer, A. J. Fischer, J. J. Song, S. Keller, U. K. Mishra, and S. P. DenBaars. "s-shaped" temperature-dependent emission shift and carrier dynamics in InGa_nN/GaN multiple quantum wells. *Appl. Phys. Lett.*, 73(10):1370, 1998.
- [56] T. Kim, J. Kim, M-S. Yang, S. Lee, Y. Park, U-I. Chung, and Y. Cho. Highly efficient yellow photoluminescence from 11-22 InGa_nN multi-quantum-well grown on nanoscale pyramid structure. *Appl. Phys. Lett.*, 97:241111, 2010.
- [57] Y. P. Varshni. Temperature dependence of the energy gap in semiconductors. *Physica*, 34(1):149, 1967.

-
- [58] K. P. O'Donnell and X. Chen. Temperature dependence of semiconductor band gaps. *Appl. Phys. Lett.*, 58(25):2924, 1991.
- [59] R. Passler. Temperature dependence of exciton peak energies in multiple quantum wells. *J. Appl. Phys.*, 83(6):3356, 1998.
- [60] P. G. Middleton, K. P. O'Donnell, T. Breitkopf, H. Kalt, W. Van der Stricht, I. Moerman, and P. Demeester. The optical linewidth of InGaN light emitting diodes. *Mat. Sci. Eng.*, B50:285, 1997.
- [61] T. J. Badcock, R. Hao, M. A. Moram, P. Dawson, M. J. Kappers, and C. J. Humphreys. The effect of indium concentration on the optical properties of a-plane InGaN/GaN quantum wells grown on r-plane sapphire. *phys. stat. sol. (a)*, 208(7):1529, 2011.
- [62] F. Bernardini, V. Fiorentini, and D. Vanderbilt. Spontaneous polarization and piezoelectric constants of III-V nitrides. *Phys. Rev. B*, 56:R10024, 1997.
- [63] M. Posternak, A. Baldereschi, A. Catellani, and R. Resta. Ab initio study of the spontaneous polarization of pyroelectric BeO. *Phys. Rev. Lett.*, 64(15):1777, 1990.
- [64] V. Tilak, P. Batoni, J. Jang, and A. Knobloch. Measurement of piezoelectric coefficient of gallium nitride using metal-insulator-semiconductor capacitors. *Appl. Phys. Lett.*, 90:043508, 2007.
- [65] G. Bastard, E. E. Mendez, L. L. Chang, and L. Esaki. Variational calculations on a quantum well in an electric field. *Phys. Rev. B*, 28(6):3241, 1983.
- [66] D. A. B. Miller, D. S. Chemla, T. C. Damen, A. C. Gossard, W. Wiegmann, T. H. Wood, and C. A. Burrus. Electric field dependence of optical absorption near the band gap of quantum-well structures. *Phys. Rev. B*, 32(2):1043, 1985.
- [67] D. A. B. Miller, D. S. Chemla, T. C. Damen, A. C. Gossard, W. Wiegmann, T. H. Wood, and C. A. Burrus. Band-edge electroabsorption in quantum well structures: The quantum-confined stark effect. *Phys. Rev. Lett.*, 53(22):2173, 1984.

-
- [68] T. Wang, D. Nakagawa, J. Wang, T. Sugahara, and S. Sakai. Photoluminescence investigation of InGaN/GaN single quantum well and multiple quantum wells. *Appl. Phys. Lett.*, 73(24):3571, 1998.
- [69] Y-L. Lai, C-P. Liu, Y-H. Lin, T-H. Hsueh, R-M. Lin, D-Y. Lyu, Z-X. Peng, and T-Y. Lin. Origins of efficient green light emission in phase separated InGaN quantum wells. *Nanotechnology*, 17:3734, 2006.
- [70] Y. Shi, J. H. Zhao, G. Olsen, and H. Lee. Quantum confined stark effect in GaInAsSb/AlGaAsSb quantum wells grown by molecular beam epitaxy. *elec. Lett.*, 33(3):248, 1997.
- [71] I. Bar-Joseph, C. Klingshirn, D. A. B. Miller, D. S. Chemla, U. Koren, and B. I. Miller. Quantum-confined stark effect in InGaAs/InP quantum wells grown by organometallic vapour phase epitaxy. *Appl. Phys. Lett.*, 50(15):1010, 1987.
- [72] S. Hong and J. Singh. Study of the low-temperature line broadening mechanisms for excitonic transitions in GaAs/AlGaAs modular structures. *Appl. Phys. Lett.*, 49(6):331, 1986.
- [73] Z. C. Feng, editor. *III-Nitride: semiconductor materials*. Imperial College Press, 2006.
- [74] N. G. Weimann, L. F. Eastman, D. Doppalapudi, H. M. Ng, and T. D. Moustakas. Scattering of electrons at threading dislocations in GaN. *J. Appl. Phys.*, 83(7):3656, 1998.
- [75] D. Kalponek, X. H. Wu, B. Heying, S. Keller, B. P. Keller, U. K. Mishra, S. P. DenBaars, and J. S. Speck. structural evolution in epitaxial metalorganic chemical vapor deposition grown GaN films on sapphire. *Appl. Phys. Lett.*, 67(11):1541, 1995.
- [76] F. A. Ponce, B. S. Krusor, W. E. Piano, and D. F. Welch. Microstructure of GaN epitaxy on SiC using AlN buffer layers. *Appl. Phys. Lett.*, 67(3):410, 1995.
- [77] Z. Z. Bandic, T. C. McGill, and Z. Ikonc. Electronic structure of GaN stacking faults. *Phys. Rev. B*, 56(7):3564, 1997.

-
- [78] S. Nakamura, M. Senoh, S. Nagahama, N. Iwasa, T. Yamada, T. Matsushita, H. Kiyoku, Y. Sugimoto, T. Kozaki, H. Umemoto, M. Sano, and K. Chocho. InGaN/GaN/AlGaIn-based laser diodes with modulation-doped strained-layer superlattices grown on an epitaxially laterally overgrown GaN substrate. *Appl. Phys. Lett.*, 72(2):211, 1997.
- [79] J. E. Van Nostrand, K. L. Averett, R. Cortez, J. Boeckl, C. E. Stutz, N. A. Sanford, A. V. Davydov, and J. D. Albrecht. Molecular beam epitaxial growth of high-quality GaN nanocolumns. *J. Cryst. Growth*, 287:500, 2006.
- [80] L. Meshi, D. Cherns, I. Griffiths, S. Khongphetsak, A. Gott, C. Liu, S. Denchitcharoen, P. Shields, W. Wang, R. Campion, S. Novikov, and T. Foxon. The reduction of threading dislocations in gan using a GaN nanocolumn interlayer. *phys. stat. sol. (c)*, 5(6):1645, 2008.
- [81] H. Sekiguchi, K. Kato, J. Tanaka, A. Kikuchi, and K. Kishino. Ultraviolet GaN-based nanocolumn light-emitting diodes grown on n-(111) Si substrates by rf-plasma-assisted molecular beam epitaxy. *phys. stat. sol. (a)*, 205(5):1067, 2008.
- [82] H. J. Joyce, Q. Gao, H. H. Tan, C. Jagadish, Y. Kim, J. Zou, L. M. Smith, H. E. Jackson, J. M. Yarrison-Rice, P. Parkinson, and M. B. Johnston. III-V semiconductor nanowires for optoelectronic device applications. *Prog. Quant. Elect.*, 35:23, 2011.
- [83] Y. S. Park, C. M. Park, D. J. Fu, T. W. Kang, and J. E. Oh. Photoluminescence studies of GaN nanorods on Si(111) substrates grown by molecular beam epitaxy. *Appl. Phys. Letts.*, 85(5718), 2004.
- [84] Y. S. Park, S. H. Lee, J. E. Oh, C. M. Park, and T. W. Kang. Self-assembled GaN nanorods grown directly on (111) Si substrates: Dependence on growth conditions. *J. Cryst. Growth.*, 282:313, 2005.
- [85] C. M. Park, Y. S. Park, H. Im, and T. W. Kang. Optical properties of GaN nanorods grown by molecular-beam epitaxy; dependence on growth time. *nanotechnology*, 17:952, 2006.

-
- [86] R. M. Park. Low-resistivity p-type ZnSe:N grown by molecular beam epitaxy using a nitrogen free-radical source. *J. Vac. Sci. Technol. A*, 10:701, 1992.
- [87] T. Zywietz, J. Neugebauer, and M. Scheffler. Adatom diffusion at GaN (0001) and (0001) surfaces. *Appl. Phys. Lett.*, 73(4):487, 1998.
- [88] V. Consonni, M. Hanke, M. Knelangen, L. Geelhaar, A. Trampert, and H. Riechert. Nucleation mechanisms of self-induced gan nanowires grown on an amorphous interlayer. *Phys. Rev. B*, 83:035310, 2011.
- [89] V. Consonni, M. Knelangen, A. Trampert, L. Geelhaar, and H. Riechert. Nucleation and coalescence effects on the density of self-induced GaN nanowires grown by molecular beam epitaxy. *Appl. Phys. Lett.*, 98:071913, 2011.
- [90] V. Consonni, M. Knelangen, L. Geelhaar, A. Trampert, and H. Riechert. Nucleation mechanisms of epitaxial GaN nanowires: Origin of their self-induced formation and initial radius. *Phys. Rev. B*, 81:085310, 2010.
- [91] C.T. Foxon, S.V. Novikov, J.L. Hall, R.P. Campion, D. Cherns, I. Griffiths, and S. Khongphetsak. A complementary geometric model for the growth of GaN nanocolumns prepared by plasma-assisted molecular beam epitaxy. *J. Cryst. Growth*, 311:3423, 2009.
- [92] M. J. Holmes, Y. S. Park, X. Wang, C. C. S. Chan, A. F. Jarjour, R. A. Taylor, J. H. Warner, J. Luo, H. A. R. El-Ella, and R. A. Oliver. Carrier dynamics of InGaN quantum disks embedded in GaN nanocolumns. *J. Appl. Phys.*, 109:063515, 2011.
- [93] <http://www.nextnano.de/nextnano3/>.
- [94] C. Pryor, J. Kim, L W. Wang, and A. J. Williamson an A. Zunger. Comparison of two methods for describing the strain profiles in quantum dots. *J. Appl. Phys.*, 83(5):2548, 1998.
- [95] M. Grundmann, O. Stier, and D. Bimberg. InAs/GaAs pyramidal quantum dots: Strain distribution, optical phonons, and electronic structure. *Phys. Rev. B*, 52(16):11969, 1995.

-
- [96] Y. Kawakami, A. Kaneta, L. Su, K. Zhu, M. Funato, A. Kikuchi, and K. Kishino. *J. Appl. Phys.*, 107:023522, 2010.
- [97] Y-R. Wu, C. Chiu, C-Y. Chang, P. Yu, and H-C. Kuo. Size-dependent strain relaxation and optical characteristics of ingan/gan nanorod LEDs. *IEEE JOURNAL OF SELECTED TOPICS IN QUANTUM ELECTRONICS*, 15(4):1226, 2009.
- [98] J. Ristic, E. Calleja, A. Trampert, S. Fernandez-Garrido, C. Riviera, Y. Jahn, and K. H. Ploog. Columnar AlGa_N/Ga_N nanocavities with AlN/GaN Bragg reflectors grown by molecular beam epitaxy on Si(111). *Phys. Rev. Lett.*, 94:146102, 2005.
- [99] J. Ristic, C. Riviera, E. Calleja, S. Fernandez-Garrido, M. Povoloskyi, and A. Di Carlo. Carrier confinement effects in nanocolumnar Ga_N/AlGa_N quantum disks grown by molecular-beam epitaxy. *Phys. Rev. B*, 72:085330, 2005.
- [100] C. Riviera, U. Jahn, T. Flissikowski, J. L. Pau, E. Munoz, and H. T. Grahn. Strain-confinement mechanism in mesoscopic quantum disks based on piezoelectric materials. *Phys. Rev. B*, 75:045316, 2007.
- [101] P. Yu, C. H. Chiu, Y-R. Wu, H. H. Yen, J. R. Chen, C. C. Kao, H-W. Yang, H. C. Kuo, T. C. Lu, W. Y. Yeh, and S. C. Wang. Strain relaxation induced microphotoluminescence characteristics of a single InGa_N-based nanopillar fabricated by focused ion beam milling. *Appl. Phys. Lett.*, 93:081110, 2008.
- [102] F. Bernardini and V. Fiorentini. Polarization fields in nitride nanostructures: 10 points to think about. *appl. surf. sci.*, 166:23, 2000.
- [103] F. Bernardini, V Fiorentini, and D. Vanderbilt. Accurate calculation of polarization-related quantities in semiconductors. *Phys. Rev. B*, 63:193201, 2001.
- [104] D. C. Mojica and Y-M. Niquet. Stark effect in Ga_N/AlN nanowire heterostructures: Influence of strain relaxation and surface states. *Phys. Rev. B*, 81:195313, 2010.

-
- [105] S. L. Chuang and C. S. Chang. k.p method for strained wurtzite semiconductors. *Phys. Rev. B*, 54(4):2491, 1996.
- [106] S. L. Chuang and C. S. Chang. A band-structure model of strained quantum-well wurtzite semiconductors. *Semicond. Sci. Technol.*, 12:252, 1997.
- [107] I. Vurgaftman and J. R. Meyer. Band parameters for nitrogen-containing semiconductors. *J. Appl. Phys*, 94(6):3675, 2003.
- [108] Q. Yan, P. Rinke, M. Scheffler, and C. G. Van de Walle. Strain effects in group-III nitrides: Deformation potentials for AlN, GaN, and InN. *Appl. Phys. Lett.*, 95:121111, 2009.
- [109] R. Calarco, M. Marso, T. Richter, A. I. Aykanat, R. Meijers and A. V.D. Hart, T. Stoica, and H. Luth. Size-dependent photoconductivity in MBE-grown GaN-nanowires. *nanoletters*, 5(5):981, 2005.
- [110] P. D. C. King, T. D. Veal, H. Lu, P. H. Jefferson, S. A. Hatfield, W. J. Schaff, and C. F. McConville. Surface electronic properties of n- and p-type InGaN alloys. *phys. stat. sol. (b)*, 245(5):881, 2008.
- [111] T. D. Veal, P. H. Jefferson, L. F. J. Piper, C. F. McConville, T. B. Joyce, P. R. Chalker, L. Considine, H. Lu, and W. J. Schaff. *Appl. Phys. Lett.*, 89:202110, 2006.
- [112] I. Mahboob, T. D. Veal, L. F. J. Piper, C. F. McConville, H. Lu, and W. J. Schaff. Origin of electron accumulation at wurtzite InN surfaces. *Phys. Rev. B*, 69:201307(R), 2004.
- [113] R. Calarco and M. Marso. GaN and InN nanowires grown by MBE: A comparison. *Appl. Phys. A*, 87:499, 2007.
- [114] T. Stoica, R. J. Meijers, R. Calarco, T. Richter, E. Sutter, and H. Luth. Photoluminescence and intrinsic properties of MBE-grown InN nanowires. *nanoletters*, 6(7):1541, 2006.
- [115] L. Polenta, M. Rossi, A. Cavallini, R. Calarco, M. Marso, R. Meijers, T. Richter, T. Stoica, and H. Lüth. Investigation on localized states in GaN nanowires. *acs nano*, 2(287), 2.

-
- [116] C. Bocklin, R. G. Veprek, S. Steiger, and B. Witzigmann. *Phys. Rev. B*, 81:155306, 2010.
- [117] P. F. Moulton. Spectroscopic and laser characteristics of Ti:A1₂O₃. *J. Opt. Soc. Am. B*, 3(1):125, 1986.
- [118] Ealing. *Reflecting Microscope Objectives Catalogue*. available from <http://www.weyscientific.com>.
- [119] Andor Technology. *Shamrock 303i specifications*. available from <http://andor.com>.
- [120] Andor Technology. *Product Portfolio*. available from <http://www.andor.com>.
- [121] Becker and Hickl. *PMH-100 specifications sheet*.
- [122] Becker and Hickl. *PHD-400 specifications sheet*.
- [123] Becker and Hickl. *SPC-130 data sheet*.
- [124] <http://www.gatan.com>.
- [125] Mark J. Holmes, Young S. Park, Jamie H. Warner, and Robert A. Taylor. Quantum confined stark effect and corresponding lifetime reduction in a single In_xGa_{1-x}N quantum disk. *Appl. Phys. Lett.*, 95(18):18190, 2009.
- [126] Y. S. Park, M. J. Holmes, Y. Shon, I. T. Yoon, H. Im, and R. A. Taylor. GaN nanorods grown on Si (111) substrates and exciton localization. *Nanoscale. Res. Lett.*, 6:81, 2011.
- [127] J. Ristic, E. Calleja, M. A. Sanchez-Garcia, J. M. Ulloa, J. Sanchez-Paramo, J. M. Calleja, U. Jahn, A. Trampert, and K. H. Ploog. Characterization of GaN quantum discs embedded in Al_xGa_{1-x}N nanocolumns grown by molecular beam epitaxy. *Phys. Rev. B*, 68:125303, 2003.
- [128] E. Calleja, M. A. Sanchez-Garca, F. J. Sanchez, F. Calle, F. B. Naranjo, and E. Munoz. Luminescence properties and defects in GaN nanocolumns grown by molecular beam epitaxy. *Phys. Rev. B*, 62(24):16826, 2000.

-
- [129] A. Reale, G. Massari, A. Di Carlo, P. Lugli, A. Vinattieri, D. Alderighi, M. Colocci, F. Semond, N. Grandjean, and J. Massies. Comprehensive description of the dynamical screening of the internal electric fields of AlGaIn/GaN quantum wells in time-resolved photoluminescence experiments. *J. Appl. Phys*, 93:400, 2003.
- [130] D. M. Graham, A. Soltani-Vala, P. Dawson, M. J. Godfrey, T. M. Smeeton, J. S. Barnard, M. J. Kappers, C. J. Humphreys, and E. J. Thrush. *J. Appl. Phys*, 97:103508, 2005.
- [131] E. J. Thrush, M. J. Kappers, P. Dawson, D. Graham, J. S. Barnard, M. E. Vickers, L. Considine, J. T. Mullins, and C. J. Humphreys. *phys. stat. sol. (a)*, 192:354, 2002.
- [132] S. F. Chichibu, A. C. Abare, M. P. Mack, M. S. Minsky, T. Deguchi, D. Cohen, P. Kozodoy, S. B. Fleischer, S. Keller, J. S. Speck, J. E. Bowers, E. Hu, U. K. Mishra, L. A. Coldren, S. P. DenBaars, K. Wada, T. Sota, and S. Nakamura. *Mat. Sci. Eng*, B59:298, 1999.
- [133] M-Y. Ryu, G. G. Shim, P. W. Yu, E. Oh, Sone Chulsoo, O. Nam, and Y. Park. *Sol. Stat. Comm.*, 120:509, 2001.
- [134] X. H. Zhang, W. Liu, and S. J. Chua. *J. Cryst. Growth*, 268:521, 2004.
- [135] S. Kalliakos, X. B. Xhang, T. Talierco, P. Lefebvre, B. Gil, N. Grandjean, B. Damilano, and J. Massies. *Appl. Phys. Lett.*, 80:428, 2002.
- [136] R. A. Oliver, S. E. Bennet, T. Zhu, M. J. Kappers, D. W. Saxey, A. Cerezo, and C. J. Humphreys. *J. Phys. D*, 43:354003, 2010.
- [137] K. Domen, A. Kuramata, and T. Tanahashi. *Appl. Phys. Lett.*, 72:1359, 1998.
- [138] E. Kuokstis, J. W. Yang, G. Simin, M. Asif Khan, R. Gaska, and M. Shur. Two mechanisms of blueshift of edge emission in InGaIn-based epilayers and multiple quantum wells. *Appl. Phys. Lett.*, 80:977, 2002.
- [139] Y. Kawakami, S. Suzuki, A. Kaneta, M. Funato, A. Kikuchi, and k. Kishino. Origin of high oscillator strength in green-emitting InGaIn/GaN nanocolumns. *Appl. Phys. Lett.*, 89:163124, 2006.

-
- [140] R. Bardoux, A. Kaneta, M. Funato, Y. Kawakami, A. Kikuchi, and k. Kishino. Positive binding energy of a biexciton confined in a localization center formed in a single $\text{In}_x\text{Ga}_{1-x}\text{N}/\text{GaN}$ quantum disk. *Phys. Rev. B*, 79:155307, 2009.
- [141] Y. S. Park, M. J. Holmes, T. W. Kang, and R. A. Taylor. Quantum confined stark effect of InGaN/GaN multi-quantum disks grown on top of GaN nanorods. *Nanotechnology*, 21:115401, 2010.
- [142] T. Kuroda and A. Tackeuchi. *J. Appl. Phys.*, 92:3071, 2002.
- [143] H. Q. Hou and C. W. Tu. *J. Electron. Mater.*, 25:1019, 1996.
- [144] S. Fischer, G. Steude, D. M. Hofmann, F. Kurth, F. Anders, M. Topf, B. K. Meyer, F. Bertram, M. Schmidt, J. Christen, L. Eckey, J. Holst, A. Hoffman, B. Mensching, and B. Rauschenbach. *J. Cryst. Growth*, 189/190:556, 1998.
- [145] F. Calle, F. J. Sanchez, J. M. G. Tijero, M. A. Sanchez-Garcia, E. Calleja, and R. Beresford. *Semicond. Sci. Technol.*, 12:1396, 1997.
- [146] M. J. Holmes, Y. S. Park, X. Wang, C. C. S. Chan, B. P. L. Reid, H. Kim, R. A. Taylor, J. H. Warner, and J. Luo. Optical studies on a single GaN nanocolumn containing a single InGaN quantum disk. *Appl. Phys. Lett.*, 98:251908, 2011.
- [147] B. Yurdumakan, N. R. Raravikar, P. M. Ajayan, and A. Dhinojwala. Synthetic gecko foot-hairs from multiwalled carbon nanotubes. *Chem. Commun.*, page 3799, 2005.
- [148] Jr. A. S. Barker. Optical measurements of surface plasmons in gold. *Phys. Rev. B*, 8:5418, 1973.
- [149] K. Okamoto, A. Scherer, and Y. Kawakami. *Mater. Res. Soc. Symp. Proc.*, pages 1055–GG05–03, 1055.
- [150] K. Okamoto, I. Niki, A. Shvartser, G. Maltezos, Y. Narukawa, T. Mukai, Y. Kawakami, and A. Scherer. Surface plasmon enhanced bright light emission from InGaN/GaN . *phys. stat. sol. (a)*, 204:2103, 2007.

-
- [151] K. Okamoto and Y. Kawakami. High-efficiency InGaN/GaN light emitters based on nanophotonics and plasmonics. *IEEE JOURNAL OF SELECTED TOPICS IN QUANTUM ELECTRONICS*, 15(4):1199, 2009.
- [152] K. Okamoto, I. Niki, A. Scherer, Y. Nakamura, T. Mukai, and Y. Kawakami. *Appl. Phys. Lett.*, 87:071102, 2005.
- [153] S. Iijima. Helical microtubules of graphite carbon. *Nature*, 354:56, 1991.
- [154] J. Goldberger, R. He, Y. Zhang, S. Lee, H. Yan, H-J. Choi, and P. Yang. Single-crystal gallium nitride nanotubes. *Nature*, 422:599, 2003.
- [155] M. He, I. Minus, P. Zhou, S. N. Mohammed, J. B. Halpern, R. Jacobs, W. L. Sarney, L. Salamanca-Riba, and R. D. Vispute. Growth of large-scale GaN nanowires and tubes by direct reaction of Ga with NH_3 . *Appl. Phys. Lett.*, 77:3731, 2000.
- [156] P. M. Ajayan, O. Stephan, Ph. Redlich, and C. Colliex. Carbon nanotubes as removable templates for oxide nanocomposites and nanostructures. *Nature*, 375:564, 1995.
- [157] O. G. Schmidt and K. Eberl. Thin solid films roll up into nanotubes. *Nature*, 410:168, 2001.
- [158] Y. Wu and P. Yang. Melting and welding semiconductor nanowires in nanotubes. *Adv. Mater.*, 13:520, 2001.
- [159] E. Durgun, S. Tongay, and S. Ciraci. Silicon and III-V compound nanotubes: Structural and electronic properties. *Phys. Rev. B*, 72:075420, 2005.
- [160] S. Ismail-Beigi. Electronic excitations in single-walled GaN nanotubes from first principles: Dark excitons and unconventional diameter dependences. *Phys. Rev. B*, 77:035306, 2008.
- [161] N. Malkova and C. Z. Ning. Band structure and optical properties of wurtzite semiconductor nanotubes. *Phys. Rev. B*, 75:155407, 2007.
- [162] B. Xu and B. C. Pan. Size-dependent electronic and optical properties of GaN nanotubes studied using LDA calculations. *Phys. Rev. B*, 74:245402, 2006.

-
- [163] B. Liu, Y. Bando, M. Wang, C. Tang, M. Mitome, and D. Golberg. Crystallography and elasticity of individual GaN nanotubes. *Nanotechnology*, 20:185705, 2009.
- [164] S. C. Hung, Y. K. Su, S. J. Chang, S. C. Chen, L. W. Ji, T. H. Fang, L. W. Tu, and M. Chen. Self-formation of GaN hollow nanocolumns by inductively coupled plasma etching. *Appl. Phys. A*, 80:1607, 2005.
- [165] ID Quantique. *ID100 series specifications*. available from <http://www.idquantique.com>.
- [166] J. B. Schlager, K. A. Bertness, P. T. Blanchard, L. H. Robins, A. Roshko, and N. A. Sanford. Steady-state and time-resolved photoluminescence from relaxed and strained GaN nanowires grown by catalyst-free molecular-beam epitaxy. *J. Appl. Phys*, 103:124309, 2008.
- [167] L. Bergman, D. Alexon, P. L. Murphy, R. J. Nemanich, M. Dutta, M. A. Stroscio, C. Balkas, H. Shin, and R. F. Davis. Raman analysis of phonon lifetimes in AlN and GaN of wurtzite structure. *Phys. Rev. B*, 59:12977, 1999.
- [168] C. Kisielowski, J. Kruger, S. Ruvimov, T. Suski, J. W. Ager III, E. Jones, Z. Liliental-Weber, M. Rubin, E. R. Weber, M. D. Bremser, and R. F. Davis. Strain-related phenomena in GaN thin films. *Phys. Rev. B*, 54:17745, 1996.
- [169] L. Dong, S. K. Yadav, R. Ramprasad, and S. P. Alpay. Band gap tuning in GaN through equibiaxial in-plane strains. *Appl. Phys. Lett.*, 96:202106, 2010.
- [170] S. P. Lepkowskia, J. A. Majewskiband , and G. Jurczak. Nonlinear elasticity in wurtzite GaN/AlN planar superlattices and quantum dots. *acta physica polonica A*, 108(5):749, 2005.
- [171] T. S. Zheleva, O-H. Nam, M. D. Bremser, and R. F. Davis. Dislocation density reduction via lateral epitaxy in selectively grown GaN structures. *Appl. Phys. Lett.*, 71:2472, 1997.
- [172] B. L. Ward, O-H. Nam, J. D. Hartman, S. L. English, B. L. McCarson, R. Schlessler, Z. Sitar, R. F. Davis, and R. J. Nemanicha). Electron emission characteristics of GaN

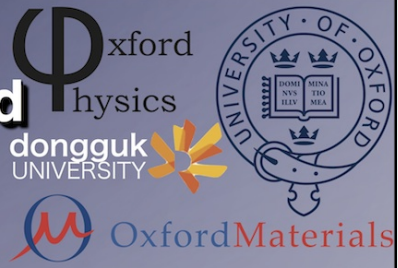
-
- pyramid arrays grown via organometallic vapor phase epitaxy. *J. Appl. Phys.*, 84(9):5238, 1998.
- [173] C. Liu, A. Satka, L. K. Jagadamma, P. R. Edwards, D. Allsopp, R. W. Martin, P. Shields, J. Kovac, F. Uherek, and W. Wang. Light emission from InGaN quantum wells grown on the facets of closely spaced GaN nano-pyramids formed by nano-imprinting. *Appl. Phys. Express*, 2:121002, 2009.
- [174] P. R. Edwards, R. W. Martin, I. M. Watson, C. Liu, R. A. Taylor, J. H. Rice, J. H. Na, J. W. Robinson, and J. D. Smith. Quantum dot emission from site-controlled InGaN/GaN micropyramid arrays. *Appl. Phys. Lett.*, 85(19):4281, 2004.
- [175] K. Tachibana, T. Someya, S. Ishida, and Y. Arakawa. Selective growth of InGaN quantum dot structures and their microphotoluminescence at room temperature. *Appl. Phys. Lett.*, 76(22):3212, 2000.
- [176] C. Liu, P. A. Shields, Q. Chen, D. W. E. Allsopp, W. N. Wang, C. R. Bowen, T.-L. Phan, and D. Cherns. Variations in mechanisms of selective area growth of GaN on nanopatterned substrates by MOVPE. *phys. stat. sol. (c)*, 7(1):32, 2010.
- [177] Q. K. K. Liu, A. Hoffmann, H. Siegle, A. Kaschner, C. Thomsen, . Christen, and F. Bertram. Stress analysis of selective epitaxial growth of GaN. *Appl. Phys. Lett.*, 74(21):3122, 1999.
- [178] Y-H. Cho, H. M. Kim, T. W. Kang, J. J. Song, and W. Yang. Spatially resolved cathodoluminescence of laterally overgrown GaN pyramids on 111 silicon substrate: Strong correlation between structural and optical properties. *Appl. Phys. Lett.*, 80(7):1141, 2002.
- [179] K. C. Zeng, J. Y. Lin, H. X. Jiang, and W. Yang. Optical properties of GaN pyramids. *Appl. Phys. Lett.*, 74(9):127, 1999.
- [180] S. Hess, F. Walraet, R. A. Taylor, J. F. Ryan, B. Beaumont, and P. Gilbert. Dynamics of resonantly excited excitons in GaN. *Phys. Rev. B*, 58:R15973, 1998.

-
- [181] Y. Takeda, D. Takagi, T. Sano, S. Tabata, N. Kobayashi, Q. Shen, T. Toyoda, J. Yamamoto, Y. Ban, and K. Matsumoto. Room temperature absorption edge of InGaN/GaN quantum wells characterized by photoacoustic measurement. *Jpn. J. Appl. Phys.*, 47:8805, 2008.
- [182] J. Wu, W. Walukiewicz, W. Shan, K. M. Yu, J. W. Ager III, S. X. Li, E. E. Haller, H. Lu, and W. J. Schaff. Temperature dependence of the fundamental band gap of InN. *J. Appl. Phys.*, 94:4457, 2003.
- [183] Hamamatsu photonics K.K. solid State deivison. *Characteristics and use of Si APD (Avalanche Photodiode)*, 2004.
- [184] Alfred Q. R. Baron, Shunji Kishimoto, John Morsec, and Jean-Marie Rigalc. Silicon avalanche photodiodes for direct detection of x-rays. *J. Synchrotron Rad.*, 13:131–142, 2006.
- [185] A. Lacaita, F. Zappa, S. Cova, and P. Lovati. Single-photon detection beyond 1 μm : performance of commercially available InGaAs/InP detectors. *Appl. Opt.*, 35(16):2986–2996, 1996.
- [186] F. Zappa, A. Lacaita, S. Cova, and P. Webb. Nanosecond single-photon timing with InGaAs/InP photodiodes. *Opt. Lett.*, 19(11):846–848, 1994.
- [187] Hamamatsu photonics K.K. solid State deivison. *InGaAs PIN photodiodes G8422/G8372/G8582 series*, 2008.
- [188] P. C. M. Owens, J. G. Rarity, P. R. Tapster, D. Knight, and P. D. Townsend. Photon counting with passively quenched germanium avalanche. *Appl. Opt.*, 33(30):6895–6901, 1994.
- [189] Robert H. Hadfield, Martin J. Stevens, Steven S. Gruber, and Aaron J. Miller. Single photon source characterization with a superconducting single photon detector. *Optics Express*, 13(26):10846, 2005.

-
- [190] A. Verevkin, A. Pearlman, W. slysz, J. Zhang, M. Currie, A. Korneev, G. Chulkova, O. Okunev, P. Kouminov, K. Smirnov, B. Voronov, G. N. Gol'tsman, and R. Sobolewski. Ultrafast superconducting single-photon detectors for near-infrared-wavelength quantum communications. *J. Mod. Opt.*, 51:1447–1458, 2004.
- [191] Kristine M. Rosfjord, Joel K. W. Yang, Eric A. Dauler, Andrew J. Kerman, Vikas Anant, Boris M. Voronov, Gregory N. Gol'tsman, and Karl K. Berggren. Nanowire single-photon detector with an integrated optical cavity and anti-reflection coating. *Optics Express*, 14(2):527, 2006.
- [192] Robert H. Hadfield, Martin J. Stevens, Richard P. Mirin, and Sae Woo Nam. Single-photon source characterization with twin infrared-sensitive superconducting single-photon detectors. *J. Appl. Phys*, 101:103104, 2007.
- [193] Martin J. Stevens, Robert H. Hadfield, Robert E. Schwall, Sae Woo Nam, Richard P. Mirin, and James A. Gupta. Fast lifetime measurements of infrared emitters using a low-jitter superconducting single-photon detector. *Appl. Phys. Letts.*, 89, 2006.
- [194] V. Anant, A. J. Kerman, E. A. Dauler, J. K. W. Yang, K. M. Rosfjord, and K. K. Berggren. Optical properties of superconducting nanowire single photon detectors. *optics express*, 16(14), 2008.
- [195] J. Bardeen, L. N. Cooper, and J. R. Schrieffer. Theory of superconductivity. *Phys. Rev.*, 108(5):1175–1204, Dec 1957.
- [196] J. Bardeen, L. N. Cooper, and J. R. Schrieffer. Microscopic theory of superconductivity. *Phys. Rev.*, 106(1):162–164, Apr 1957.
- [197] W. Meissner and R. Ochsenfeld. Ein neuer effekt bei eintritt der supraleitfähigkeit. *Naturwissenschaften*, 21(44):787–788, 1933.
- [198] Leon N. Cooper. Bound electron pairs in a degenerate Fermi gas. *Phys. Rev.*, 104(4):1189–1190, Nov 1956.

-
- [199] G. N. Gol'tsman, O. Okunev, G. Chulkova, A. Lipatov, A. Semenov, K. Smirnov, B. Voronov, A. Dzardanov, C. Williams, and R. Sobolewski. Picosecond superconducting single-photon optical detector. *Appl. Phys. Letts.*, 79(6):705–708, 2001.
- [200] Andrew J. Kerman, Eric A. Dauler, William E. Keicher, Joel K. W. Yang, Karl K. Berggren, G. Gol'tsman, and B. Voronov. Kinetic-inductance-limited reset time of superconducting nanowire photon counters. *Appl. Phys. Letts.*, 88:111116, 2006.
- [201] R. H. Hadfield, A. J. Miller, S. W. Nam, R. L. Kautz, and R. E. Schwall. Low-frequency phase locking in high-inductance superconducting nanowires. *Appl. Phys. Letts.*, 87:203505, 2005.
- [202] Shigehito Miki, Mikio Fujiwara, Masahide Sasaki, Burm Baek, Aaron J. Miller, Robert H. Hadfield, Sae Woo Nam, and Zhen Wang. Large sensitive-area NbN nanowire superconducting single-photon detectors fabricated on single-crystal MgO substrates. *Appl. Phys. Letts.*, 92:0611116, 2008.
- [203] A. Nigro, G. Nobile, V. Palmieri, G. Rubino, and R. Vaglio. Superconducting and normal state properties of niobium-nitride thin films. *Physica Scripta*, 38:483–485, 1988.
- [204] Shigehito Miki, Mikio Fujiwara, Masahide Sasaki, and Zhen Wang. NbN superconducting single-photon detectors prepared on single-crystal MgO substrates. *DE of the NbN nanowires seems much higher according to IEEE Trans. Appl. Supercond.*, 17(2):285, 2007.
- [205] F. Marsili, D. Bitauld, A. Fiore, A. Gaggero, F. Mattioli, R. Leoni, M. Benkahoul, and F. Levy. High efficiency NbN nanowire superconducting single photon detectors fabricated on MgO substrates from a low temperature process. *Optics Express*, 16(5):3191, 2008.
- [206] A. Gaggero, S. J. Nejed, F. Marsili, F. Mattioli, R. Leoni, D. Bitauld, D. Sahin, G. J. Hamhuis, R. Notzel, R. Sanjines, and A. Fiore. Nanowire superconducting single-photon detectors on GaAs for integrated quantum photonic applications. *Appl. Phys. Lett.*, 97:151108, 2010.

Internal field shielding and the quantum confined Stark effect in a single $\text{In}_x\text{Ga}_{1-x}\text{N}$ quantum disk



Mark J. Holmes,¹ Young S. Park,^{1,2} Jamie H. Warner,³ Jun Luo,³ Xu Wang,¹ Anas F. Jarjour,¹ and Robert A. Taylor¹

¹ Department of Physics, Clarendon Laboratory, University of Oxford, Parks Road, Oxford OX1 3PU, United Kingdom

² Department of Physics and Quantum Functional Semiconductor Research Center, Dongguk University, Seoul 100-715, Republic of Korea

³ Department of Materials, University of Oxford, Parks Road, Oxford OX1 3PH, United Kingdom

1. Introduction

Time-integrated and time-resolved microphotoluminescence studies were carried out on $\text{In}_x\text{Ga}_{1-x}\text{N}$ quantum disks embedded in GaN nanocolumns grown by molecular beam epitaxy. Emission at ~ 3.33 eV from confined states was detected and observed to blueshift with excitation power; a result of charge screening and the quantum confined Stark effect. Due to the reduced band bending and resulting increased overlap of the confined electron and hole wave functions, the lifetime of the emission was measured to decrease with increasing excitation power. The saturation of the blueshift and lifetime reduction follows that of the peak intensity, indicating a Stark screening process.

2. Sample growth and structure

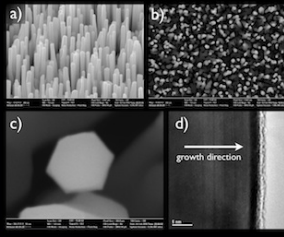
Samples grown by RF-MBE under nitrogen rich conditions on a Si(111) substrate, resulting in columnar growth.

$\text{In}_x\text{Ga}_{1-x}\text{N}$ quantum disk grown at the tip of each column, before being capped with GaN.

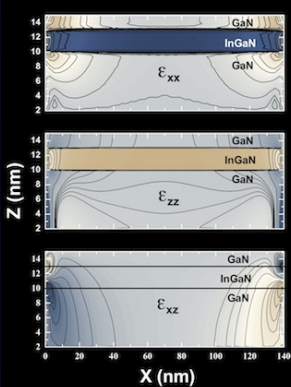
Columns are $\sim 3\mu\text{m}$ in length and $\sim 140\text{nm}$ in diameter.

Column density is $\sim 10^8\text{cm}^{-2}$.

QDisk is nominally 3nm in height. Indium mole fraction is estimated to be ~ 0.07 .

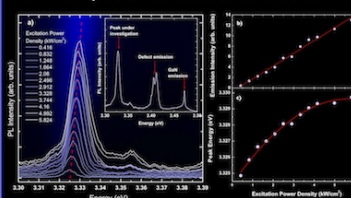


3 Strain distribution calculations



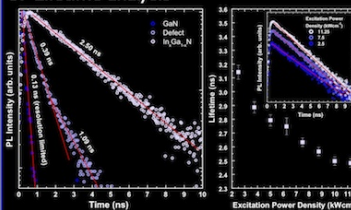
The strain distribution has been calculated for a 2.5nm QDisk of diameter 140nm using nextnano³ device simulator. An inhomogeneous distribution in strain may result in a lateral distribution in carriers as the effects of deformation and piezoelectric field play against each other.

4. Microphotoluminescence studies

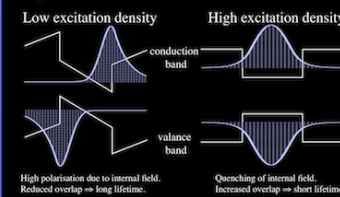


Time integrated $\mu\text{-PL}$ spectra at 4K reveal 3 main peak emissions. The I2 GaN bulk emission, the I1 emission from basal stacking faults, and a sharp narrow emission at ~ 3.325 eV from the $\text{In}_x\text{Ga}_{1-x}\text{N}$ QDisk. The emission from the QDisk shifts to the blue with increasing excitation power.

5. Lifetime analysis



Time resolved $\mu\text{-PL}$ spectra reveal that the emission attributed to the QDisk has a longer lifetime than the other emissions. Furthermore, the lifetime of the QDisk emission decreases as the excitation power is increased. This strongly indicates that carriers excited in the QDisk are compensating for the internal piezoelectric field in Wurtzite GaN and reducing the inherent band bending. The resulting increase in wavefunction overlap results in a reduced emission lifetime, as outlined in the diagram below.



It appears that there is a rise-time for the QDisk emission, possibly due to some charge transfer mechanism from the GaN nanocolumn. This hypothesis is further backed up by the maps in section 7.

It should also be noted that the lifetimes of the QDisk emission measured here ($\sim 3\text{ns}$) are not indicative of a lateral charge distribution brought about by an inhomogeneous distribution in strain. We conclude that both electrons and holes must be either confined at the center of the disk, or at the edges.

6. Many column analysis

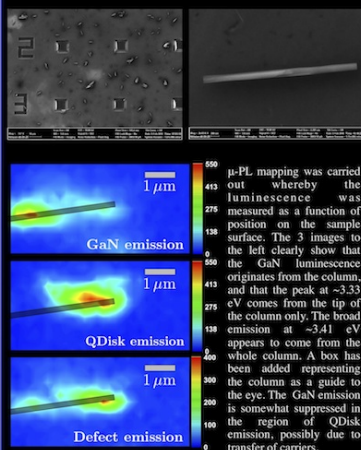
Under an electric field (F), the energy shift due to the Stark effect can be written as

$$\Delta E(F) = \mu F + \alpha F^2$$

where μ is the exciton dipole moment. The linear gradient of the shift has been measured for several columns and plotted against the emission lifetime. A trend of increasing lifetime with increasing dipole moment is consistent with the explanation that the effects measured here are due field screening and to the QCSE. It is also found that the long lifetime QDisks are those that emit at low energies, and thus have a larger indium mole fraction.

7. Single column and future work...

A grid was patterned in gold on quartz using e-beam lithography. Single columns were dispersed in a solvent over the surface such that they could be located and investigated with $\mu\text{-PL}$.



future experiments will involve trying to electrically contact the nanocolumns, and the application of a lateral electric field.

References

M. J. Holmes, Y. S. Park, J. H. Warner and R. A. Taylor Appl. Phys. Lett. 95, 181904 (2009)
Y. S. Park, M. J. Holmes, T. W. Kang and R. A. Taylor Nanotechnology 21, 115401 (2010)

Acknowledgements

Engineering and Physical Sciences Research Council (EP/S01116/1, EP/S01116/2)
Basic Science Research Program: National Research Foundation of Korea (2009-0079007)

Figure E.10: The poster presentation from ICPS 2010 in Seoul, Korea.

Optical Studies of GaN Nanocolumns Containing InGaN Quantum Disks and the Effect of Strain Relaxation on the Carrier Distribution



Mark J. Holmes,¹ Young S. Park,¹ Xu Wang,¹ Christopher C. S. Chan,¹ Benjamin P. L. Reid,¹ HeeDae Kim,¹ H. A. R. El-Ella,² Jun Luo,³ Jamie H. Warner,³ R. A. Oliver,² and Robert A. Taylor¹

¹ Department of Physics, Clarendon Laboratory, University of Oxford, Parks Road, Oxford OX1 3PU, United Kingdom
² Department of Materials Science and Metallurgy, University of Cambridge, Pembroke Street, Cambridge CB2 3QZ, United Kingdom
³ Department of Materials, University of Oxford, Parks Road, Oxford OX1 3PH, United Kingdom

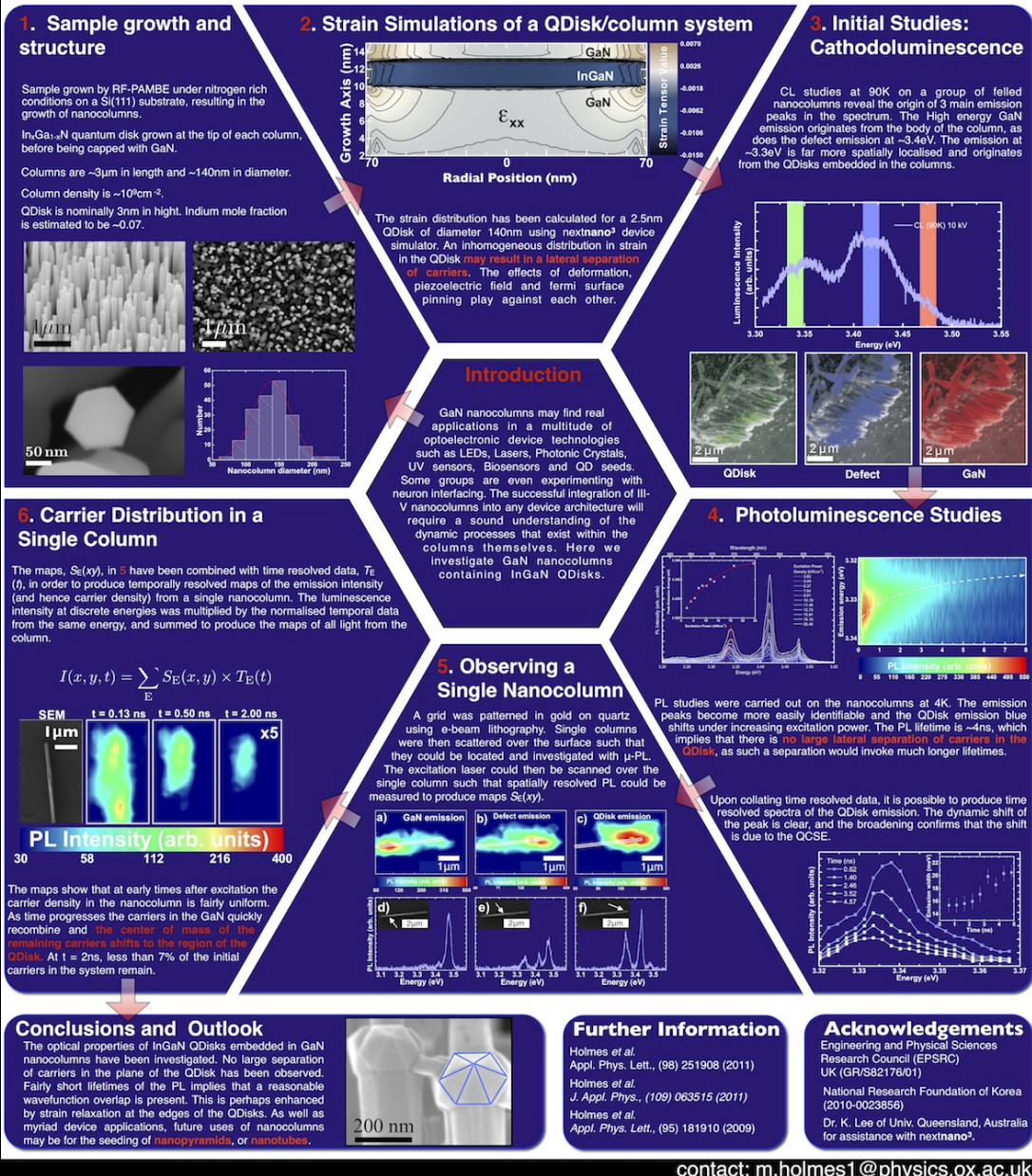


Figure E.11: The poster presentation from ICNS 2011 in Glasgow, Scotland. [This poster was selected for the Young Researcher Award at the conference].